Two New Methods to Improve Adaptive Time-Frequency Localization

by

Ziyu Chen

Department of Mathematics
Duke University

Date: _____

Approved:

_____
Ingrid Daubechies, Advisor

_____
Hau-Tieng Wu

_____
Jianfeng Lu

_____
Shahar Kovalsky

Dissertation submitted in partial fulfillment of the
requirements for the degree of Doctor of Philosophy
in the Department of Mathematics
in the Graduate School of
Duke University

2021

ABSTRACT

Two New Methods to Improve Adaptive Time-Frequency Localization

by

Ziyu Chen

Department of Mathematics
Duke University

Date: _____

Approved:

_____
Ingrid Daubechies, Advisor

_____
Hau-Tieng Wu

_____
Jianfeng Lu

_____
Shahar Kovalsky

An abstract of a dissertation submitted in partial fulfillment of the requirements for the degree of Doctor of Philosophy in the Department of Mathematics in the Graduate School of Duke University

2021

Abstract

This dissertation introduces algorithms that analyze oscillatory signals adaptively. It consists of three chapters.

The first chapter reviews the adaptive time-frequency analysis of 1-dimensional signals. It introduces models that capture the time-varying behavior of oscillatory signals. Then it explains two state-of-the-art algorithms, named the SynchroSqueezed Transform (SST) and the Concentration of Frequency and Time (ConceFT), that extract the instantaneous information of signals; this chapter ends with a discussion of some of the shortcomings of SST and ConceFT, which will be remedied by the new methods introduced in the remainder of this thesis.

The second chapter introduces the Ramanujan DeShape Algorithm (RDS); it incorporates the periodicity transform to extract adaptively the fundamental frequency of a non-harmonic signal.

The third part proposes an algorithm that rotates the time-frequency content of an oscillatory signal to obtain a time-frequency representation that has fewer artifacts.

Numerical results illustrate the theoretical analysis.

Acknowledgements

First and foremost, I would like to thank my advisor Prof. Ingrid Daubechies, for her constant support and advice in the past five years, and allowing me to explore other research directions freely. I sincerely appreciate her patience and detailed explanations whenever I brought a question to her. I would also like to thank my co-advisor Prof. Hau-Tieng Wu for building up my insights in time-frequency analysis and data analysis. I gratefully thank them for the many efforts they made, financially and academically, that helped develop my path. I also want to thank Prof. Jianfeng Lu and Prof. Shahar Kovalsky for agreeing to sit on the defense committee.

I would also like to thank Prof. Xiuyuan Cheng for the opportunity to fuse neural networks with spectral embedding, as well as for the organization of a reading group in spectral graph theory; Dr. Yingzhou Li for many informative discussions in neural networks and numerical linear algebra.

Last but not least, I want to thank my parents for their continued support.

Contents

List of Figures

Chapter 1

Introduction[1]

Oscillatory signals are ubiquitous in our life. For example, signals in seismology, finance and medicine are usually oscillatory. They are often "non-stationary", composed of multiple oscillatory components, each characterized by its own pattern, frequency and amplitude. In many cases, these characteristics may change as time progresses, meaning the components can have time-varying frequency, time-varying amplitude, or even time-varying oscillatory pattern. In practice, these time-varying quantities encode precise and useful information about the underlying system, which is why it is of paramount interest in signal processing to extract those time-varying quantities from the given signal. From these quantities, researchers hope to infer the underlying system behavior, or forecast the upcoming events. In this thesis, we are concerned mostly with developing precise and reliable methods to extract the time-varying information itself.

If the observed signal f can be written as a finite sum of so-called harmonic components, i.e. $f(t) = \sum_l a_l \cos(2\pi\xi_l t + \alpha_l)$, where $a_l > 0$ and $\xi_l > 0$ represent the amplitude and frequency of the l-th component respectively, then one can recover the a_l and ξ_l from $f(t)$ via the Fourier transform $\hat{f}$ of f, defined by $\hat{f}(\xi) := \int f(t)e^{-2\pi i\xi t}\,\mathrm{d}t$. However, many signals of interest in practice often exhibit time-varying behavior, meaning that a_l and ξ_l themselves may vary with time. We shall be interested in signals that are such combinations of oscillatory components whose amplitude and frequency are not longer constant. In [15], motivated by capturing time-varying amplitude and frequency of a given time series, Daubechies et al. consider *intrinsic mode type* (IMT) functions, i.e. functions f of the type

$$f(t) = A(t)\cos(2\pi\varphi(t)), \tag{1.1}$$

where $A(t) > 0$ is a smooth function that represents the time-varying amplitude of the signal, and $\varphi(t)$ is a smooth monotonically increasing function that describes the phase

[1]Some of the content of this chapter overlaps with introductory material from the paper [9], of which the author of this thesis is a co-author.

of the signal. We call $A(t)$ the *amplitude modulation* (AM) and $\varphi'(t)$ the *instantaneous frequency* (IF). In practice, $\frac{1}{\varphi'(t)}$ can be understood as the *instantaneous period* (IP) of the oscillation at time t. Some conditions are typically imposed on the time-dependence of A and φ; otherwise we cannot identify A and φ in general. A common condition is that A and φ' change *slowly* when compared to the oscillation frequency; more precisely, for some small $\epsilon > 0$, we assume $|A'(t)| \leq \epsilon\varphi'(t)$ and $|\varphi''(t)| \leq \epsilon\varphi'(t)$ for all $t \in \mathbb{R}$. Under this condition, the identifiability of A, φ and φ' of the IMT function has been proved in [8]. A signal satisfies the *adaptive harmonic model (AHM)* if it is a linear combination of a fairly small number of IMT functions,

$$f(t) = \sum_{l=1}^{L} f_l(t) + \Phi(t), \tag{1.2}$$

where $L \in \mathbb{N}^+$ (with even $L = 1$ a case of interest) and each $f_l = A_l(t)\cos(2\pi\varphi_l(t))$ is an IMT function, with the additional assumption that $\varphi_l'(t) > \varphi_{l-1}'(t)$ and the separation of $\varphi_l'(t)$ and $\varphi_{l-1}'(t)$ is uniformly bounded from below; finally $\Phi(t)$ is a mean zero random process that models noise or other stochastic quantity of interest. Note that Φ does not need to be stationary; for instance, we may consider the piecewise locally stationary random process [77] (which is not, itself, stationary) as the noise model. (See [8] for more discussion when the noise is nonstationary.) For readers interested in the identifiability issue of the AHM, we refer to [8] for details and proof. The AHM has been proved useful to model various types of time series from different fields, including instantaneous heart rate [30], vibration signal [24], and seismic signal [71].

The last few decades have seen many approaches, in signal processing and applied harmonic analysis, to develop analysis tools for signals of this type; this is the field of *time-frequency (TF) analysis*. TF analysis extracts the temporal and spectral information from the signal simultaneously. The short-time Fourier transform (STFT) and continuous wavelet transform (CWT) are probably the most well known TF analysis tools. Usually, a TF analysis tool converts the given signal, a function defined on $\mathbb{R}$, which parametrizes time, into a TF representation (TFR), a function defined on $\mathbb{R}^2$, which parametrizes time and frequency. The user can then read the oscillatory information from the TFR; for example,

how fast and strong the signal oscillates at a given time, or if there is a singularity. Usually, the modulation of the TFR is represented as an image for users' visual inspection; for example, the squared modulation of STFT is the widely applied spectrogram, and the squared modulation of CWT is the scalogram. For example, in the STFT of a function $f \in L^2$, the (modified) *windowed* or *short-time Fourier transform* (STFT) associated with a window function $g(t)$ is defined as:

$$V_f^{(g)}(t,\xi) := \int f(x)g(x-t)e^{-2\pi i\xi(x-t)}\,\mathrm{d}x,$$

where $t \in \mathbb{R}$ is the time, $\xi \in \mathbb{R}^+$ is the frequency, and g is the window function chosen by the user such as the commonly used Gaussian functions centered at the origin.

However, both the STFT and the CWT are subject to the Heisenberg uncertainty principle, limiting how accurately oscillatory information can be captured over short time intervals, and this typically expresses itself by a "blurring" or "smearing out" of their TFR, see Figure 1.1. One recently developed approach to obtain a sharpened or more concentrated TFR for a special class of functions is the synchrosqueezed transform (SST) [15, 62]. The STFT-based SST of a signal f is defined as:

$$S_f^{(g)}(t,\xi) := \lim_{\alpha\to 0}\int V_f^{(g)}(t,\eta)h_\alpha(\xi-\omega_f^{(g)}(t,\eta))\,\mathrm{d}\eta,$$

where h_α is an "approximate δ-function" (i.e. h is smooth and has fast decay, with $\int h(x)\,\mathrm{d}x = 1$, so that $h_\alpha(t) := \frac{1}{\alpha}h(\frac{t}{\alpha})$ tends weakly to the delta measure δ as $\alpha \to \infty$), and with the reassignment rule $\omega_f^{(g)}(t,\eta)$ defined by

$$\omega_f^{(g)}(t,\eta) := \Re\frac{\partial_t V_f^{(g)}(t,\xi)}{2\pi i V_f^{(g)}(t,\xi)} \text{ if } V_f^{(g)}(t,\xi) \neq 0, \text{ and } \omega_f^{(g)}(t,\eta) := -\infty \text{ otherwise,}$$

where $\Re$ indicates the real part of a complex number. An example of the SST is shown in Figure 1.1, which illustrates that the SST of the signal provides indeed a "sharper" TFR compared to its STFT. This approach is designed for and gives good results for functions that satisfy AHM, when the noise is weak.

More recently, Daubechies et al. proposed the Concentration of Frequency and Time (ConceFT) algorithm [16], which combines multi-taper estimation ideas and averaging over

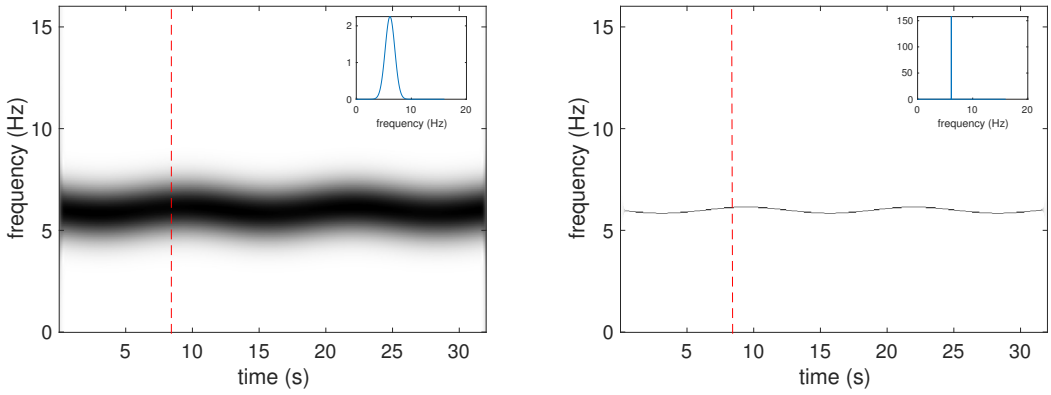

Figure 1.1: Left: $\left|V_f^{(g)}(t,\xi)\right|$ of f; right: $\left|S_f^{(g)}(t,\xi)\right|$ of f. In both cases, the inset window graphs the vertical section of the gray-scale figure at $t_0 = 8$s.

random projections with synchrosqueezing, to determine the TFR of signals even when they are corrupted by significant and challenging noise. The STFT-based ConceFT can be described as follows:

- Take J orthonormal window functions, $g_1, \ldots, g_J$, with good concentration in the TF-plane a common choice is a gaussian function and higher-order Hermite functions.[2]
- Uniformly sample N random vectors $\boldsymbol{r}_n$, $n = 1, \ldots, N$ in the unit sphere S^{J-1}.
- For each n between 1 and N, define $g_{[n]} := \sum_{j=1}^{J} (\boldsymbol{r}_n)_j \psi_j$, and $V_f^{(g_{[n]})} = \sum_{j=1}^{J} (\boldsymbol{r}_n)_j V_f^{(g_j)}$.
- For each n between 1 and N, evaluate the reassignment rule $\omega_f^{(g_{[n]})}(t,\eta)$, and hence $S_f^{(g_{[n]})}(t,\xi)$, the final ConceFT representation of f is the average

$$C_f(t,\xi) := \frac{1}{N} \sum_{n=1}^{N} S_f^{(g_{[n]})}(t,\xi).$$

[2]There also exists an SST approach based on continuous wavelet transforms, which we shall not discuss in this thesis, that can be likewise enhanced by the ConceFT approach; in that case the Hermite window functions are typically replaced by reference wavelets that are the Laguerre functions [16].

Figure 1.2 gives an example of the ConceFT of a signal compared with its SST when the signal is corrupted with significant noise.

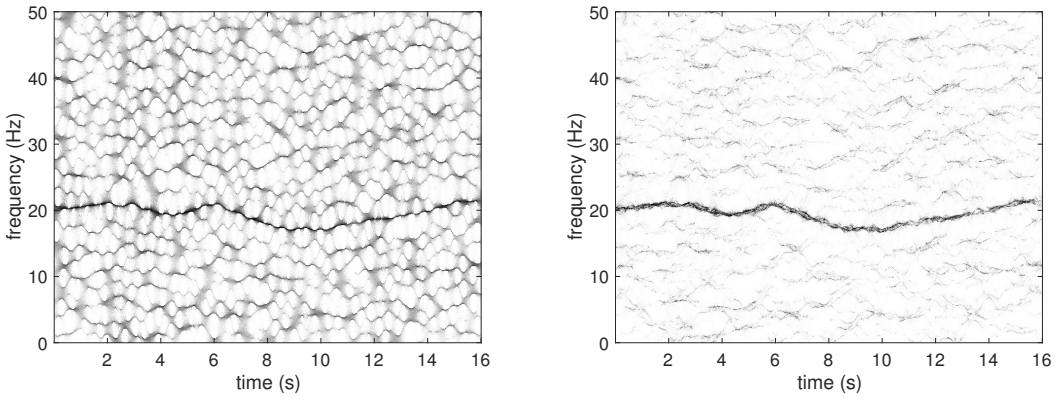

Figure 1.2: Left: The SST of a signal; right: the ConceFT of the signal. SNR = -2.5098 dB.

The AHM has been considered in various applied problems. However, there are many oscillatory signals that cannot be *satisfactorily* modeled by the AHM, since their oscillatory pattern is non-sinusoidal. The main observation that the oscillatory pattern is non-sinusoidal motivates us to replace the cosine function in the IMT function by a 1-periodic function to capture this non-sinusoidal oscillatory pattern [73]:

$$f(t) = A(t)s(\varphi(t)), \tag{1.3}$$

where $\left|A'(t)\right| \leq \epsilon\varphi'(t)$ and $\left|\varphi''(t)\right| \leq \epsilon\varphi'(t)$ for some small $\epsilon > 0$ and for all $t \in \mathbb{R}$, and $s(x)$ is a real 1-periodic function, but not simply of the form $\cos(2\pi\xi x + \beta)$. Here, $s(t)$ is called the *wave-shape function*. Figure 1.3 gives an example of a signal with non-sinusoidal oscillation pattern. Usually we assume that the wave-shape function has zero mean; asking that it has unit L^2 norm defines $A(t)$ uniquely. In [73], the first Fourier coefficient of s is assumed to be $\hat{s}(1) \neq 0$, and this condition is later relaxed in [74]. When the real function s is reasonable, f could be expanded in its Fourier series, leading to

$$f(t) = \sum_{n=0}^{\infty} A(t)a_n \cos(2\pi n\varphi(t) + \alpha_n), \tag{1.4}$$

where $a_n \geq 0$ and $\alpha_n \in [0, 2\pi)$ are associated with the Fourier coefficients of s. More precisely, $\hat{s}(n) = \int_0^1 s(x)e^{-2\pi inx}\,\mathrm{d}x$ for $n \in \mathbb{Z}$, and $\hat{s}(n) = \frac{1}{2}a_n e^{i\cdot\mathrm{sign}(\alpha_n)\alpha_n}$, with $\hat{s}(-n) = \overline{\hat{s}(n)}$ because s is real. (Note that the zero-mean assumption for s translates to $\hat{s}(0) = 0$.) (Note that the equality in (1.4) in general has to be understood in the distribution sense; it holds in the pointwise sense if s is smooth enough.) Therefore, instead of viewing f in (1.3) as an oscillatory signal with single oscillatory component with non-sinusoidal oscillation, we could also view f as an oscillatory signal with multiple components with sinusoidal oscillation pattern as in (1.1). Under this interpretation, we call the first oscillatory component $A(t)a_1\cos(2\pi\varphi(t) + \alpha_1)$ the *fundamental component* and $A(t)a_n\cos(2\pi n\varphi(t) + \alpha_n)$, $n \geq 2$ the *n-th multiple* (or harmonic) of the fundamental component. We call the IF $\varphi'(t)$ of the fundamental component the *fundamental IF* of f, and clearly, the IF of the nth multiple is n-times the fundamental frequency.

Analysis of such signals is more complex if there is a mixture of several oscillations with different shapes. We shall say that signal satisfies the *adaptive non-harmonic model (ANHM)* if it can be written as

$$f(t) = \sum_{l=1}^{L} f_l(t) + \Phi, \tag{1.5}$$

where $L \in \mathbb{N}^+$ but is typically small, $f_l = A_l(t)s_l(\varphi_l(t))$ satisfies (1.4), and $\Phi(t)$ is a mean zero random process that models noise or other stochastic quantity of interest. This model is also considered in [21]. Figure 1.4 gives an example of ANHM when $L = 2$. Even though there are really only two components, they are hard to distinguish. We shall see in Chapter 2 that examples of this type do occur in practice; we defer our discussion if how to deal with them to that chapter.

Lin et al. [27] proposed the De-shape algorithm to extract fundamental frequencies of constituent components of f satisfying (1.5), which incorporates the cepstrum idea into the STFT of a signal. We will explain this algorithm in more detail in Chapter 2.

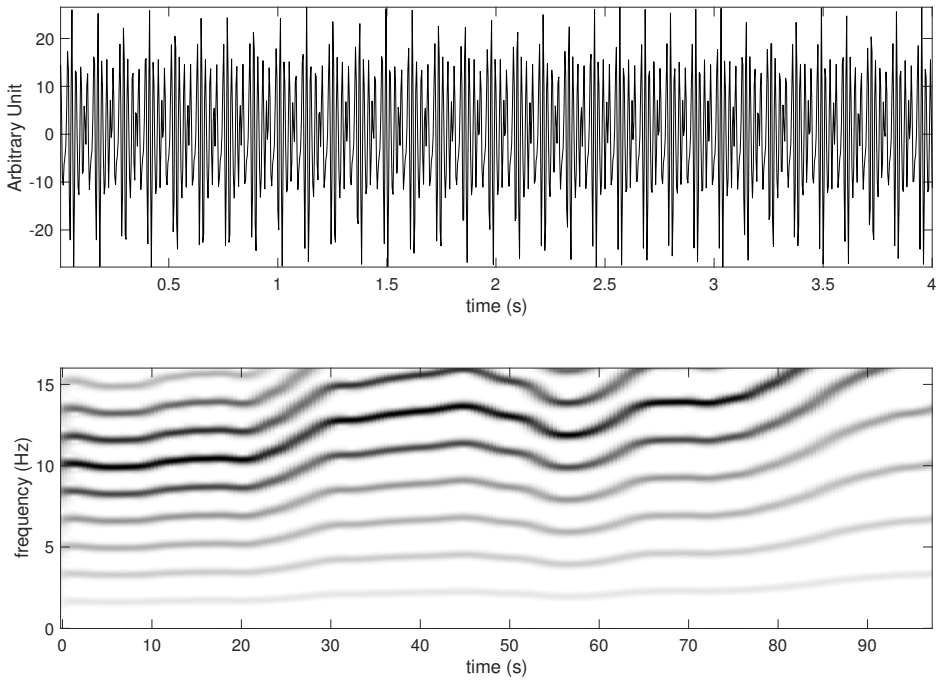

Figure 1.3: Top: plot of $f(t) = s(\phi(t))$ up to 4 seconds; bottom: the spectrogram of $f(t)$.

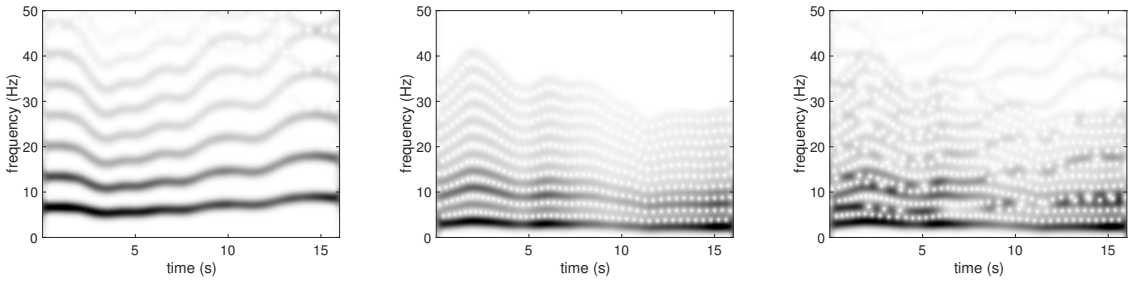

Figure 1.4: Left: STFT of $f_1 = A_1(t)s_1(\varphi_1(t))$; middle: STFT of $f_2 = A_2(t)s_2(\varphi_2(t))$; right: STFT of $f_1 + f_2$.

1.1 Shortcomings of these existing methods

Although SST and ConceFT are significant improvements on the spectrogram or, STFT, and De-shape decouples the fundamental frequency from the shape, they nevertheless fall short in some circumstances. We conclude this introductory chapter by briefly describing two such shortcomings to which we construct remedies in chapter 2 and 3.

When a signal is corrupted by noise. The logarithm of the STFT in the cepstrum can amplify the noise in a nonlinear way. Moreover, the inversion operation in the iSTCT would flip the noisy low-quefrency content into the high-frequency regime, which thus makes the final representation of fundamental IFs less clear. Figure 1.5 shows an example of the De-shape transform of an ta-mECG signal, where we can observe significant noise in the final TFR. Note that there are some light lines below 1.5Hz in the iSTCT, which are masked out in the de-shape STFT. It is clear that there are two curves in the de-shape STFT, one is around 1.5Hz, and one is around 2Hz. The curve around 1.5Hz is the maternal IHR, and the curve around 2Hz is the fetal IHR. To enhance the visibility, we only show the frequency up to 4 Hz. We will provide a new method to extract the fundamental IFs while avoiding the inversion operation in Chapter 2.

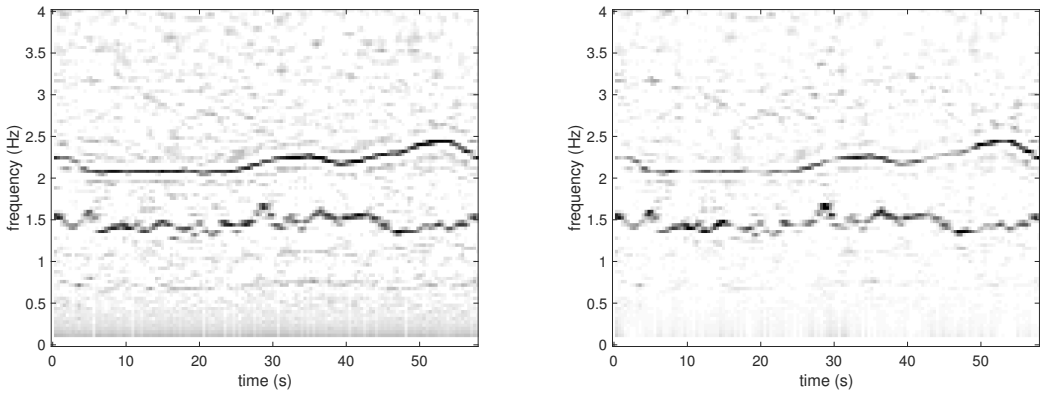

Figure 1.5: Left: the iSTCT of a ta-mECG signal f, $|U_f^{(h)}(t,\xi)|$. Right: the de-shape STFT of f, $|W_f^{(h)}(t,\xi)|^2$.

ConceFT is much sharper than SST, especially in noise. However, after the publication of [16], it was noticed that "chirping" portions of the signal f to be analyzed led to "thicker" representation curves in the TF-plane, as illustrated in Figure 1.6, where we show the SST and ConceFT of $f_i(t) = \cos[2\pi(\alpha_i(t - \frac{5}{2})^2 + 25t)]$, for $i = 1, 2, 3$, where $\alpha_1 = 0, \alpha_2 = 1$ and $\alpha_3 = 3$, and we use the Gaussian and the 1-st order Hermite function as basis function for ConceFT.

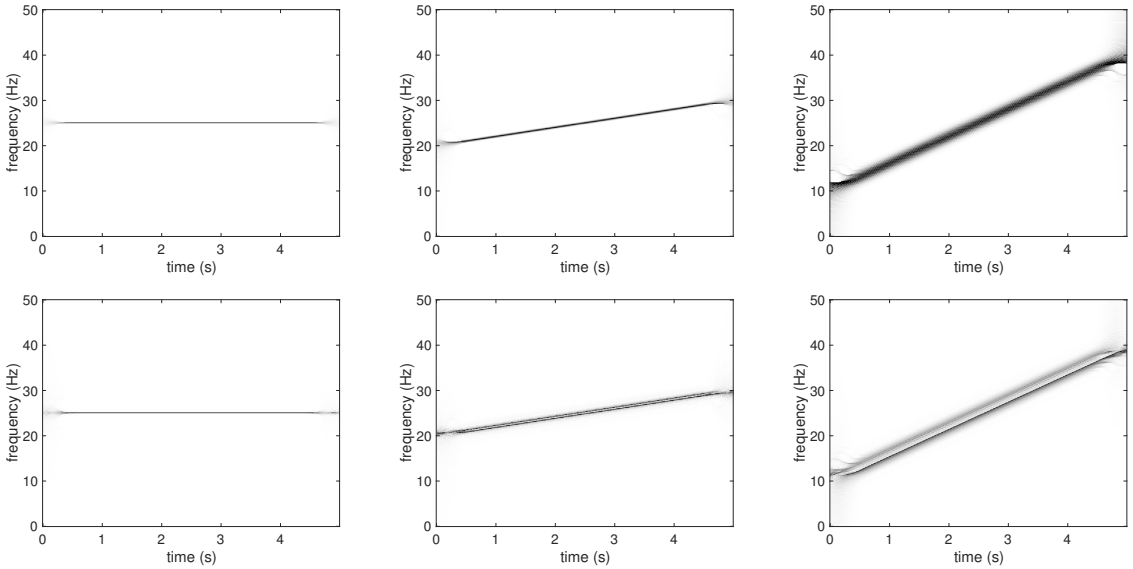

Figure 1.6: Top left: SST of f_1; top middle: SST of f_2; top right: SST of f_3; bottom left: ConceFT of f_1; bottom middle: ConceFT of f_2; bottom right: ConceFT of f_3.

In Chapter 3, we will provide a theoretical analysis that explains this phenomenon, and construct an approach that exploits geometric properties of the TF plane to circumvent its cause.

Chapter 2

Ramanujan de-shape transform

This chapter proposes a novel time-frequency (TF) analysis tool that fuses the short-time Fourier transform (STFT) and periodic transform (PT) [48].[1] Since many time series oscillate with time-varying frequency, amplitude and non-sinusoidal oscillatory pattern, a direct application of PT or STFT might not be suitable. However, we shall show that by combining them in a proper way, we obtain a powerful TF analysis tool. We first combine the Ramanujan sums and l_1 penalization to implement the PT. We call the resulting algorithm Ramanujan PT (RPT). The RPT is of its own interest for other applications, like analyzing short signal composed of components with integer periods, but that is not the focus of this chapter. Second, the RPT is applied to modify the STFT and generate a novel TF representation of the complicated time series that faithfully reflect the instantaneous frequency information of each oscillatory components. We coin the name for the proposed TF analysis Ramanujan de-shape (RDS) and vectorized RDS (vRDS). In addition to showing some preliminary analysis results on complicated biomedical signals, we provide theoretical analysis about RPT. Specifically, we show that the RPT is robust to three commonly encountered noises, including envelop fluctuation, jitter and additive noise.

2.1 Motivating example

Figure 2.1 shows a trans-abdominal maternal electrocardiogram (ta-mECG) signal.

In this example, the signal is clearly oscillatory, and we briefly summarize its characteristics.

[1] Our interest in using the PT in this context was first stimulated by the papers [67, 68, 56], by P.P.Vaidyanathan and collaborators; we note that our use of the PT differs from that in his approach.

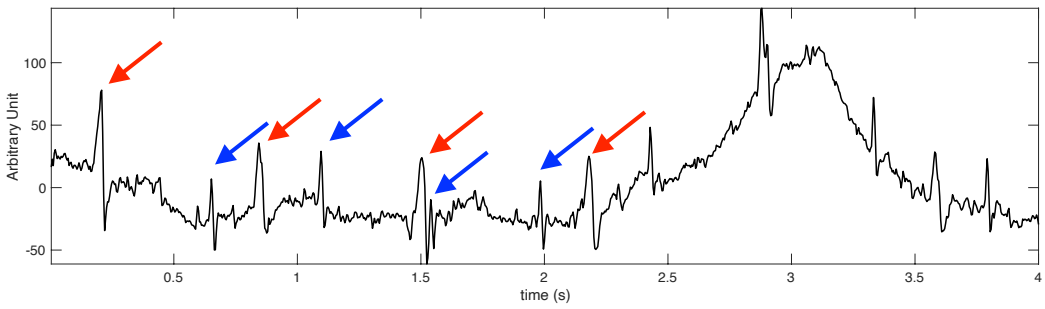

Figure 2.1: The ta-mECG signal sampled at 250Hz. The spikes indicated by red arrows are mECG, and those spikes indicated by blue arrows are fECG.

(C1) It is composed of two oscillations; one is the maternal ECG (mECG), and the other one is the fetal ECG (fECG). Moreover, there is a slowly varying trend, which is usually called the baseline wandering.

(C2) Although it is not easy to identify from the signal, according to physiological knowledge, the cycle-to-cycle period changes from time to time, both in mECG and fECG. This variation is usually known as the *heart rate variability* (HRV) [53].

(C3) The oscillation is far from sinusoidal, whose "shape" encodes the heart's electrophysiological information, like arrhythmia. Moreover, due to the nonlinear relationship between the cycle-to-cycle period and the ventricular electrophysiological dynamics, the cycle morphology changes from cycle to cycle as well [36]. This variation can be quantified as the QT interval variability [1].

(C4) The amplitude of each cycle changes due to the respiration-induced impedance variation [47].

These four characteristics are time-varying, and quantifications of these characteristics allow researchers or clinicians to understand more health-related information. There are many other signals sharing similar complicated structures, not only from medicine. We need a systematic signal processing tool to extract the information of interest to us. In this

chapter, we propose a novel time-frequency (TF) analysis tool aiming to extract how fast the signal oscillates at each moment.

In this chapter, we focus on the common challenge all these TF tools face when the signal does not oscillate sinusoidally, as is illustrated in (C3) above. Since the oscillation is not sinusoidal, in the frequency domain the oscillatory pattern is "automatically" decomposed into multiple oscillatory components via the Fourier series, and this "automatic" decomposition generates a lot of trouble when we interpret the output TFR. Let us take a look at this fact mathematically. Consider a function that oscillates regularly with a non-sinusoidal pattern that repeats every $1/\xi_0$ seconds, where $\xi_0 > 0$ can be viewed as the frequency of the oscillation, and the strength is $A > 0$. We represent the non-sinusoidal oscillatory pattern by a 1-periodic function s, and to simplify the discussion, we assume it has sufficient regularity so that it can be pointwise represented by its Fourier series; that is, $s(t) = \sum_{n=0}^{\infty} a_n \cos(2\pi n t + \alpha_n)$, where $a_n \geq 0$, α_n is the phase and $\alpha_0 = 0$. In this setup, the oscillatory signal can be written as

$$f(t) = As(\xi_0 t) = \sum_{n=0}^{\infty} A a_n \cos(2\pi n \xi_0 t + \alpha_n),$$

where each term $A a_n \cos(2\pi n \xi_0 t + \alpha_n)$ can be viewed as an oscillatory component, $n \geq 1$. By a simple calculation, we get the STFT with a window function g:

$$V_f^{(g)}(t,\xi) = A a_0 e^{-2\pi i t \xi} \hat{g}(\xi) + \frac{A}{2} \sum_{n \in \mathbb{Z}, n \neq 0} a_n e^{i \mathrm{sign}(n) \alpha_n} \hat{g}(\xi - n\xi_0) e^{2\pi i t (\xi - n\xi_0)}. \tag{2.1}$$

Clearly, we will see multiple components in the spectrogram, the squared magnitude of $V_f^{(g)}(t,\xi)$, as seen in Chapter 1.

To appreciate how this trouble impacts the interpretation for real data, see Figure 2.2 for the spectrogram of the ta-mECG shown in Figure 2.1. It is clear that there are various "curves" in the TF domain. Since we have ground truth information for this signal (the direct contact fECG is available in this database), we know that those curves indicated by blue arrows are associated with the mECG, and those light curves indicated by red arrows are associated with the fECG. These curves come from the non-sinusoidal oscillatory patterns of mECG and fECG.

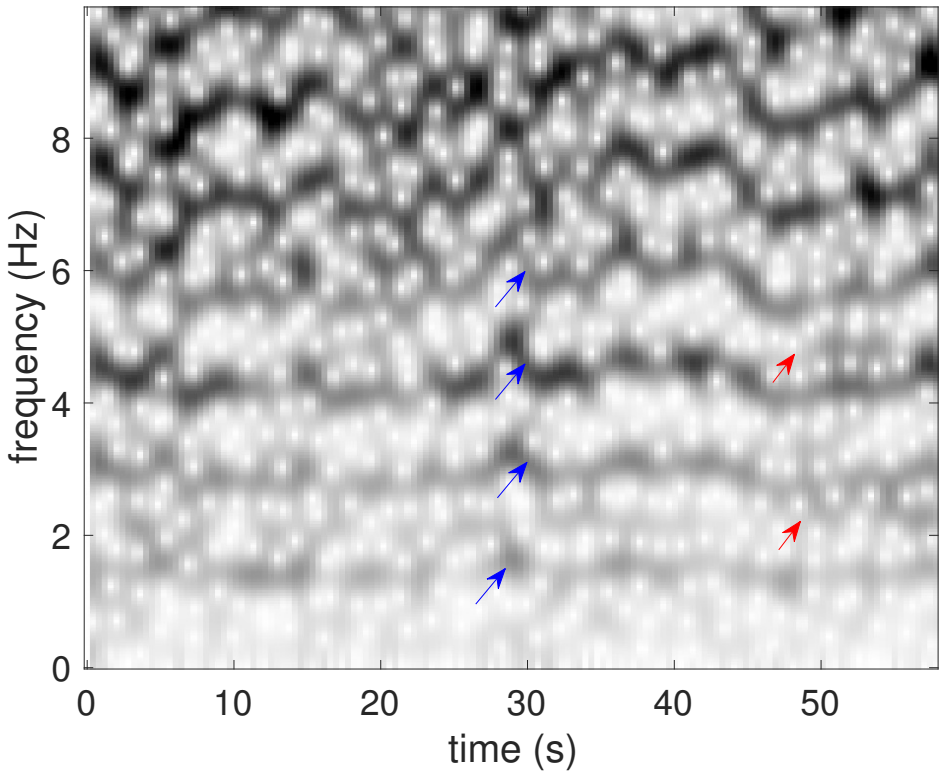

Figure 2.2: Top left: the magnitude of the STFT of the ta-mECG signal f shown in Figure 2.1, $|V_f^{(h)}(t,\xi)|$.

In practice, one is interested in getting the maternal instantaneous heart rate (IHR) and the fetal IHR for various clinical applications, like maternal stress detection [32], it is difficult to directly extract this information from the TFR. Note that IHR quantifies how fast the signal oscillates at each moment. (Although not shown, the scalogram and other TFRs face the same challenge.) A summary and comparison of different techniques of handling the single-channel ta-mECG is out of the scope of this chapter, and we refer readers with interest to [51] and citations therein.

A natural question to ask is if it is possible to come out with a TF analysis tool that is immune to the non-sinusoidal oscillatory patterns? In [27], the *de-shape* algorithm was introduced to handle this challenge. It modifies the well known cepstrum idea, called *inverse cepstrum*, to eliminate the impact of non-sinusoidal oscillatory pattern in the TFR. While the de-shape algorithm has been applied to study various biomedical signals, like the ta-mECG [50], the respiratory signal [33], and the sawtooth artifacts in the pulse transit time [28], it has several limitations. For example, when the oscillatory pattern is also time varying, the inverse cepstrum might not perform well; due to the interaction of the inverse cepstrum and the non-sinusoidal oscillation, the TFR from the de-shape algorithm might not correctly encode the oscillatory strength information. We will elaborate its limitations in more detail later in Section 2.3.2.

To resolve these limitations, we propose a novel TF analysis algorithm inspired by the periodic transform (PT) that has been actively studied in the signal processing society [48, 67, 68, 56, 59, 61]. Based on the nice properties of the Ramanujan sum and Ramanujan subspace [67, 68, 56, 59], we propose a l_1 minimization approach for the PT under the Ramanujan subspace, which we call the Ramanujan periodic transform (RPT). Based on the RPT, and a critical observation of the periodic structure in the spectrogram, we propose a novel TF analysis algorithm called the *Ramanujan de-shape* (RDS), and its vectorization version called the *vectorized Ramanujan de-shape* (vRDS). We also provide theoretical support for the RPT, particularly three robustness results. Specifically, we show that the RPT is robust to envelope fluctuation, jitter, and additive noise. These results explain the

performance of RDS and vRDS. We also demonstrate its performance by showing some preliminary results on real biomedical signals.

We will use following notations throughout this chapter. Denote $\mathbb{N}^+ = \{1, 2, \ldots\}$ be the set of positive natural numbers, and $\mathbb{N} = \mathbb{N}^+ \cup \{0\}$. (p, q) denotes the *greatest common divisor* of two integers p and q and *lcm* stands for *least common multiple*. For a real number x, $\lfloor x \rfloor$ denotes the largest integer no greater than x. For two integers p and q, $p|q$ denotes that p is a divisor of q. Given two sequences $f(n)$ and $g(n) \geq 0$, we say $f(n) = O(g(n))$ if there exists a constant $c_1 > 0$ such that $|f(n)| \leq c_1 g(n)$; $f(n) = \Omega(g(n))$ if there exists $c_2 > 0$ such that $|f(n)| \geq c_2 g(n)$; $f(n) = \Theta(g(n))$ if there exists c_1 and c_2 such that $c_1|g(n)| \leq |f(n)| \leq c_2|g(n)|$.

The ta-mECG shown in Figure 2.1 is a typical example of what we introduced in chapter 1 as an adaptive non-harmonic modeal, i.e., we have $L = 2$, and s_l captures the typical "P-QRS-T pattern" of the ECG signal. With this model, the signal processing challenge can be itemized to the following –

(Q1) how to estimate the maternal IHR $\varphi_1'(t)$ and fetal IHR $\varphi_2'(t)$ from $f(t)$?

(Q2) how to estimate the maternal AM $A_1(t)$ and fetal AM $A_2(t)$ from $f(t)$?

(Q3) how to estimate the maternal wave-shape dynamics s_1 and fetal wave-shape dynamics s_2 from $f(t)$?

(Q4) may we even decompose the ta-mECG ($f(t)$) to the mECG ($f_1(t)$) and the mECG ($f_2(t)$)? This question is called the *single channel blind source separation* (scBSS) problem since we only have one channel.

Note that (Q1)-(Q4) are typical questions we may ask for any other oscillatory time series, while the interpretation of these quantities depends on the background knowledge and purposes. In this study, we focus on answering question (Q1), which serves as the initial point to answer questions (Q2), (Q3) and (Q4) [51, 29].

Remark 1. *We have several remarks.*

1. *Although the ta-mECG can be modeled by the AHM, like the expansion shown in* (1.4)*, such an expansion would not be truly satisfactory. The "satisfaction" part is related to the usefulness of the information contained in the parametrization. In this ECG analysis (as well as in some other applications), how the signal oscillates provides important information about the system. Specifically, it is from the oscillatory pattern of an ECG signal that a physician can diagnose arrhythmia or other health issues. Therefore, for these signals, we should model how fast the signal oscillates separately from the oscillatory pattern itself, which means the ANHM is more useful than the AHM.*

2. *The model in (1.3) has been further generalized to capture the "time-varying oscillatory pattern" in [27, 74, 29]. See [27, 29] for more discussion about its physiological motivation and generalization. Among these generalized models, the one proposed in [29] is designed to further quantify the wave-shape dynamics mentioned in (Q3), and it has been applied to study the ultra-long time physiological time series [72]. Since taking these generalizations into account will not make a conceptual difference, we focus on the simple ANHM model in this chapter.*

3. *In practice there are trends in the signal that need to be modeled [8] as well. In this study, to simplify the discussion and focus on the main ideas, we focus on the ANHM considered in (1.5) and assume that the trend can be removed by traditional filtering techniques.*

2.2 Periodicity transform: old and new

We first review a relevant signal processing tool, the periodic transform (PT) [48], and propose a new implementation of the PT. In a nutshell, the PT is a time domain technique aiming to quantifying the oscillatory behavior of a given signal. It helps us obtain the periods of each oscillatory components. It is particularly useful when the periodicity is integer or can be well approximated by an integer [61], and when we have a short recording [56] so that frequency domain or TF domain techniques are limited. It has been applied to study various signals, ranging from music [49], video [44], to DNA sequence analysis [4, 5, 58].

The reason we discuss PT comes from the critical observation in Figure 1.3 in the Introduction. Recall that there is a repetition pattern in the frequency axis of spectrogram shown in Figure 1.3, where the period of the repetition pattern equals the fundamental frequency. This motivates us to consider the PT that aims to obtain the hidden periodicity, and hence the fundamental frequency. Specifically, as we will show in the next section, we will analyze the spectrogram at time t, $|V_f^{(h)}(t,\cdot)|$ shown in (2.1), by the PT.

Intuitively, if we can find a good dictionary encoding the periodicity information, then by decomposing the signal via the associated space in some special way, we can determine if the signal contains an oscillatory component and decide its periodicity. Such intuition is now known as the *Basis Pursuit* [6]. To realize this intuition, we need to find the space encoding the periodicity information. First, recall that a vector $v \in \mathbb{R}^n$ is called p-periodic, where $p \leq n$, if p is the smallest positive integer so that $v(j+p) = v(j)$ for any $j = 1, \ldots, n-p$. An intuitive space that encodes the information of period p can be defined in the following way.

Definition 1 (Periodic space [48]). *Fix $n \in \mathbb{N}^+$ and take the period $p \leq n$. The* periodic subspace *of period p of $\mathbb{R}^n$, denoted as $\mathcal{P}_p$, consists of p-periodic vectors, denoted as δ_p^s,*

$s = 0, 1, 2, \ldots, p-1$, *and defined by*

$$\delta_p^s(j) = \begin{cases} 1, & (j-s) \ mod \ p = 0; \\ 0, & otherwise. \end{cases}$$

We call δ_p^s *the p-periodic basis vector.*

Note that this basis of p-periodic subspace $\mathcal{P}_p$ is redundant in that $\mathcal{P}_{m_1 p} \cap \mathcal{P}_{m_2 p} = \mathcal{P}_p$, if m_1 and m_2 are mutually prime. This could make the estimation of periodicity fail since there is a strong correlation and overlap between subspaces $\mathcal{P}_{m_1 p}$ and $\mathcal{P}_{m_2 p}$. In [56, IV.A], this basis is called the *natural basis*, which is a special case of *nested periodic subspaces*.

To tackle this problem, Vaidyanathan [67, 68] considered the *Ramanujan sums* and the *p-periodic Ramanujan subspace* so that a p-periodic sequence can be uniquely decomposed into periodic components in the p-periodic Ramanujan subspace and those Ramanujan subspaces with periods being factors of p. We mention that Ramanujan sums has been applied to various problems, ranging from low frequency noise analysis [41], $1/f$ noise analysis [42], electrocardiogram signal [34], amino acid sequences [35], etc. Moreover, the Ramanujan subspace is also a special case of nested periodic subspaces, which contains several nice properties [56] compared with other nested periodic subspaces. For more theoretical details about nested periodic subspaces and its relationship with several other existing work, we refer readers with interest to [59]. We now briefly review the theory of Ramanujan sums and Ramanujan subspaces. More details about Ramanujan sums and Ramanujan subspaces and historical notes can be found in [67, 68, 56] and the citation therein.

Definition 2 (Euler totient function)**.** *The* Euler totient function $\phi(n)$*, where* $n \in \mathbb{N}^+$*, is defined as the number of positive integers* $m \in \mathbb{N}^+$*,* $m \leq n$*, such that* m *is coprime to* n*; that is,* $(m, n) = 1$*. The* totient summation function *is defined as*

$$\Phi(n) := \sum_{i=1}^{n} \phi(i).$$

Definition 3 (Ramanujan sum)**.** *For* $p \in \mathbb{N}^+$*, the pth Ramanujan sum is defined as*

$$c_p(n) = \sum_{\substack{k=1 \\ (k,p)=1}}^{p} e^{\frac{2\pi i k n}{p}},$$

where $n \in \mathbb{Z}$.

Note that there are $\phi(p)$ terms in the summation of $c_p(n)$ for all $n \in \mathbb{Z}$. Also, it is clear from the definition that $c_p(n) = c_p(n+p)$ for all $n \in \mathbb{Z}$. We list some useful properties of Ramanujan sums here:

Proposition 1 (Some properties of the Ramanujan sums)**.** *The Ramanujan sums satisfy the following properties:*

1. *[67, Corollary 1]* $c_p(n)$ *is an integer and* $c_p(n) \leq \phi(p)$ *for any* p *and* n *;*
2. *[67, Equation (9)]* $c_p(n) = c_p(-n)$ *for any* p *and* n *;*
3. *(Autocorrelation) [67, Theorem 7]* $\sum_{n=0}^{p-1} c_p(n)c_p(n-l) = pc_p(l)$ *for any* $l \in \mathbb{Z}$*;*
4. *(Orthogonality) [67, Equation (15)]* $\sum_{n=0}^{lcm(p,q)-1} c_p(n)c_q(n-l) = 0$ *for any* $l \in \mathbb{Z}$ *when* $p \neq q$.

Definition 4. *Define the* k*-th circular shift sequence of* $c_p(n)$ *as* $c_p^{(k)}(n)$*:*

$$c_p^{(k)}(n) := c_p(n-k),$$

where $n, k \in \mathbb{Z}$.

To detect a p-periodic component in a given signal, we consider the following $p \times p$ circulant matrix:

$$B_p := \begin{bmatrix} c_p(0) & c_p(p-1) & c_p(p-2) & \cdots & c_p(1) \\ c_p(1) & c_p(0) & c_p(p-1) & \cdots & c_p(2) \\ c_p(2) & c_p(1) & c_p(0) & \cdots & c_p(3) \\ \vdots & \vdots & \vdots & \ddots & \vdots \\ c_p(p-1) & c_p(p-2) & c_p(p-3) & \cdots & c_p(0) \end{bmatrix}$$

$$= \begin{bmatrix} c_p^{(0)}(0) & c_p^{(1)}(0) & c_p^{(2)}(0) & \cdots & c_p^{(p-1)}(0) \\ c_p^{(0)}(1) & c_p^{(1)}(1) & c_p^{(2)}(1) & \cdots & c_p^{(p-1)}(1) \\ \vdots & \vdots & \vdots & \ddots & \vdots \\ c_p^{(0)}(p-1) & c_p^{(1)}(p-1) & c_p^{(2)}(p-1) & \cdots & c_p^{(p-1)}(p-1) \end{bmatrix}.$$

Clearly B_p is a symmetric matrix due to Proposition 1 (2).

Proposition 2 (Properties of circulant matrix [67])**.** *The circulant matrix $B_p \in \mathbb{Z}^{p\times p}$ has some nice properties:*

1. *rank$(B_p) = \phi(p)$*
2. *any $\phi(p)$ consecutive columns of B_p are linearly independent.*
3. *the period of any vector in the column space of B_p is exactly p and cannot be smaller.*
4. *The column space of B_p is the same as that of the subspace spanned by $\phi(p)$ Fourier columns:*

$$\left\{ \begin{bmatrix} 1 \\ \omega_p^{k_i} \\ \omega_p^{2k_i} \\ \vdots \\ \omega_p^{(p-1)k_i} \end{bmatrix} \right\}_i, \quad (k_i, p) = 1, \quad 1 \le k_i \le p,$$

where $\omega_p = e^{\frac{-2\pi i}{p}}$.

Proposition 2 reminds us the usual definition of the discrete Fourier transform (DFT) matrix, which we remind the readers below.

Definition 5. *The $p \times p$ DFT matrix is defined as*

$$W_p = \begin{bmatrix} 1 & 1 & 1 & \cdots & 1 \\ 1 & \omega_p^1 & \omega_p^2 & \cdots & \omega_p^{p-1} \\ 1 & \omega_p^2 & \omega_p^{2\times 2} & \cdots & \omega_p^{2(p-1)} \\ 1 & \vdots & \vdots & \ddots & \vdots \\ 1 & \omega_p^{(p-1)} & \omega_p^{(p-1)\times 2} & \cdots & \omega_p^{(p-1)(p-1)} \end{bmatrix}.$$

Definition 6. *We need the following notations.*

1. *Denote the matrix formed by the first $\phi(p)$ columns of B_p by C_p.*

2. *Fix $N \in \mathbb{N}^+$. Let $C_{p,N}$ be an $N \times \phi(p)$ matrix defined as*

$$C_{p,N} = \begin{bmatrix} C_p \\ \vdots \\ C_p \\ R \end{bmatrix},$$

where R is the first $N - p\left\lfloor \frac{N}{p} \right\rfloor$ rows of C_p if $N - p\left\lfloor \frac{N}{p} \right\rfloor \neq 0$, and R is not needed if $N - p\left\lfloor \frac{N}{p} \right\rfloor = 0$.

3. *Denote the columns of $C_{p,N}$ by $c_{p,N}^{(0)}, c_{p,N}^{(1)}, \cdots, c_{p,N}^{(\phi(p)-1)}$ accordingly.*

Note that by a direct calculation, we have $B_p = V_p V_p^*$, where V_p is a $p \times \phi(p)$ submatrix of W_p whose columns are those $\phi(p)$ Fourier columns shown in Proposition 2 (4) [67]. By (2) of Proposition 2, C_p has full column rank and has the same column space as V_p. Moreover, $C_p^T C_p \in \mathbb{Z}^{\phi(p)\times\phi(p)}$ is positive definite. $C_{p,N}$ is designed to capture the p-periodic component inside a signal of length N by periodically extending C_p to length N with C_p repeated for $\left\lfloor \frac{N}{p} \right\rfloor$ times padded with R if needed. Note that $C_{p,N}^T C_{p,N}$ is always positive definite when $N \geq p$.

Definition 7 (Ramanujan subspace [67, 56])**.** *The* p-periodic Ramanujan subspace *of length N, denoted by $\mathcal{R}_{p,N}$, is defined to be the column space $C_{p,N}$; that is, the span of $\{c_{p,N}^{(0)}, c_{p,N}^{(1)}, \cdots, c_{p,N}^{(\phi(p)-1)}\}$.*

By construction, it is clear that the p-periodic Ramanujan subspace $\mathcal{R}_{p,N}$ is formed by fewer basis vectors than $\mathcal{P}_p$. We have the following important property of the Ramanujan subspace by (4) in Proposition 2.

Proposition 3 ([67, 68])**.** *For $p \neq q$ and for any sequence $x(n) \in \mathcal{R}_{p,N}$ and $y(n) \in \mathcal{R}_{q,N}$, there exists a constant $C_{p,q}$, which depends only on p and q, such that*

$$\left| \sum_{n=0}^{N-1} x(n)y(n) \right| \leq C_{p,q}.$$

To investigate a p-periodic signal, it is sufficient to look at the case when $N = p$,

Definition 8 ([67, 56])**.**

$$F_p := \begin{bmatrix} C_{p_1,p} & C_{p_2,p} & \cdots & C_{p_n,p} \end{bmatrix},$$

where p_i's are divisors of p with $1 = p_1 < p_2 < \cdots < p_n = p$.

By a well known property that $\sum_{p_i|p} \phi(p_i) = p$, we know that F_p is a $p \times p$ matrix.

Proposition 4 ([67, 56])**.** *We have that rank$(F_p) = p$. Moreover, F_p has the same column space as the $p \times p$ DFT matrix.*

Thus, any signal with period p can be uniquely expressed by a linear combination of columns of F_p. In other words, any p-periodic signal can be uniquely decomposed into Ramanujan subspaces corresponding to period p and its divisors. Therefore, it is likely to observe periods p_i that are divisors of p, when we decompose a p-periodic signal. Moreover, by the orthogonality property of the Ramanujan sums, we immediately have:

Corollary 1. *Following the notation in Definition 8, when N is a multiple of p, the column spaces associated with $C_{p_1,N}$, $C_{p_2,N}$, ..., $C_{p_n,N}$ are mutually orthogonal.*

2.2.1 Existing algorithms for PT

There have been many algorithms proposed for the PT. Those algorithms can be roughly classified into two categories. The first one is projecting the signal into the prescribed dictionary, and the second one includes those greedy-based algorithm [48], such as Small to Large algorithm, M-best algorithm, Best Correlation algorithm. In [48], the natural periodic subspaces $\mathcal{P}_p$ were chosen. The same algorithm can also be adapted to the setup of Ramanujan subspaces $\mathcal{R}_{p,N}$.

For the comparison purpose in the numerical section, we summarize these algorithms in terms of $\mathcal{R}_{p,N}$. Take a signal $x \in \mathbb{R}^N$ and a predetermined longest periods P_{max}. Given a predetermined threshold T, the Small to Large algorithm iteratively checks the existence

of periods, starting from the shortest period $p = 1$, and finish up to the maximal period P_{max}. During the iteration, if there exists $p \geq 1$ so that the orthogonal projection of x onto $\mathcal{R}_{p,N}$ has magnitude greater than T times the magnitude of x, we remove that component from x, get the residue r, and continue the algorithm with r. Note that $p = 1$ is related to the constant trend. To run the M-best algorithm, we need a prior estimate of the number of periods, M, that constitute x. The algorithm maintains a list of the M best periods and the corresponding basis elements. When a new (sub)period is detected that removes more energy from the signal than one currently on the list, the new one replaces the old, and the algorithm iterates until convergence. The Best Correlation algorithm also needs a predetermined number of periods M. This algorithm projects x onto all $\mathcal{R}_{1,N}, \ldots, \mathcal{R}_{P_{max},N}$, essentially measuring the correlation between x and the individual periodic basis elements. The period p with the largest correlation is then used for the projection. The selection of M is critical for the M-best algorithm and Best Correlation algorithm.

Vaidyanathan et al. also proposed to use the l^2 norm minimization to replace the l^1 norm in (2.2) [55, 56, 59]. In [61], the *integer MUltiple SIgnal Classification* (iMUSIC) algorithm is proposed, which follows the idea of minimizing the l^2 norm of the correlation vector of the periodic component with the noise eigenspace of the sample autocorrelation matrix of x [61]. However, these methods cannot guarantee a sparse estimation and spurious periods are possible. This might impede identifying the underlying periods.

2.2.2 Our proposed algorithm for PT

We now describe our approach of PT. Our approach is based on the following observation and assumption. Since many signals of practical interest consist of few periodic components, the *ideal* output of the PT encoding the underlying periodicity of the signal should be sparse. This sparsity requirement motivates us to implement the PT as a l_1-norm minimization problem. This sparsity idea has been mentioned in [55, 56, 59, 26], while our implementation is different from what have been proposed. Take a signal $y \in \mathbb{R}^N$. Fix a predetermined

upper bound of estimated periods, denoted as $P_{max} \in \mathbb{N}$. Consider

$$\min \|Dx\|_1 \quad s.t. \quad y = Ax, \tag{2.2}$$

where A is an $N \times \Phi(P_{max})$ dictionary defined as

$$A := \begin{bmatrix} C_{1,N} & C_{2,N} & \cdots & C_{P_{max},N} \end{bmatrix},$$

D is a diagonal penalty matrix whose i-th diagonal entry is $\zeta(P_i)$, where P_i is the period associated with the i-th column of A, and ζ is the chosen *positive* function describing how the optimization is penalized. We call ζ the *periodicity penalization function*. In [56, (32)], due to the inclination of PT in favor of long period via the dictionary approach, the quadratic penalization, $\zeta(x) = x^2$, is suggested. In other words, D suppresses high-period components since the components with longer periods are penalized more. In practice, if we have any prior knowledge about the period range, we can design a suitable periodicity penalization function. How to incorporate the prior knowledge depend on the application, and it is out of the scope of this work. Note (2.2) is similar to Basis Pursuit proposed in [6].

Next, we shall relax the condition $y = Ax$, particularly when the signal is corrupted by noise. So, instead of considering (2.2), we focus on the following program

$$\bar{x} \in \underset{x \in \mathbb{R}^{\Phi(P_{max})}}{\arg\min} \frac{1}{2} \|y - Bx\|_2^2 + \lambda \|x\|_1 , \tag{2.3}$$

where $B := AD^{-1}$ and $\lambda > 0$ is a tuning parameter. This is the l_1 penalized linear regression, also known as *Basis Pursuit Denoising* (BPDN) or Lasso, which was originally proposed in [63, 6]. This type of regression has been extensively studied, for example, in [76, 70, 66, 64]. We call the proposed algorithm for PT the *Ramanujan PT* (RPT). Note that a similar program involving the Ramanujan sums has also been experimented in [26] for music analysis with satisfactory results but with a more redundant dictionary and a different penalty matrix.

Recall that $z \in \mathbb{R}^{\Phi(P_{max})}$ is a subgradient of the l_1-norm $\|\cdot\|_1$ at $x \in \mathbb{R}^{\Phi(P_{max})}$, *i.e.*,

$z \in \partial \|x\|_1$, if

$$z_i = \begin{cases} 1, & x_i > 0\,; \\ -1, & x_i < 0\,; \\ \in [-1,1], & x_i = 0\,, \end{cases}$$

where $i = 1, \ldots, \Phi(P_{max})$. A subgradient for the function (2.3) being minimized is therefore $-B^T(y - Bx) + \lambda z$ for some $z \in \partial \|x\|_1$. Moreover, $\bar{x} \in \mathbb{R}^{\Phi(P_{max})}$ is a solution to (2.3) if and only if there exists a $\bar{z} \in \partial \|\bar{x}\|_1$, such that

$$B^T B\bar{x} - B^T y + \lambda \bar{z} = 0. \tag{2.4}$$

We know from [64, Lemma 1] that if x_1 and x_2 are both solutions to (2.3), then $Bx_1 = Bx_2$. Therefore, if $x_{1,i} = 0$ for $i \in G \subseteq \{1, 2, \ldots, \Phi(P_{max})\}$ and there exists a $z_1 \in \partial \|x_1\|_1$ such that $|z_{1,i}| < 1$ for $i \in G$, then $z_1 \in \partial \|x_2\|_1$ by (2.4), and we have $x_{2,i} = 0$ for all $i \in G$.

Since each Ramanujan subspace of period p has $\phi(p)$ basis vectors, we have the following definitions. The first definition is from [56, equation (22)],

Definition 9 (Energy of period)**.** *The energy of period of a vector $x \in \mathbb{R}^{\Phi(P_{max})}$, denoted as $EOP_x \in \mathbb{R}^{P_{max}}$, is defined as*

$$EOP_x(p) = \sum_{i=\Phi(p-1)+1}^{\Phi(p)} x_i^2\,.$$

Essentially, $EOP_x(p)$ summarizes how strong the signal x oscillates with the period p, since the $(\Phi(p-1)+1)$-th to the $\Phi(p)$-th bases captures the component oscillating with the period p. In this chapter, we also propose the following quantities for the upcoming algorithm and analysis.

Definition 10 (Intrinsic period)**.** *The intrinsic period (IP) of a vector $x \in \mathbb{R}^{\Phi(P_{max})}$ is a set defined as*

$$IP_x = \{p : EOP_x(p) > 0\}.$$

We define the IP so that the solution x to (2.3) tells us that the signal y contains an oscillatory component with p-periodicity if $p \in IP_x$. We further define their corresponding indices in the dictionary

Definition 11 (Support of periodicity)**.** *The support of periodicity (SOP) of a vector* $x \in \mathbb{R}^{\Phi(P_{max})}$ *is defined as*

$$SOP_x = \bigcup_{p \in IP_x} \{i : \Phi(p-1) + 1 \leq i \leq \Phi(p)\}.$$

Finally, we mention that when we have multiple realizations of the signal we have interest, we can easily generalize (2.3) to take all realizations into account. Suppose we have k signals, $y_1, \ldots, y_k \in \mathbb{R}^N$ with the same periodic components but different noise realizations, we can estimate the periodicity by

$$\bar{x} \in \underset{x \in \mathbb{R}^{\Phi(P_{max})}}{\arg\min} \frac{1}{2} \left\| Y - Bx\mathbf{1}^T \right\|_F^2 + \lambda \|x\|_1 \ ,$$

where $\mathbf{1}$ is a k-dim vector with all entries 1 and $Y = [y_1, \ldots, y_k] \in \mathbb{R}^{N \times k}$. We call this generalized algorithm vectorized RPT (vRPT).

2.3 Proposed time-frequency analysis algorithm

In this section, we summarize the existing de-shape algorithm and discuss its limitation. Then we introduce our proposed RDS and vRDS algorithms by taking the PT into account.

2.3.1 A critical observation of spectrogram

We start from recalling the STFT. Given a window function h, such as a Gaussian function centered at the origin, the STFT of f is defined as:

$$V_f^{(h)}(t,\xi) = \int_{\mathbb{R}} f(\tau)h(\tau - t)e^{-2\pi i\xi(\tau-t)}\,\mathrm{d}\tau,$$

where $t \in \mathbb{R}$ and $\xi \in \mathbb{R}$ indicate time and frequency respectively. We call $V_f^{(h)} : \mathbb{R}^2 \to \mathbb{C}$ a TFR of f. Usually, people call $|V_f^{(h)}(t,\xi)|^2$ the *spectrogram* of f, which is another TFR. The TFR depicts the spectral dynamics of the signal as time t evolves.

If we apply the STFT to analyze an oscillatory signal with non-sinusoidal oscillatory pattern modeled by (1.3), a critical observation is that there exists an oscillatory pattern in the frequency domain. A specific example is shown in (2.1), and see Figure 1.3 for an example of a simulated signal, and Figure 2.3 for an example of the fetal ECG signal shown in Figure 2.1. Recall that this pattern comes from the Fourier series expansion of the non-sinusoidal wave-shape function shown in (1.4). As is discussed in the Introduction, it is not easy to extract useful information from the TFR, even when we know the ground truth, not to say if we are blind to the ground truth.

2.3.2 Existing approach – De-shape algorithm

To handle the challenge shown above, Lin etc. [27] proposed the de-shape algorithm to eliminate the impact of non-sinusoidal oscillation of f satisfying (1.3). In a nutshell, by modifying the *cepstrum* idea [40] and incorporating it into the STFT, the de-shape algorithm modifies the STFT so that the resulting TFR looks like if the input signal oscillates with a sinusoidal oscillation. Below, we recall the cepstrum and summarize the de-shape algorithm.

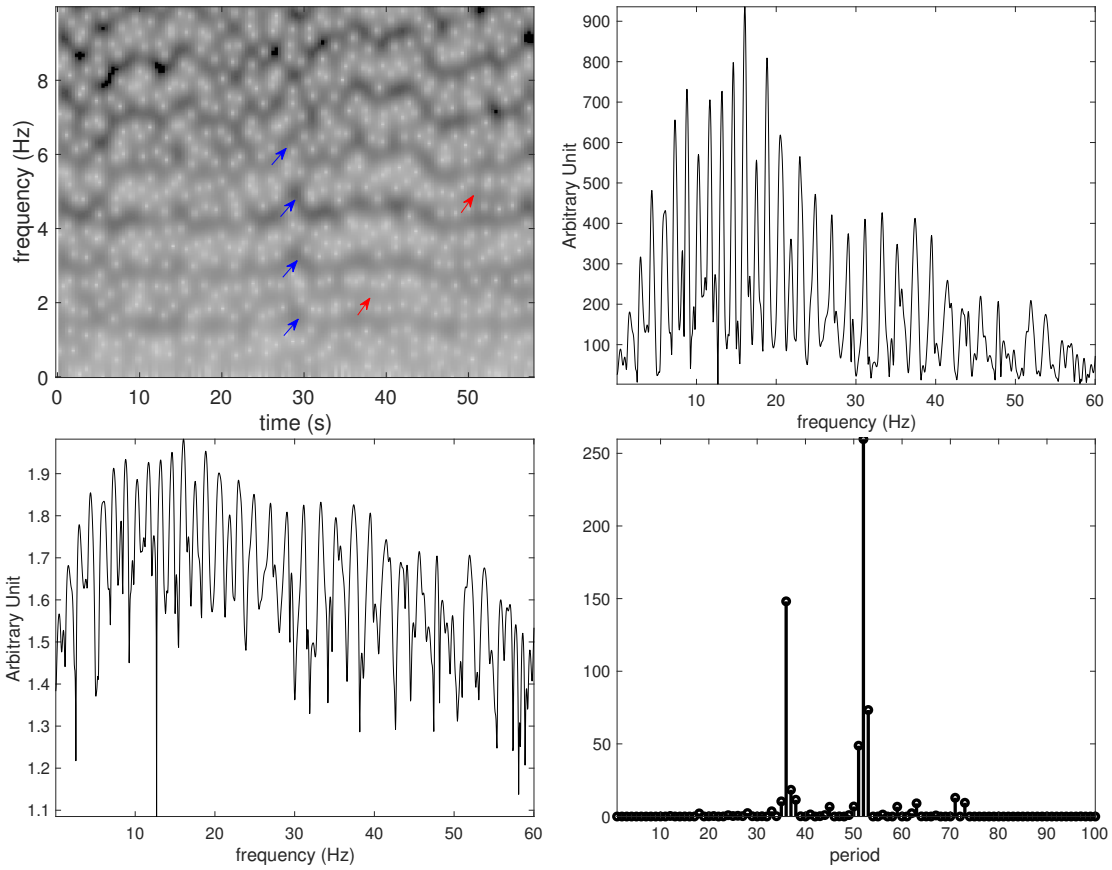

Figure 2.3: Top left: $|V_f^{(h)}(t,\xi)|^{0.1}$. top right: $|V_f^{(h)}(t_0,\cdot)|$, where $t_0 = 24.24$s. bottom left: $|V_f^{(h)}(t_0,\cdot)|^{0.1}$. bottom right: result of the proposed RPT on $|V_f^{(h)}(t_0,\cdot)|^{0.1}$.

Cepstrum is a widely-used technique that has been applied to various signal processing problems, such as pitch detection, deconvolution and speech recognition since its invention in 1963 [2]. The cepstrum f^C for a proper signal f is defined as

$$f^C(q) = \int_{\mathbb{R}} \log|\hat{f}(\xi)| e^{2\pi i q\xi}\, \mathrm{d}\xi,$$

where $\hat{f}(\xi)$ is the Fourier transform of f and $q \in \mathbb{R}$ is called *quefrency*, whose unit is the same as the unit of the original signal f. We refer interested readers to [40] for a review of cepstrum.

Clearly, like Fourier transform, cepstrum is a global operator, and the local dynamics cannot be directly captured by the cepstrum. Thus, in [27], the cepstrum is generalized to the *short-time cepstral transform (STCT)*, which is defined as

$$C_f^{(h)}(t,q) = \int_{\mathbb{R}} \log|V_f^{(h)}(t,\xi)| e^{2\pi i q\xi}\, \mathrm{d}\xi\,.$$

Since taking logarithm transforms the multiplication operation to the addition operation, taking logarithm decouples the amplitude modulation from the oscillation in $\log|V_f^{(h)}(t,\cdot)|$. Here, the amplitude modulation in $|V_f^{(h)}(t,\cdot)|$ comes from the Fourier series coefficients. To elaborate this important fact, take (2.1) as an example. Assume $\mathtt{supp}\hat{g}$ in (2.1) is sufficiently small so that $\mathtt{supp}\hat{g}(\xi - n\xi_0) \cap \mathtt{supp}\hat{g}(\xi - m\xi_0) = \emptyset$ when $n \neq m$. Thus,

$$|V_f^{(g)}(t,\xi)| = A a_0 |\hat{g}(\xi)| + \frac{A}{2} \sum_{n\in\mathbb{Z}, n\neq 0} |a_n||\hat{g}(\xi - n\xi_0)|\,.$$

This can be understood as

$$|V_f^{(g)}(t,\xi)| \approx E(\xi)\Big[\sum_{n\in\mathbb{Z}} |\hat{g}(\xi - n\xi_0)|\Big],$$

where E is a "low frequency" positive function so that $E(n\xi_0) = \frac{A|a_n|}{2}$ for $n \neq 0$ and $E(0) = A|a_0|$. We thus call $E(\xi)$ the *spectral envelope* of the wave-shape function. A rigorous treatment of this argument can be found in [27], particularly when f satisfies the ANHM. As a result, $\log|V_f^{(h)}(t,\xi)|$ becomes a summation of the logarithm of the spectral envelope $E(\xi)$, which oscillates slowly, and the logarithm of $\sum_{n\in\mathbb{Z}} |\hat{g}(\xi - n\xi_0)|$, which oscillates fast. In other words, $\log E(\xi)$ is in the low-quefrency domain and $\log\big[\sum_{n\in\mathbb{Z}} |\hat{g}(\xi - n\xi_0)|\big]$ is in

the high-quefrency domain. However, since taking the natural logarithm might be unstable numerically, the γ-power of $|V_f^{(h)}(t,\cdot)|$ is introduced to approximate the logarithm, where $\gamma > 0$ is a small constant, so that we can compute it in a more numerically stable way [27, 22, 65, 54]; that is, we consider

$$C_f^{(h,\gamma)}(t,q) = \int_{\mathbb{R}} |V_f^{(h)}(t,\xi)|^\gamma e^{2\pi i q\xi}\,\mathrm{d}\xi\,,$$

where $\gamma > 0$ is a small constant chosen by the user. As a result, if we ignore the low-quefrency content, we would obtain the fundamental IP (the inverse of the fundamental IF) and its multiples in $C_f^{(h,\gamma)}(t,\cdot)$. Note that in general the Fourier transform of $|V_f^{(h)}(t,\xi)|^\gamma$ should be understood in the distribution sense. See [27] for mathematical details.

Next, in order to extract the fundamental IF, we construct the *inverse short-time cepstral transform (iSTCT)* defined as

$$U_f^{(h,\gamma)}(t,\xi) = C_f^{(h,\gamma)}(t,1/\xi),$$

where the unit of ξ is in the frequency domain. The main motivation of this conversion comes from the relationship between period and frequency – the inverse of period is frequency. Hence, the inverse of the k-th multiple of the fundamental IP is the fundamental IF divided by k. Specifically, at time t, if there are peaks around ξ_0, $2\xi_0$, $3\xi_0$, etc, in $|V_f^{(h)}(t,\cdot)|^\gamma$, then we would observe peaks around $1/\xi_0$, $2/\xi_0$, $3/\xi_0$, etc, in $C_f^{(h,\gamma)}(t,\cdot)$, and hence ξ_0, $\xi_0/2$, $\xi_0/3$, etc, in $U_f^{(h,\gamma)}(t,\cdot)$. Consequently, the information shared by the STFT and the iSTCT is the fundamental IF. Thus, we can use $U_f^{(h,\gamma)}(t,\xi)$ as a mask for the spectrogram. Motivated by this fact, the de-shape STFT is defined as

$$W_f^{(h,\gamma)}(t,\xi) = V_f^{(h)}(t,\xi)U_f^{(h,\gamma)}(t,\xi), \tag{2.5}$$

and the final TFR containing only the fundamental frequency is given by $|W_f^{(h,\gamma)}(t,\xi)|^2$. Note that in general (2.5) should be understood in the distribution sense. For mathematical details, we refer readers with interest to [27].

Details of numerically implementation of de-shape STFT can be found in [33, 50]. Applications of the de-shape algorithm can be found, for example, in [11, 33, 50, 28, 25].

We mention that based on the STFT of f, one may further apply the sychrosqueezing transform [15] to sharpen the TFR $W_f^{(h,\gamma)}(t,\xi)$ or even concentration of frequency and time (ConceFT) [16] to alleviate the noise impact. We skip these steps to simplify the discussion.

While the de-shape algorithm has been applied to several problems [50, 33, 28], however, it has its own limitations.

(L1) The first trouble is the noise. By taking the γ power of $|V_f^{(h)}(t,\xi)|$, we might amplify the unwanted noise in a nonlinear way. Take the fetal ECG signal in Figure 2.1 as an example. Its iSTCT and de-shape STFT are displayed in Figure 1.5. While we can observe two dark curves in the de-shape STFT (the curve above 2Hz is the fetal IHR, and the other one below 2Hz is the maternal IHR), there are several artifacts around them.

(L2) Second, the inversion operation in the iSTCT would flip the noisy short-quefrency content into the high-frequency area. However, since the spectral envelope associated with the wave-shape function can be complicated, even when there is no noise, we generate complicated short-quefrency content in the STCT. Thus, a careful handle of the short-quefrency content is critical in the de-shape STFT framework.

(L3) Third, the de-shape STFT might not faithfully reflect the strength of the non-sinusoidal oscillation. Indeed, since the de-shape STFT comes from a direct entrywise multiplication of the STFT and its iSTCT (2.5), only the strength of the fundamental component will be preserved. For example, suppose we have two oscillatory signals of the same energy, $f_1(t) = As_1(\xi_0 t)$ and $f_2(t) = As_2(\xi_0 t)$, where $A > 0$ and $\|s_1\|_2 = \|s_2\|_2 = 1$, but $|\hat{s}_1(1)| \ll |\hat{s}_2(1)|$; that is, the fundamental component of s_1 is much weaker than that of s_1. In this case, the STFT of f_1 around ξ_0 will be much weaker than that f_2, and hence the de-shape STFT.

The above three issues might generate troubles when we interpret the results for scientific research. We thus propose a novel TF analysis tool motivated by these practical issues.

2.3.3 Proposed algorithm – Ramanujan de-shape

To handle the above-mentioned limitations (L1)-(L3), we consider the RPT. Note that in general PT is a global time-domain approach, we may not be able to capture the time-varying oscillatory pattern. Thus, in order to capture the time-varying period, or the IF, of our analyzed dataset, we apply the PT in the frequency domain. We coined the algorithm *Ramanujan de-shape* (RDS) algorithm if we apply the RPT, or vectorized RDS (vRDS) if we apply the vRPT.

We now describe the RDS and vRDS algorithms. From now on, we follow the convention and assume that the indices of vectors and matrices start at 1. Suppose the continuous signal f is sampled at uniform interval $\Delta_t > 0$, and we denote its discretization as $\mathbf{f} \in \mathbb{R}^N$, where $\mathbf{f}(n) = f(n\Delta_t)$, where $1 \leq n \leq N$; that is, we "record" the signal for $N\Delta_t$ long. Choose a discrete window function $\mathbf{h} \in \mathbb{R}^{2K+1}$, where $K \in \mathbb{N}$. For example, $\mathbf{h}$ can be a discretization of a Gaussian, so that $\mathbf{h}(K+1)$ is the center of the Gaussian. Fix $M \in \mathbb{N}$, and let $M+1$ be the number of bins in the frequency axis of our targeting TFR. We choose STFT to generate our targeting TFR. Then, the STFT of $\mathbf{f}$ would be a matrix $\mathbf{V_f} \in \mathbb{C}^{(M+1)\times N}$, whose entries are

$$\mathbf{V_f}(m,n) = \sum_{k=1}^{2K+1} \mathbf{f}(n+k-K-1)\mathbf{h}(k)e^{\frac{-2\pi i(k-1)(m-1)}{2M}},$$

where we define $\mathbf{f}(n) = 0$ when $n < 1$ or $n > N$, $n = 1, 2, \ldots, N$ is the time index, and $m = 1, 2, \ldots, M+1$ is the frequency index. For a fixed n, we apply the program (2.3) to each column of the matrix $\mathbf{V_f}(m,n)$, that is, the frequency axis, to obtain a matrix $\mathbf{X_f} \in \mathbb{R}^{\Phi(P_{max})\times N}$, where

$$\mathbf{X_f}(\cdot,n) \in \underset{x\in\mathbb{R}^{\Phi(P_{max})}}{\arg\min} \frac{1}{2}\left\| |\mathbf{V_f}(\cdot,n)|^\gamma - Bx \right\|_2^2 + \lambda\|x\|_1, \quad \gamma > 0.$$

The parameter γ should be chosen small enough like that in STCT in order to flatten the spectral envelope. The dictionary B is the same as in (2.3) with the chosen periodicity penalization function ζ and length $M+1$. We may only utilize the STFT with the corresponding frequency no more than a given maximal frequency f_{max}; that is, we only keep

the first $1+\lfloor \frac{f_{max}}{2M\Delta_t} \rfloor$ entries of $|\mathbf{V_f}(\cdot,n)|^\gamma$ and the dictionary B has $1+\lfloor \frac{f_{max}}{2M\Delta_t} \rfloor$ rows in the above minimization. We then transform $\mathbf{X_f}$ to a matrix $\mathbf{E_f} \in \mathbb{R}^{P_{max} \times N}$, where

$$\mathbf{E_f}(j,n) = EOP_{\mathbf{X_f}(\cdot,n)}(j)\,, \tag{2.6}$$

where $j = 1, \ldots, P_{max}$. Then, define $\mathbf{P_f}(m,n) \in \mathbb{C}^{(M+1)\times N}$ as

$$\mathbf{P_f}(m,n) = \begin{cases} \mathbf{E_f}(m,n) & 1 \le m \le P_{max}; \\ 0 & P_{max} < m \le M+1. \end{cases} \tag{2.7}$$

If we have a priori knowledge about the periods and the periodicity penalization function is designed properly, we may assign $\mathbf{P_f}(m,n)$ to be the final TFR; that is,

$$\mathbf{R_f}(m,n) = \mathbf{P_f}(m,n). \tag{2.8}$$

In general, when we do not have the prior knowledge about the period, the final TFR would be the entry-wise product

$$\mathbf{R_f}(m,n) = |\mathbf{V_f}(m,n)|^{\gamma'} \mathbf{P_f}(m,n)\,, \tag{2.9}$$

where $\gamma' > 0$ is a parameter that the user can choose. Indeed, since there is a nontrivial relationship between Ramanujan subspaces of periods p and p' when $(p,p') \neq 1$, it is possible that the RPT outputs spurious spikes in the divisors of the fundamental IF we have interest. Thus, we count on the STFT to "mask" those spurious spikes. This is possible since in the spectrogram, we have the fundamental IF and their multiples. The pseudo-code for RDS is shown in Algorithm 1.

The computational complexity of Algorithm 1 is $O(N(F(\lfloor \frac{f_{max}}{2M\Delta_t} \rfloor + 1) + M \log M))$, where $F(\lfloor \frac{f_{max}}{2M\Delta_t} \rfloor + 1)$ is the complexity of running the minimization at step 3 in the algorithm. Thus, if M is fixed and hence $F(\lfloor \frac{f_{max}}{2M\Delta_t} \rfloor + 1)$ is fixed, overall the computational complexity is $O(N)$.

In order to obtain a smoother TFR, instead of applying RPT at each time slot, we apply vRPT on the neighborhood of that time; that is, for each time index n and chosen $k \in \mathbb{N}$, we rather solve for

$$\mathbf{X_f}(\cdot,n) \in \underset{x \in \mathbb{R}^{\Phi(P_{max})}}{\arg\min} \frac{1}{2} \left\| |\tilde{\mathbf{V}}_\mathbf{f}(\cdot,n)|^\gamma - Bx\mathbf{1}^T \right\|_F^2 + \lambda \|x\|_1\,, \quad \gamma > 0,$$

Algorithm 1 Ramanujan de-shape (RDS)

INPUT: sampled signal $\mathbf{f}(n) \in \mathbb{R}^N$, window function $\mathbf{h}(n)$, P_{max}, f_{max}, λ, γ, γ', and the periodicity penalization function ζ;

OUTPUT: RDS $\mathbf{R_f}(m,n)$.

1: Compute the STFT $\mathbf{V_f}(m,n)$;

2: Set $\mathbf{T_f} \in \mathbb{C}^{(\lfloor \frac{f_{max}}{2M\Delta_t} \rfloor + 1) \times N}$, where $\mathbf{T_f}(m,n) = \mathbf{V_f}(m,n)$ for $1 \leq m \leq \lfloor \frac{f_{max}}{2M\Delta_t} \rfloor + 1$ and $1 \leq n \leq N$, and zero otherwise;

3: for n from 1 to N, solve for

$$\mathbf{X_f}(\cdot,n) \in \underset{x \in \mathbb{R}^{\Phi(P_{max})}}{\arg\min} \frac{1}{2} \left\| |\mathbf{T_f}(\cdot,n)|^\gamma - Bx \right\|_2^2 + \lambda \|x\|_1 ;$$

4: Obtain $\mathbf{E_f}(m,n)$ by $\mathbf{E_f}(j,n) = EOP_{\mathbf{X_f}(\cdot,n)}(j)$;

5: Extend $\mathbf{E_f}(m,n)$ to $\mathbf{P_f}(m,n)$;

6: $\mathbf{R_f}(m,n) = |\mathbf{V_f}(m,n)|^{\gamma'} \mathbf{P_f}(m,n)$ or $\mathbf{R_f}(m,n) = \mathbf{P_f}(m,n)$, depending on the prior knowledge.

where $\mathbf{1}$ is a $(2k+1)$-dim vector with all entries 1, $|\tilde{\mathbf{V}}_\mathbf{f}(\cdot,n)|^\gamma \in \mathbb{R}^{(M+1)\times(2k+1)}$, and

$$|\tilde{\mathbf{V}}_\mathbf{f}(\cdot,n)|^\gamma := \Big[|\mathbf{V_f}(\cdot,n-k)|^\gamma \quad \dots \quad |\mathbf{V_f}(\cdot,n)|^\gamma \quad \dots \quad |\mathbf{V_f}(\cdot,n+k)|^\gamma \Big],$$

except that the smallest time index would be 1 if $n-k<1$ and the largest time index would be N if $n+k>N$, and $\|\cdot\|_F$ is the matrix Frobenius norm. With $\mathbf{X_f}$, we can follow the same line as those from (2.6) to (2.9) to construct the final TFR, denoted as $\mathbf{VR_f}$. We call this proposed algorithm the vRDS, whose pseudo-code is shown in Algorithm 2. Note that when $k=0$, the vRDS is just RDS.

Algorithm 2 Vectorized Ramanujan de-shape (vRDS)

INPUT: sampled signal $\mathbf{f}(n) \in \mathbb{R}^N$, window function $\mathbf{h}(n)$, P_{max}, f_{max}, λ, γ, γ', number of time slots k, and the periodicity penalization function ζ;

OUTPUT: vRDS $\mathbf{VR_f}(m,n)$.

1: Compute the STFT $\mathbf{V_f}(m,n)$;

2: Set $\mathbf{T_f} \in \mathbb{C}^{(\lfloor \frac{f_{max}}{2M\Delta_t} \rfloor + 1) \times N}$, where $\mathbf{T_f}(m,n) = \mathbf{V_f}(m,n)$ for $1 \leq m \leq \lfloor \frac{f_{max}}{2M\Delta_t} \rfloor + 1$ and $1 \leq n \leq N$, and zero otherwise;

3: for n from 1 to N, solve for

$$\mathbf{X_f}(\cdot,n) \in \underset{x \in \mathbb{R}^{\Phi(P_{max})}}{\arg\min} \frac{1}{2} \left\| |\tilde{\mathbf{T}}_\mathbf{f}(\cdot,n)|^\gamma - Bx * \mathbf{1}^T \right\|_F^2 + \lambda \|x\|_1 ,$$

where

$$|\tilde{\mathbf{T}}_\mathbf{f}(\cdot,n)|^\gamma = \left[|\mathbf{T_f}(\cdot,n-k)|^\gamma \quad \dots \quad |\mathbf{T_f}(\cdot,n)|^\gamma \quad \dots \quad |\mathbf{T_f}(\cdot,n+k)|^\gamma \right];$$

4: Obtain $\mathbf{E_f}(m,n)$ by $\mathbf{E_f}(j,n) = EOP_{\mathbf{X_f}(\cdot,n)}(j)$;

5: Extend $\mathbf{E_f}(m,n)$ to $\mathbf{P_f}(m,n)$;

6: $\mathbf{VR_f}(m,n) = |\mathbf{V_f}(m,n)|^{\gamma'} \mathbf{P_f}(m,n)$ or $\mathbf{VR_f}(m,n) = \mathbf{P_f}(m,n)$, depending on the prior knowledge.

2.4 Numerical Results

In this section we illustrate the effectiveness of the proposed l_1 penalized PT and RDS on several examples. All the numerical examples (as well as those in previous sections) are generated in Matlab R2019a on a 2017 15-inch Macbook Pro with 16GB memory and 2.8 GHz Quad-Core Intel Core i7 processor. The l^1 penalized regression is based on Alternating Direction Method of Multipliers (ADMM) [3] in Matlab. The implementation of Small to Large algorithm, M-best algorithm, Best Correlation algorithm are downloaded from https://sethares.engr.wisc.edu/downloadper.html announced by the inventors of those algorithms. For the reproducibility purpose, the Matlab code is available upon requests.

2.4.1 Simulated signal

We start by considering two synthesized data. In the first example, we have two periodic signals $y_1(n)$ and $y_2(n)$ of length 500, where $y_1(n) = 5$ if n is a multiple of 15, and 0 otherwise; $y_2(n) = 8$ if n is a multiple of 21, and 0 otherwise. Take two white random processes ξ_n, η_n, $n = 1, \ldots, 250$ that are independently sampled from the uniform distribution on $(-0.3, 0.3)$. Generate $A_1, A_2 \in \mathbb{R}^{250}$ so that $A_1(n) = \xi_n$ if n is a multiple of 15, and 0 otherwise, and $A_2(n) = \eta_n$ if n is a multiple of 21, and 0 otherwise. We also set $A_1(15) = A_2(21) = 0$. Then $y_1(n)$ and $y_2(n)$ are pointwisely multiplied by $A_1(n)$ and $A_2(n)$ respectively, and set $y(n) = A_1(n)y_1(n) + A_2(n)y_2(n)$. To make the example more challenging, we further apply an envelope $E(n)$ to $y(n)$, where $E(n) = e^{\frac{-n^2}{250^2}}$. Then, we apply the proposed RPT to $\tilde{y}(n) = E(n)y(n)$, with $P_{max} = 50$, $\lambda = 1$ and the periodicity penalty function $\zeta(p) = p$. Results are shown in Figure 2.4. In the period estimation, we can find peaks at 15 and 21 as well as their divisors 3, 5 and 7. The arise of 3, 5, 7 is due to the fact that by Proposition 4, a p-periodic signal can contain components in Ramanujan subspaces $\mathcal{R}_{p_i,N}$, where p_i are divisors of p.

The second example is a signal with a series of Gaussian peaks of length 301. $y_1(n)$

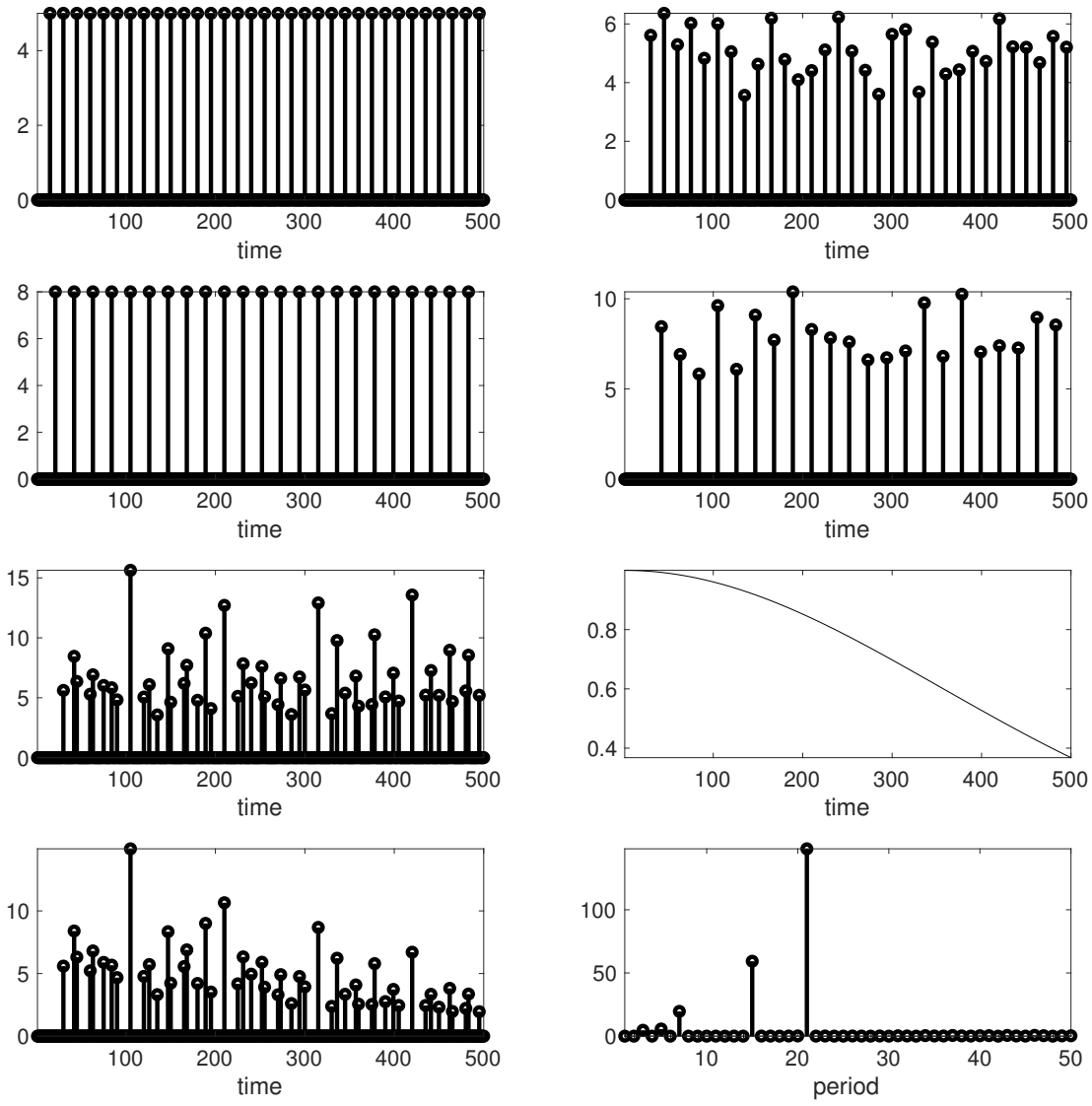

Figure 2.4: From left to right, top to bottom: $y_1(n)$, $A_1(n)y_1(n)$, $y_2(n)$, $A_2(n)y_2(n)$, $y(n)$, $E(n)$, $\tilde{y}(n)$, period estimation of $\tilde{y}(n)$.

and $y_2(n)$ are two periodic signals, where $y_1(n)$ is 27-periodic with Gaussian peaks centered at every 27 points with width 9 points; $y_2(n)$ is 17-periodic with Gaussian peaks centered at every 17 points with width 13 points, and both have peak values 3. Set ξ_n, η_n to be i.i.d. uniformly distributed on $(-0.2, 0.2)$ and $A_1(n) = \xi_n$ and $A_2(n) = \eta_n$. Define $E(n) := e^{\frac{-n^2}{(2\times 301)^2}}$ and $e(n)$ is i.i.d. Gaussian noise with standard deviation 1.11. Finally, set $y(n) = A_1(n)y_1(n) + A_2(n)y_2(n)$ and $\tilde{y}(n) = E(n)y(n) + e(n)$. The signal to noise ratior (SNR) is 5.21, where SNR is defined as $20\log\frac{\mathrm{std}(E(n)y(n))}{\mathrm{std}(e(n))}$. Figure 2.5 shows the result of the proposed RPT on $\tilde{y}(n)$ with $P_{max} = 50$, $\lambda = 0.5$ and $\zeta(p) = p^2$. We observe peaks at periods 17 and 27.

2.4.2 Trans-abdominal maternal ECG signal

We first show the RDS and the vRDS of the ta-mECG shown in Figure 2.1. This signal is from the 4th channel of the 17th recording of the Noninvasive Fetal ECG database for the PhysioNet Computing in Cardiology Challenge 2013 (CinC2013) [18],[2]. Each recording in this database contains 4 ta-mECG channels, and each channel is recorded for 60 seconds and sampled at 1000Hz. In this case, the signal is downsampled to 250Hz, that is, $\Delta_t = \frac{1}{250}$ second. We de-trend the signal by the standard median filter technique [12] for the ECG signal. In the STFT, each frequency bin is 0.04Hz, so there are $M = 3126$ frequency bins. To run the RDS and vRDS, we choose $P_{max} = 100$ (corresponds to 4Hz), $f_{max} = 60$Hz, $\zeta(p) = p^2$ as is suggested in [56, (32)], $\gamma = 0.1$, and $\gamma' = 1$. We choose $\lambda = 0.01$ for the RDS and $k = 1$ and $\lambda = 0.03$ for the vRDS. The result is shown in Figure 2.6. Note that in vRDS, each time we have 3 time slots in the minimization program, and hence the quadratic term in the convex program would be approximately 3 times larger than that of the RDS. Thus, the λ should be 3 times as that of the RDS for a fair comparison.

Second, we show that the PT is not suitable to analyze this kind of signal. In Figure 2.7, the results of RPT with different periodicity penalty functions are shown. (Left: the application of RPT with $\zeta(p) = 1$ and $\lambda = 5$. Middle: the application of RPT with

[2] https://physionet.org/content/challenge-2013/1.0.0/

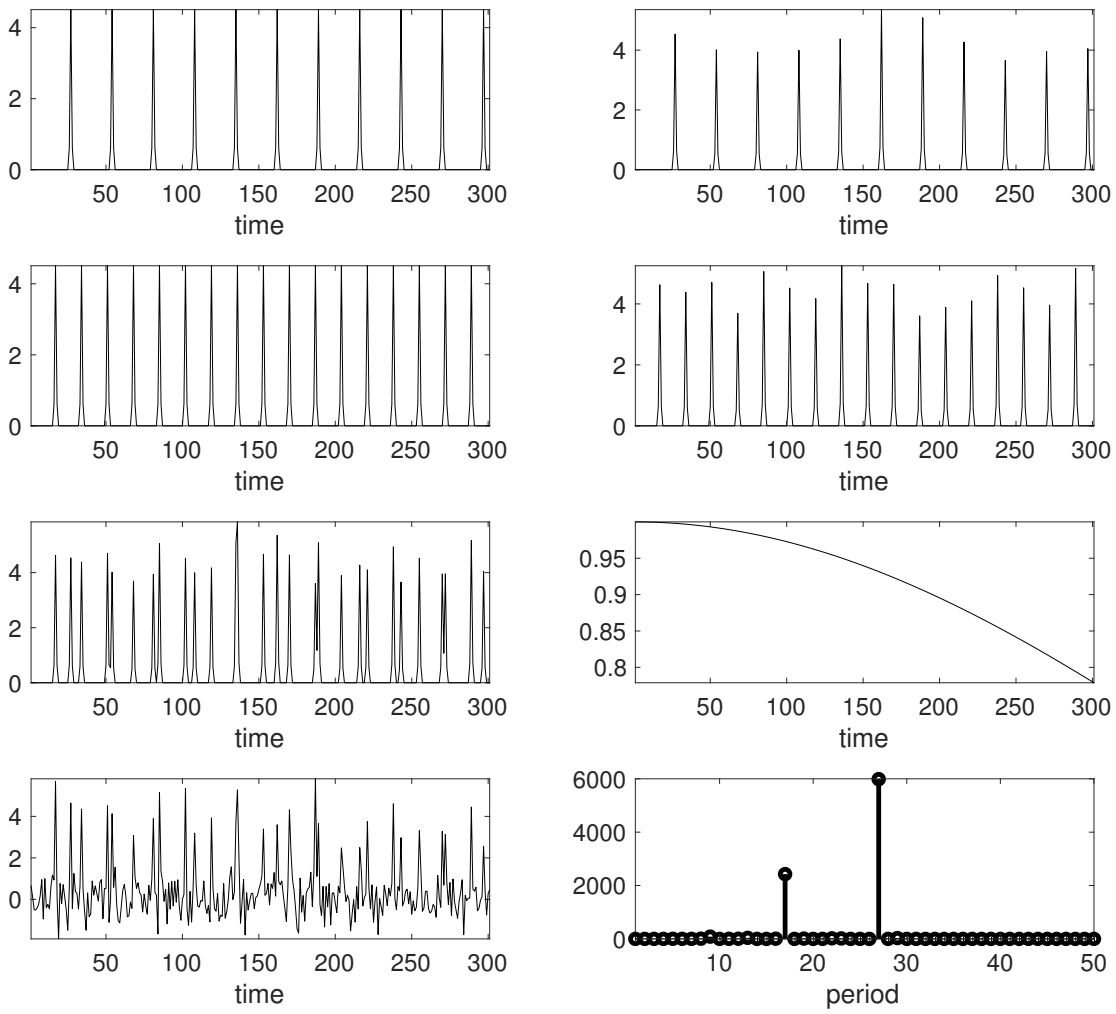

Figure 2.5: From left to right, top to bottom: $y_1(n)$, $A_1(n)y_1(n)$, $y_2(n)$, $A_2(n)y_2(n)$, $y(n)$, $E(n)$, $\tilde{y}(n)$, period estimation of $\tilde{y}(n)$

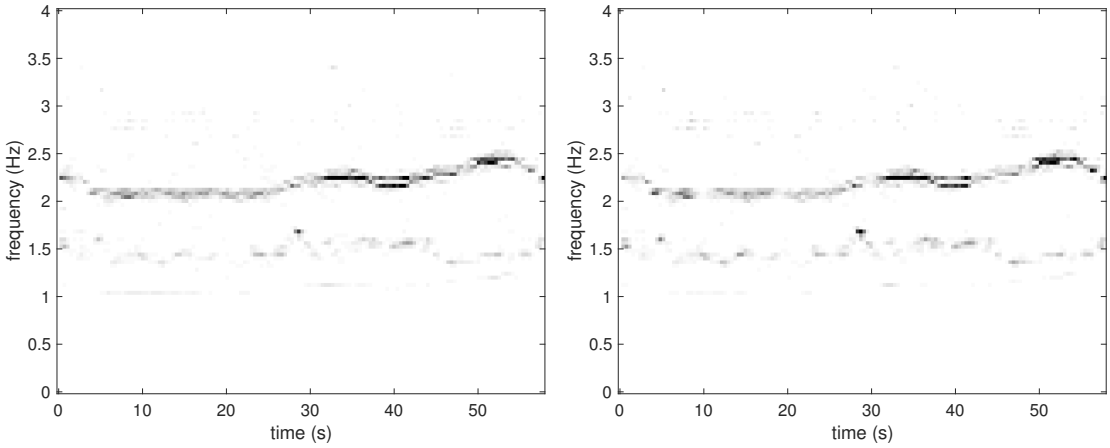

Figure 2.6: Left: the $\mathbf{P_f}$ of the ta-mECG signal f. Right: the Ramanujan de-shape (RDS) $\mathbf{R_f}$.

$\zeta(p) = p$ with $\lambda = 20$. Right: the application of RPT with $\zeta(p) = p^2$ with $\lambda = 5$. Since $\Delta_t = 1/250$ second, period p corresponds to frequency $250/p$ Hz.) In this example, we know that the maternal IHR is higher than 1.4Hz, so we take $P_{max} = 200$, which is related to $250/200 = 1.25$ Hz, to enhance the result. Note that due to the time-varying frequency and the global nature of the PT, there are several spikes in all results and it is not clear how to interpret the results.

Third, we show a comparison with other existing PT algorithms. We replace the RPT in Step 3 in Algorithm 1 by other existing PT algorithms, including the Small to Large algorithm, the M-Best algorithm and the Best correlation algorithm. We consider these algorithms since the benchmark code is available online in https://sethares.engr.wisc.edu/downloadper.html. See Figure 2.8 for the comparison. We set $P_{max} = 100$ in all cases. In the Small to Large algorithm, we observe that the threshold T should be very small otherwise no periodic component would be extracted. Thus, we set $T = 0.01$ which is close to the threshold when there is at least one output period and we can observe some artifacts in the high-frequency range. In the M-Best algorithm and the Best correlation algorithm, we assume that we know the number of oscillatory components, that is $M = 2$.

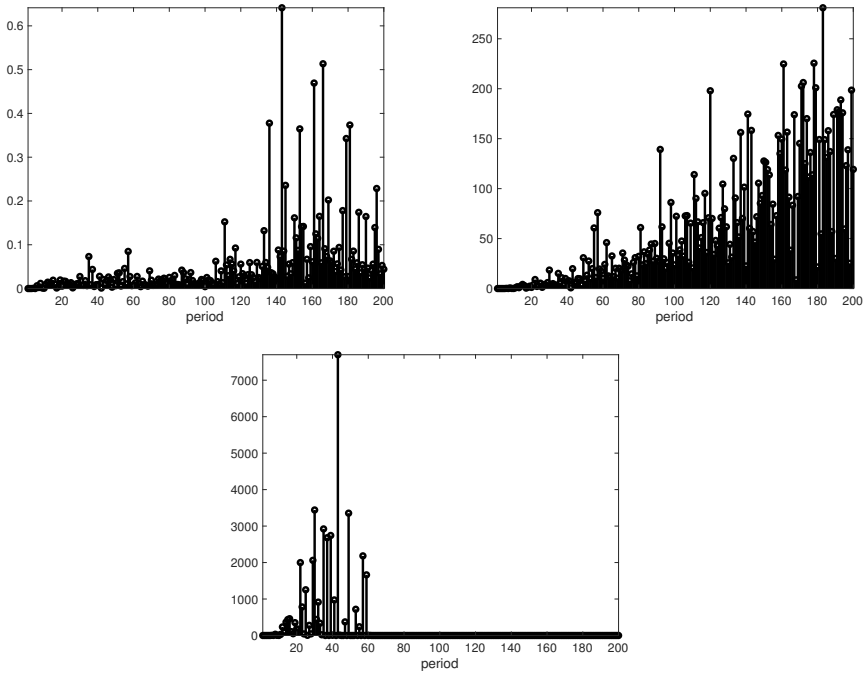

Figure 2.7: Application of the RPT on the ta-mECG signal f shown in Figure 2.1. As expected, due to the time-varying frequency, there are several spikes in all results.

Under this assumption, we can only observe one curve in the TFR. On the other hand, when $M = 3$, these algorithms tend to show the maternal IHR but vaguely. We thus show the results of these algorithm for $M = 3$.

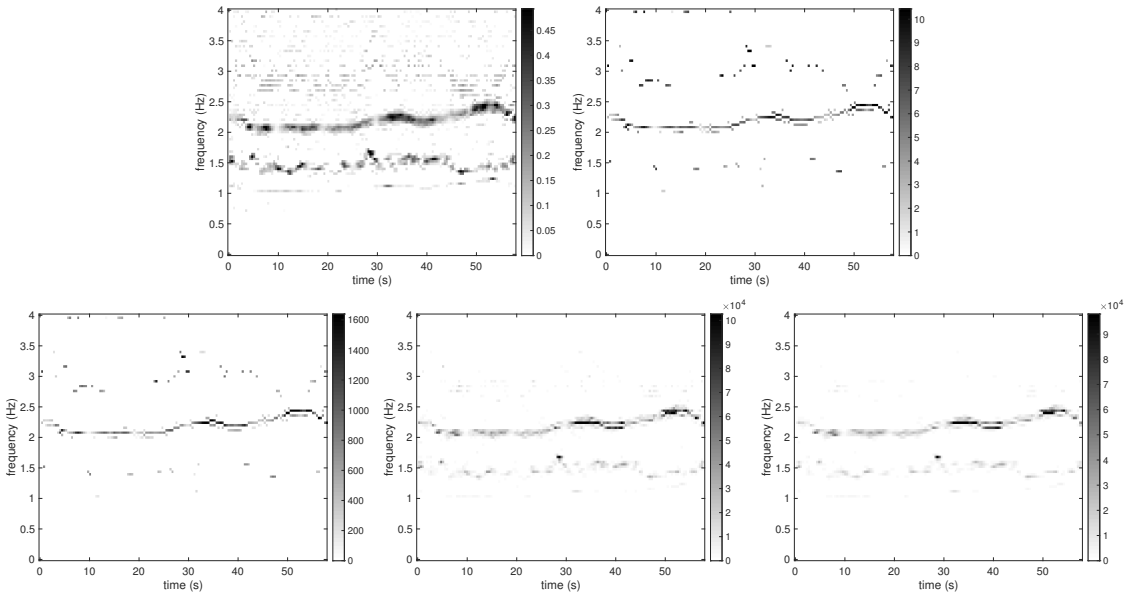

Figure 2.8: Top left: Small to Large. Top right: M-best. Second row left: Best correlation. Second row right: our RDS approach. Bottom row: vRDS approach.

Finally, we compare the RDS with the de-shape algorithm, and point out how the proposed RDS resolves the limitations of the de-shape STFT. We take the 2nd channel of the 31st recording of CinC2013 database. The signal is shown in Figure 2.9. Again, we can see that the ta-mECG has non-sinusoidal oscillation pattern. After downsampling the signal to 250 Hz and de-trending it as in the previous example, we apply the RDS, vRDS and the de-shape STFT. The result of de-shape STFT is shown in Figure 2.9 and those of RDS and vRDS are shown in Figure 2.10. Similar to what is shown in Figure 1.5, the de-shape STFT captures both the maternal IHR and fetal IHR, while the resulting TFR is corrupted by noise in the background. We then apply the RDS with $P_{max} = 100$ (corresponds to up to 4Hz), $f_{max} = 49$Hz and $\gamma = 0.1$. When $\lambda = 0.01$, we can successfully extract both the maternal IHR and the fetal IHR. Compared with the de-shape STFT, the

denoising effect of the RDS is clear. While less dramatic compared with the improvement of the RDS over the de-shape STFT, the vRDS can further stabilize the TFR. Therefore, the first and second limitations, (L1) and (L2), of de-shape STFT are resolved. When $\lambda = 0.03$, the fetal IHR is suppressed and the maternal IHR is kept. This is due to the property that the energy of the oscillatory signal is well preserved by the PT and the fact that the mECG has a larger energy than that of the fECG. Moreover, since the penalty matrix D penalizes more on high frequency, when we set a larger l_1 penalty, the fetal ECG is removed. This is an important feature in that we can more adaptively determine which component is associated with the mECG. Therefore, the third limitation, (L3), of the de-shape STFT is alleviated. We will explore its clinical value in the future work.

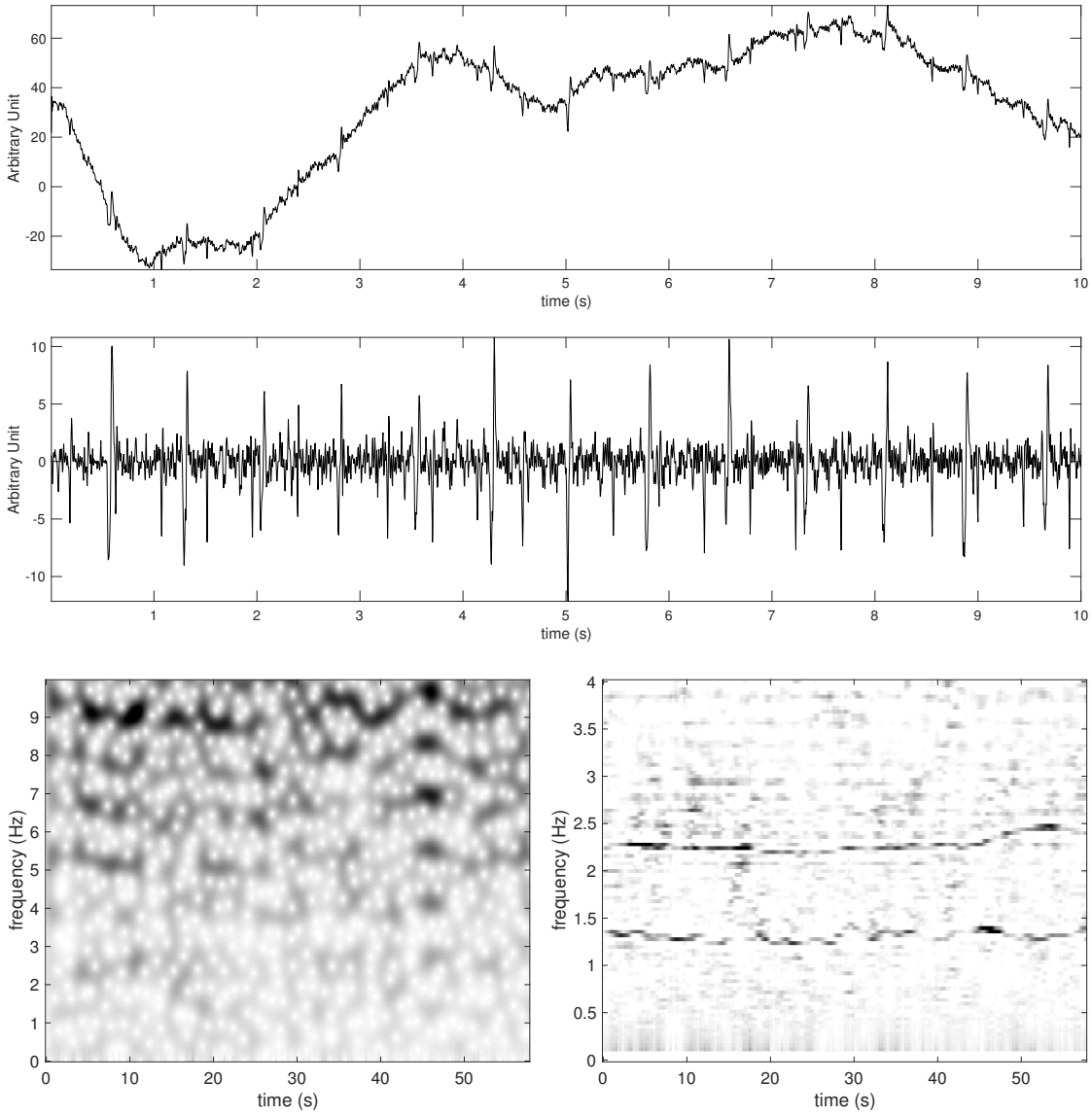

Figure 2.9: Top: ta-mECG signal. Middle: de-trended ta-mECG signal f. Bottom left: the spectrogram of f; Bottom right: the magnitude of the de-shape STFT of f.

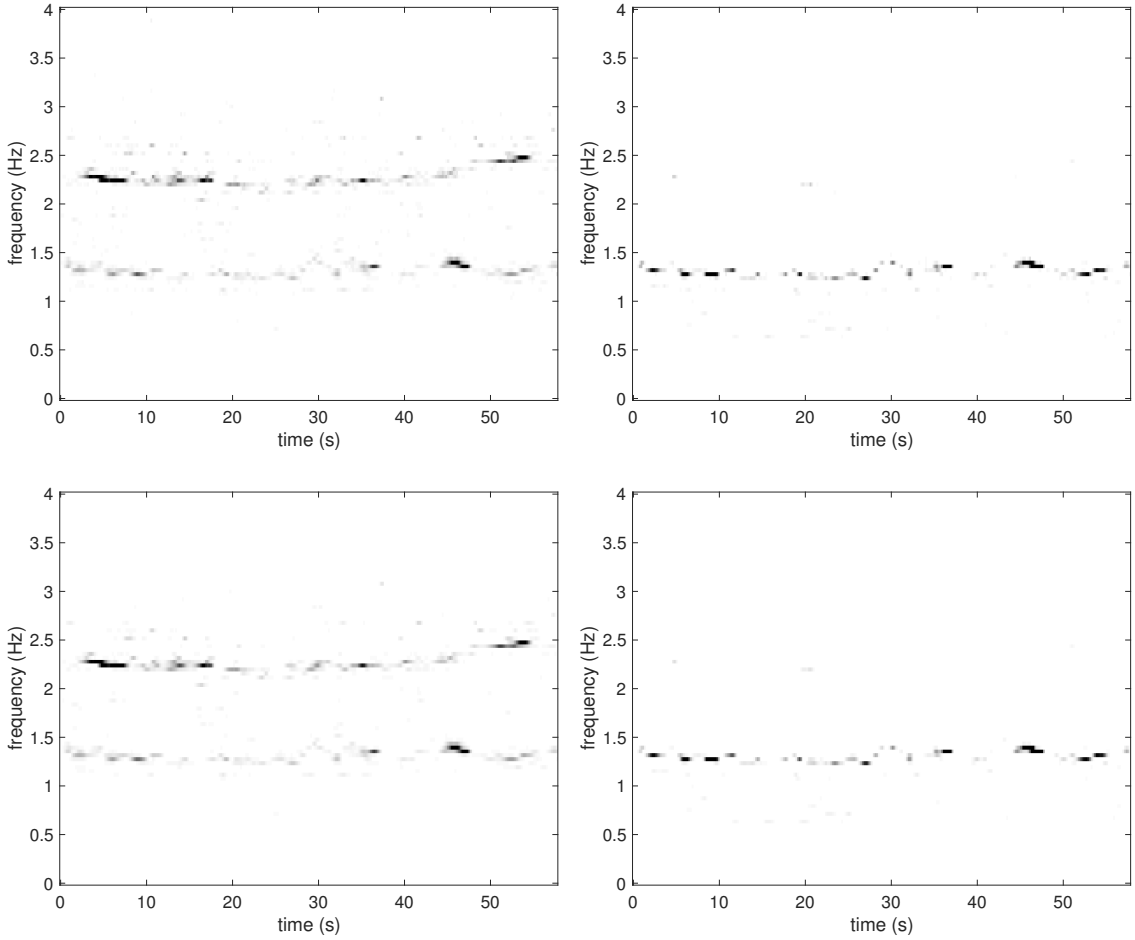

Figure 2.10: Top left: RDS of f when $\lambda = 0.01$; top right: RDS of f when $\lambda = 0.03$; Bottom left: vRDS of f, $k = 1, \lambda = 0.03$; bottom right: vRDS of f, $k = 1, \lambda = 0.09$.

2.5 Theoretical results

In this section, we theoretically analyze several natural questions associated with the proposed RPT, and hence the RDS. The analysis for vRPT is direct, and we omit it. First, the solution to (2.3) should be unique (the existence follows from [64, Lemma 1]); otherwise the construction of $\mathbf{X_f}$ would be meaningless. Second, this approach can accurately reveal the underlying periods (and hence the fundamental frequency) if the input signal, $|V_f^{(h)}(t,\cdot)|^\gamma$, is oscillatory but modulated by the spectral envelope and corrupted by noise. Third, it is also important to show that the RPT is robust to the jitter; that is, the oscillation happens around but not precisely on multiples of the period. Last, we want to better know the role of λ in the program.

We start with preparing some notation. Recall the notation A, B and D used in (2.3). Assume that a signal $y \in \mathbb{R}^N$ consists of l oscillatory components coming from $\mathcal{R}_{p_1,N}, \mathcal{R}_{p_2,N}, \ldots, \mathcal{R}_{p_l,N}$, where $1 \le p_1 < p_2 < \ldots < p_l$, so that

$$y = Bx^* = AD^{-1}x^*\,.$$

Suppose

$$Bx^* = B_S x_S^*,$$

where B_S is an $N \times (\sum_{i=1}^{l} \phi(p_i))$ submatrix of B with the column index $SOP(x^*)$, and x_S^* is a subvector of x^* with the index $SOP(x^*)$. Denote

$$x_S^* = \begin{bmatrix} x_{p_1}^* \\ \vdots \\ x_{p_l}^* \end{bmatrix},$$

where $x_{p_i}^* \in \mathbb{R}^{\phi(p_i)}$. Now, for $i = 1, \ldots, l$, set

$$b_{p_i,N}^{(k)} := \frac{1}{\zeta(p_i)} c_{p_i,N}^{(k)},$$

where $0 \le k \le \phi(p_i) - 1$. With the above setup, we thus have

$$y = \sum_{i=1}^{l} \sum_{j=0}^{\phi(p_i)-1} b_{p_i,N}^{(j)} x_{p_i}^*(j+1),$$

where at least one of the $x^*_{p_i}(j)$, $1 \le j \le \phi(p_i)$, for each p_i is nonzero. Throughout this chapter, we further assume that N is sufficiently large compared with p_l so that B_S has full column rank, according to Proposition 4. We mention that this is a reasonable and practical assumption since the signal should have enough length, compared to the underlying periods, so that we can be sure that there exists an oscillation. Under this assumption, we would have that $B_S^T B_S$ is invertible.

We use $IP^c_{x^*}$ to denote the complement set of IP_{x^*} in $\{1, 2, \ldots, P_{max}\}$ and S^c to denote the complement of the index set S in $\{1, 2, \ldots \Phi(P_{max})\}$. As a result, y can be written as

$$y = \begin{bmatrix} B_S & B_{S^c} \end{bmatrix} \begin{bmatrix} x^*_S \\ 0 \end{bmatrix}.$$

Define

$$M_{S,S} = \max_{\substack{i,j: \\ p_i,p_j \in IP_{x^*}}} \max \left\{ \left| \frac{\sum_{n=1}^{m} c^{(s)}_{p_i}(n) c^{(t)}_{p_j}(n)}{\zeta(p_i)\zeta(p_j)} \right| \;\middle|\; \begin{array}{l} 0 \le m \le lcm(p_i, p_j) - 1; \\ 0 \le s \le \phi(p_i) - 1; \\ 0 \le t \le \phi(p_j) - 1. \end{array} \right\},$$

and

$$M_{S,S^c} = \max_{\substack{i,j: \\ p_i \in IP_{x^*} \\ p_j \in IP^c_{x^*}}} \max \left\{ \left| \frac{\sum_{n=1}^{m} c^{(s)}_{p_i}(n) c^{(t)}_{p_j}(n)}{\zeta(p_i)\zeta(p_j)} \right| \;\middle|\; \begin{array}{l} 0 \le m \le lcm(p_i, p_j) - 1; \\ 0 \le s \le \phi(p_i) - 1; \\ 0 \le t \le \phi(p_j) - 1. \end{array} \right\}.$$

$M_{S,S}$ is the upper bound for the truncated correlation within $SOP(x^*)$, while M_{S,S^c} is the upper bound for the truncated correlation between columns in the $SOP(x^*)$ and those not in $SOP(x^*)$.

In the following analysis, we assume $P_{max} \in \mathbb{N}^+$ is fixed. Suppose $\tilde{y}$ is some noisy version of y. Below, we will show the robustness of the proposed Ramanujan-based PT algorithm, and see that the solution to

$$\arg\min_{x \in \mathbb{R}^{\Phi(P_{max})}} \frac{1}{2} \|\tilde{y} - Bx\|_2^2 + \lambda \|x\|_1 \tag{2.10}$$

could reveal those periods associated with y. We prepare some technical lemmas.

Lemma 1. *Let* $M = \max\{M_{S,S}, M_{S,S^c}\}$, λ_i *be the minimal eigenvalue of* $C_{p_i}^T C_{p_i}$ *and*

$$K := \min_i \left\lfloor \frac{N}{p_i} \right\rfloor \frac{\lambda_i}{\zeta^2(p_i)} - n_S M,$$

where $n_S := \sum_{i=1}^{l} \phi(p_i)$. *Then, the minimal eigenvalue of* $B_S^T B_S$ *has a lower bound* $\lambda_{min}(B_S^T B_S) \geq K$.

Proof. Write $B_S = \begin{bmatrix} B_1 & B_2 & \cdots & B_l \end{bmatrix}$, where $B_i = \frac{1}{\zeta(p_i)} C_{p_i,N}$. Then, $B_S^T B_S$ is an $l \times l$ block matrix whose (i,j)-th block is $B_i^T B_j$. Let $\tilde{B}_i$ be the upper $p_i \left\lfloor \frac{N}{p_i} \right\rfloor \times \phi(p_i)$ submatrix of B_i, and set H to be

$$H = \begin{bmatrix} \tilde{B}_1^T \tilde{B}_1 & & & \\ & \tilde{B}_2^T \tilde{B}_2 & & \\ & & \ddots & \\ & & & \tilde{B}_l^T \tilde{B}_l \end{bmatrix};$$

that is, a block diagonal matrix of the same size as $B_S^T B_S$ whose diagonal entries are $\tilde{B}_i^T \tilde{B}_i$. By definition, the minimum eigenvalue $\lambda_{min}(H)$ of H is

$$\lambda_{min}(H) = \min_i \left\lfloor \frac{N}{p_i} \right\rfloor \frac{\lambda_i}{\zeta^2(p_i)},$$

where $i = 1, 2, \ldots, l$. Denote

$$P := B_S^T B_S - H.$$

By the orthogonality property of the Ramanujan sums, any entry of P is either a truncated correlation within $SOP(x^*)$ (in diagonal blocks) or a truncated correlation between some column in the $SOP(x^*)$ and the other not in $SOP(x^*)$ (off diagonal block). Hence any entry of P is bounded by M so that $\|P\|_2 \leq (\sum_{i=1}^{l} \phi(p_i))M$. Therefore, by Weyl's inequality we have

$$|\lambda_{min}(B_S^T B_S) - \lambda_{min}(H)| \leq n_S M.$$

As a result, we have

$$\lambda_{min}(B_S^T B_S) \geq \lambda_{min}(H) - (\sum_{i=1}^{l} \phi(p_i))M = \min_i \left\lfloor \frac{N}{p_i} \right\rfloor \frac{\lambda_i}{\zeta^2(p_i)} - n_S M.$$

□

Since the term $n_S M$ does not depend on N and $p_1, \ldots, p_l$ are fixed, $\min_i \left\lfloor \frac{N}{p_i} \right\rfloor \frac{\lambda_i}{\zeta^2(p_i)} - n_S M$ grows asymptotically as N increases. Based on Lemma 1, we have

Lemma 2. *Suppose the signal length N is sufficiently large such that $K = \min_i \left\lfloor \frac{N}{p_i} \right\rfloor \frac{\lambda_i}{\zeta^2(p_i)} - n_S M > 0$. Then we have*

$$\left\| B_{S^c}^T B_S (B_S^T B_S)^{-1} \right\|_\infty \leq \frac{n_S^2 M_{S,S^c}}{K}.$$

Proof. Since $B_S^T B_S$ is positive definite when N is sufficient large, we have the eigen-decomposition as

$$B_S^T B_S = U \Lambda U^T = \begin{bmatrix} u_1 & u_2 & \cdots & u_{n_S} \end{bmatrix} \begin{bmatrix} \lambda_1 & & & \\ & \lambda_2 & & \\ & & \ddots & \\ & & & \lambda_{n_S} \end{bmatrix} \begin{bmatrix} u_1^T \\ u_2^T \\ \vdots \\ u_{n_S}^T \end{bmatrix},$$

where $U \in O(n_S)$, u_i is the i-th eigenvector associated with the i-th eigenvalue λ_i, and $\lambda_1 \geq \lambda_2 \geq \ldots \geq \lambda_{n_S} \geq K > 0$. Therefore,

$$(B_S^T B_S)^{-1} = \begin{bmatrix} u_1 & u_2 & \cdots & u_{n_S} \end{bmatrix} \begin{bmatrix} \frac{1}{\lambda_1} & & & \\ & \frac{1}{\lambda_2} & & \\ & & \ddots & \\ & & & \frac{1}{\lambda_{n_S}} \end{bmatrix} \begin{bmatrix} u_1^T \\ u_2^T \\ \vdots \\ u_{n_S}^T \end{bmatrix}.$$

Moreover, let

$$B_S = \begin{bmatrix} \tilde{b}_1 & \tilde{b}_2 & \ldots & \tilde{b}_{n_S}, \end{bmatrix}$$

and the m-th row of $B_{S^c}^T$ be denoted as a^T, where a is the m-th column of B_{S^c}. Then, the (m,k)-th entry of $B_{S^c}^T B_S (B_S^T B_S)^{-1}$ is equal to

$$\begin{bmatrix} a^T \tilde{b}_1 & \ldots & a^T \tilde{b}_{n_S} \end{bmatrix} \begin{bmatrix} \frac{1}{\lambda_1} u_1 & \ldots & \frac{1}{\lambda_{n_S}} u_{n_S} \end{bmatrix} \begin{bmatrix} u_{1,k} \\ \vdots \\ u_{n_S,k} \end{bmatrix} = \sum_{j=1}^{n_S} \sum_{i=1}^{n_S} \frac{1}{\lambda_j} a^T \tilde{b}_i u_{j,i} u_{j,k},$$

where $u_{i,j}$ is the j-th entry of u_i. Hence, the l^1 norm of the m-th row of $B_{S^c}^T B_S (B_S^T B_S)^{-1}$ is $\sum_{k=1}^{n_S} \left| \sum_{j=1}^{n_S} \sum_{i=1}^{n_S} \frac{1}{\lambda_j} a^T \tilde{b}_i u_{j,i} u_{j,k} \right|$, and

$$\begin{aligned}
\sum_{k=1}^{n_S} \left| \sum_{j=1}^{n_S} \sum_{i=1}^{n_S} \frac{1}{\lambda_j} a^T \tilde{b}_i u_{j,i} u_{j,k} \right| &\leq \frac{1}{K} \sum_{k=1}^{n_S} \sum_{j=1}^{n_S} \sum_{i=1}^{n_S} \left| a^T \tilde{b}_i \right| \left| u_{j,i} \right| \left| u_{j,k} \right| \quad \text{(by Lemma 1)} \\
&\leq \frac{M_{S,S^c}}{K} \sum_{k=1}^{n_S} \sum_{i=1}^{n_S} (\sum_{j=1}^{n_S} \left| u_{j,i} \right| \left| u_{j,k} \right|) \\
&\leq \frac{M_{S,S^c}}{K} \sum_{k=1}^{n_S} \sum_{i=1}^{n_S} 1 \quad \text{(by Cauchy-Schwarz)} \\
&= \frac{n_S^2 M_{S,S^c}}{K}.
\end{aligned}$$

Therefore,

$$\left\| B_{S^c}^T B_S (B_S^T B_S)^{-1} \right\|_\infty \leq \frac{n_S^2 M_{S,S^c}}{K}.$$

□

Note that since n_S and M_{S,S^c} are fixed and $K = \Theta(N)$ when $N \to \infty$, $\left\| B_{S^c}^T B_S (B_S^T B_S)^{-1} \right\|_\infty = O(N^{-1})$ when $N \to \infty$. We proceed to prove the main theorems using the technique similar to the Primal-Dual Witness construction in [70], where $\left\| B_{S^c}^T B_S (B_S^T B_S)^{-1} \right\|_\infty < 1$ is presumed and the probability of successful support recovery by Lasso under additive Gaussian noise is estimated.

Theorem 1 (Robustness to envelope perturbations)**.** *Suppose N is sufficiently large such that $K > n_S^2 M_{S,S^c}$ and $\tilde{y} = Ey$, where $E = diag(e_1, e_2, \ldots, e_N)$ is the envelope. Let*

$$M_{S,y}^1 := \left\| B_{S^c}^T (I - B_S (B_S^T B_S)^{-1} B_S^T) \right\|_\infty \|y\|_\infty \tag{2.11}$$

and

$$M_{S,y}^2 := \left\| (B_S^T B_S)^{-1} B_S^T \right\|_\infty \|y\|_\infty . \tag{2.12}$$

Then, if

$$\max_i |e_i - 1| < \frac{\lambda}{M_{S,y}^1} \left(1 - \frac{n_S^2 M_{S,S^c}}{K} \right), \tag{2.13}$$

where $\lambda > 0$ is the chosen penalty in (2.10), the program (2.10) has a unique solution $\hat{x}$ such that if $\hat{x}_i \neq 0$, then $i \in SOP(x^*)$.

Moreover, if for $i = 1, 2, \ldots, l$ we denote

$$\beta_i := \max_j |x^*_{p_i}(j)|\,, \tag{2.14}$$

then the solution $\hat{x}$ can successfully identify periods p_i when β_i satisfies

$$\beta_i > \max_i |e_i - 1| \cdot M^2_{S,y} + \lambda \left\| (B_S^T B_S)^{-1} \right\|_\infty . \tag{2.15}$$

Before proving the theorem, let us have a closer look at this theorem. First, if $E = I$, that is, when there is no envelop variation, $\max_i |e_i - 1| = 0$. Thus, for any $\lambda > 0$, the program (2.10) always has a unique solution $\hat{x}$ such that $SOP(\hat{x}) \subseteq SOP(x^*)$, so there is no spurious period detected. Moreover, if λ is sufficiently small such that $\lambda < \frac{\min_i \beta_i}{\left\| (B_S^T B_S)^{-1} \right\|_\infty}$, we can detect all the periods p_i, $1 \le i \le l$.

Second, (2.11) might rings the bell that $B_S(B_S^T B_S)^{-1} B_S^T \tilde{y}$ is the solution of minimizing $\min_{x_S} \|\tilde{y} - B_S x_S\|_2$. Thus, $B_{S^c}^T (I - B_S(B_S^T B_S)^{-1} B_S^T)\tilde{y}$ is quantifying the deviation of $\tilde{y}$ from y using the basis not indexed by S. However, as we will see in the proof, (2.11) comes from controlling $\tilde{y} - y$ instead of $\tilde{y}$.

Third, for fixed coefficients $x^*_{p_i}(j)$, $\|y\|_\infty$ is fixed. Hence by the definition of B_S and B_{S^c}, it is clear that $M^1_{S,y} = \Theta(N)$, and $M^2_{S,y} = \Theta(1)$ when $N \to \infty$. So, if the strength of envelope modulation $\max_i |e_i - 1|$ is fixed in (2.13), to ensure the uniqueness solution of (2.10) and to avoid spurious periods, λ should be $\Omega(N)$. This result provides a rule-of-thumb criterion to choose λ when we solve the program.

Finally, note that $\left\| (B_S^T B_S)^{-1} \right\|_\infty = \Theta(\frac{1}{N})$, and a bound for $\left\| (B_S^T B_S)^{-1} \right\|_\infty$ is $\left\| (B_S^T B_S)^{-1} \right\|_\infty \le \frac{1}{K}$, which can be proved in a way similar to that of Lemma 2 by using its eigenvalue decomposition. As a result, by (2.15), the lower bound for β_i in order to to successfully identify the period p_i is $\Theta(\frac{\lambda}{N})$.

Proof. To study (2.10), we first look at the following restricted problem:

$$\arg\min_{x \in \mathbb{R}^{n_S}} \frac{1}{2} \|\tilde{y} - B_S x\|_2^2 + \lambda \|x\|_1 \,, \tag{2.16}$$

where $\lambda > 0$. By the assumption, B_S is of full rank, and hence we have $B_S^T B_S$ is invertible. Therefore, the minimized function in (2.16) is strictly convex and the solution $\hat{x}_S$ to (2.16)

is unique. Let

$$\hat{z}_S = \frac{1}{\lambda}(B_S^T\tilde{y} - B_S^T B_S\hat{x}_S)$$

be a subgradient of $\|x\|_1$ at $\hat{x}_S$ by (2.4). Set $\hat{x} = \begin{bmatrix}\hat{x}_S & 0\end{bmatrix}^T$ and $\hat{z} = \begin{bmatrix}\hat{z}_S & \hat{z}_{S^c}\end{bmatrix}^T$, where $\hat{z}_{S^c}$ is to be determined so that $\hat{z} \in \partial\|\hat{x}\|_1$. We thus plug $\hat{x}$ and $\hat{z}$ into equation (2.4), and get

$$B^T B\hat{x} - B^T EBx^* + \lambda\hat{z} = 0, \tag{2.17}$$

where we use the assumption that $y = Bx^*$. Let I be the $N \times N$ identity matrix. Then (2.17) can be rewritten as

$$B^T B(\hat{x} - x^*) + B^T(I - E)Bx^* + \lambda\hat{z} = 0,$$

which can also be written as

$$\begin{bmatrix}B_S^T \\ B_{S^c}^T\end{bmatrix}\begin{bmatrix}B_S & B_{S^c}\end{bmatrix}\begin{bmatrix}\hat{x}_S - x_S^* \\ 0\end{bmatrix} + \begin{bmatrix}B_S^T \\ B_{S^c}^T\end{bmatrix}(I - E)\begin{bmatrix}B_S & B_{S^c}\end{bmatrix}\begin{bmatrix}x_S^* \\ 0\end{bmatrix} + \lambda\begin{bmatrix}\hat{z}_S \\ \hat{z}_{S^c}\end{bmatrix} = 0,$$

where we use the fact that $x_{S^c}^* = 0$. We have from the top block that

$$B_S^T B_S(\hat{x}_S - x_S^*) + B_S^T(I - E)B_S x_S^* + \lambda\hat{z}_S = 0,$$

which indicates

$$\hat{x}_S - x_S^* = -(B_S^T B_S)^{-1}[B_S^T(I - E)B_S x_S^* + \lambda\hat{z}_S]. \tag{2.18}$$

On the other hand, we have from the bottom block that

$$B_{S^c}^T B_S(\hat{x}_S - x_S^*) + B_{S^c}^T(I - E)B_S x_S^* + \lambda\hat{z}_{S^c} = 0. \tag{2.19}$$

By plugging $\hat{x}_S - x_S^*$ from (2.18) to (2.19), since $B_S^T B_S$ is invertible and $\lambda > 0$, we have solved $\hat{z}_{S^c}$ and get

$$\hat{z}_{S^c} = B_{S^c}^T[B_S(B_S^T B_S)^{-1}\hat{z}_S - \frac{1}{\lambda}(B_S(B_S^T B_S)^{-1}B_S^T - I)(E - I)B_S x_S^*].$$

We need to show that $\hat{z}$ is a subgradient of the l^1 norm at $\hat{x}$. Note that $\|\hat{z}_S\|_\infty \leq 1$. Thus, by a direct bound, we have

$$\|\hat{z}_{S^c}\|_\infty \leq \left\|B_{S^c}^T B_S(B_S^T B_S)^{-1}\right\|_\infty + \frac{1}{\lambda}\left\|B_{S^c}^T(I - B_S(B_S^T B_S)^{-1}B_S^T)\right\|_\infty \|E - I\|_\infty\|y\|_\infty$$

$$< \frac{n_S^2 M_{S,S^c}}{K} + \frac{1}{\lambda} M^1_{S,y} \frac{\lambda}{M^1_{S,y}} (1 - \frac{n_S^2 M_{S,S^c}}{K}) \quad \text{(by Lemma 2)}$$

$$< 1.$$

Hence $\hat{z}$ is a subgradient of the l^1 norm at $\hat{x}$ and $\hat{x}$ is a solution to (2.10), and any solution x to (2.10) satisfies $x_i = 0$, if $i \in S^c$; that is, $x = \begin{bmatrix} x_S & 0 \end{bmatrix}^T$ where x_S is a solution to program (2.16). Therefore, $\hat{x}$ is the unique solution to (2.10) since $\hat{x}_S$ is the unique solution to (2.16).

For the second part, we have from (2.18),

$$\begin{aligned} \left\|\hat{x} - x^*\right\|_\infty = \left\|\hat{x}_S - x^*_S\right\|_\infty &\leq \left\|(B_S^T B_S)^{-1} B_S^T\right\|_\infty \|E - I\|_\infty \|y\|_\infty + \lambda \left\|(B_S^T B_S)^{-1}\right\|_\infty \\ &\leq \max_i |e_i - 1| \cdot M^2_{S,y} + \lambda \left\|(B_S^T B_S)^{-1}\right\|_\infty \end{aligned}$$

Therefore, if for some period p_i, there exists a coefficient $|x^*_{p_i}(j)| > \max_i |e_i - 1| \cdot M^2_{S,y} + \lambda \left\|(B_S^T B_S)^{-1}\right\|_\infty$, then $EOP_{\hat{x}}(p_i) > 0$. □

Next, we show the robustness of (2.10) to jitter; that is, when the periods between two consecutive cycles are not fixed and deviated by some perturbation. For example, a p-periodic signal with peaks at $p, 2p, 3p, \ldots$ is jittered (or its peak locations are perturbed) so that the peaks arise at $p + \epsilon_1, 2p + \epsilon_2, 3p + \epsilon_3, \ldots$, where ϵ_i is bounded and $|\epsilon_i| < p/2$.

Theorem 2 (Robustness to jitter)**.** *Suppose N is sufficiently large such that $K > n_S^2 M_{S,S^c}$, and $\tilde{y} = \sum_{i=1}^{l} V_i y_i$, where $y_i = \sum_{j=0}^{\phi(p_i)-1} b^{(j)}_{p_i,N} x^*_{p_i}(j+1)$, and V_i is a diagonal block matrix:*

$$V_i = \begin{bmatrix} V_{i,1} & & & \\ & V_{i,2} & & \\ & & \ddots & \\ & & & V_{i,k_i} \end{bmatrix},$$

where each $V_{i,j}$ is either a identity matrix or a permutation matrix. Then, if

$$\lambda > \frac{2K \sum_{i=1}^{l} M^1_{S,y_i}}{K - n_S^2 M_{S,S^c}}, \tag{2.20}$$

the program (2.10) has a unique solution $\hat{x}$ such that if $\hat{x}_i \neq 0$, then $i \in SOP(x^*)$. Moreover, if for $i = 1, 2, \ldots, l$ we denote

$$\beta_i = \max_j |x^*_{p_i}(j)|, \tag{2.21}$$

then the solution $\hat{x}$ can successfully identify periods p_i if β_i satisfies

$$\beta_i > \sum_{i=1}^{l} 2M^2_{S,y_i} + \lambda \left\| (B_S^T B_S)^{-1} \right\|_\infty . \tag{2.22}$$

Proof. First we note that $\|V_i - I\|_\infty \leq 2$ for any i. We can write each y_i as $y_i = Bx^*_{S_i} = B_{S_i} x^*_{S_i}$, where S_i are indices in B that correspond to $\mathcal{R}_{p_i,N}$ so that $S = \bigcup_{i=1}^{l} S_i$. We follow the same procedure an notations as in the proof of previous theorem to obtain

$$\begin{bmatrix} B_S^T \\ B_{S^c}^T \end{bmatrix} \begin{bmatrix} B_S & B_{S^c} \end{bmatrix} \begin{bmatrix} \hat{x}_S - x^*_S \\ 0 \end{bmatrix} + \sum_{i=1}^{l} \begin{bmatrix} B_S^T \\ B_{S^c}^T \end{bmatrix} (I - V_i) \begin{bmatrix} B_{S_i} & B_{S_i^c} \end{bmatrix} \begin{bmatrix} x^*_{S_i} \\ 0 \end{bmatrix} + \lambda \begin{bmatrix} \hat{z}_S \\ \hat{z}_{S^c} \end{bmatrix} = 0.$$

We have from the top block that

$$B_S^T B_S (\hat{x}_S - x^*_S) + \sum_{i=1}^{l} B_S^T (I - V_i) B_{S_i} x^*_{S_i} + \lambda \hat{z}_S = 0,$$

which indicates

$$\hat{x}_S - x^*_S = -(B_S^T B_S)^{-1} [\sum_{i=1}^{l} B_S^T (I - V_i) B_{S_i} x^*_{S_i} + \lambda \hat{z}_S]. \tag{2.23}$$

On the other hand, we have from the bottom block that

$$B_{S^c}^T B_S (\hat{x}_S - x^*_S) + \sum_{i=1}^{l} B_{S^c}^T (I - V_i) B_{S_i} x^*_{S_i} + \lambda \hat{z}_{S^c} = 0. \tag{2.24}$$

By plugging $\hat{x}_S - x^*_S$ from (2.23) to (2.24), we get

$$\hat{z}_{S^c} = B_{S^c}^T [B_S (B_S^T B_S)^{-1} \hat{z}_S + \sum_{i=1}^{l} \frac{1}{\lambda} (B_S (B_S^T B_S)^{-1} B_S^T - I)(I - V_i) B_{S_i} x^*_{S_i}].$$

Thus, by a direct bound, we have

$$\begin{aligned} \|\hat{z}_{S^c}\|_\infty &\leq \left\| B_{S^c}^T B_S (B_S^T B_S)^{-1} \right\|_\infty + \sum_{i=1}^{l} \frac{1}{\lambda} \left\| B_{S^c}^T (I - B_S (B_S^T B_S)^{-1} B_S^T) \right\|_\infty \|I - V_i\|_\infty \|y_i\|_\infty \\ &< \frac{n_S^2 M_{S,S^c}}{K} + 2 \sum_{i=1}^{l} M^1_{S,y_i} \frac{K - n_S^2 M_{S,S^c}}{2K \sum_{i=1}^{l} M^1_{S,y_i}} \end{aligned}$$

$= 1.$

On the other hand, we have from (2.23)

$$\begin{aligned}\left\|\hat{x} - x^*\right\|_\infty = \left\|\hat{x}_S - x^*_S\right\|_\infty &\leq \sum_{i=1}^{l} \left\|(B_S^T B_S)^{-1} B_S^T\right\|_\infty \|V_i - I\|_\infty \|y_i\|_\infty + \lambda \left\|(B_S^T B_S)^{-1}\right\|_\infty \\ &\leq \sum_{i=1}^{l} 2M^2_{S,y_i} + \lambda \left\|(B_S^T B_S)^{-1}\right\|_\infty .\end{aligned}$$

□

Theorem 3 (Robustness to additive noise)**.** *Suppose N is sufficiently large such that $K > n_S^2 M_{S,S^c}$ and $\tilde{y} = y + e$, where the entries of e are i.i.d. Gaussian with mean 0 and variance σ^2, i.e. $e \sim \mathcal{N}(0, \sigma^2 I)$. Let*

$$C := \max_{1 \leq i \leq \Phi(P_{max})} \|b_i\|_2^2 . \tag{2.25}$$

Denote

$$\beta_i = \max_j |x^*_{p_i}(j)| \tag{2.26}$$

for $i = 1, 2, \ldots, l$. Then, with probability at least

$$1 - (\Phi(P_{max}) - n_S) e^{-\frac{\lambda^2 (K - n_S^2 M_{S,S^c})^2}{2C\sigma^2 K^2}}, \tag{2.27}$$

we have the following:

a) the program (2.10) has a unique solution $\hat{x}$ such that if $\hat{x}_i \neq 0$, then $i \in SOP(x^*)$.

b) the solution $\hat{x}$ can successfully identify the period p_i if β_i satisfies

$$\beta_i > \sqrt{\frac{\lambda^2 (K - n_S^2 M_{S,S^c})^2}{K^4} + \frac{2C\sigma^2 (\log n_S - \log(\Phi(P_{max}) - n_S))}{K^2}} + \lambda \left\|(B_S^T B_S)^{-1}\right\|_\infty . \tag{2.28}$$

Before we prove the theorem, we mention that if we choose $\lambda = \Omega(\sqrt{N})$, then the above probability tends to 1 as $N \to \infty$ since $K = \Theta(N)$ and $C = \Theta(N)$. Moreover, with the choice of $\lambda = \Omega(\sqrt{N})$, the right-hand side of (2.28) will be $\Omega(1/\sqrt{N})$. The proof below is similar to the proof of [70, Theorem 1].

Proof. First we note that for any i, $1 \le i \le N$ and $t > 0$ we have

$$\begin{aligned}\mathbb{P}(|e_i| \ge t) &= \frac{2}{\sqrt{2\pi}\sigma}\int_t^\infty e^{-\frac{x^2}{2\sigma^2}}\,\mathrm{d}x = \frac{2}{\sqrt{2\pi}\sigma}\int_0^\infty e^{-\frac{(x+t)^2}{2\sigma^2}}\,\mathrm{d}x \\ &\le \frac{2}{\sqrt{2\pi}\sigma}e^{-\frac{t^2}{2\sigma^2}}\int_0^\infty e^{-\frac{x^2}{2\sigma^2}}\,\mathrm{d}x = e^{-\frac{t^2}{2\sigma^2}}.\end{aligned}$$

As at the beginning of the proof of Theorem 1, we have from (2.4) that

$$B^TB\hat{x} - B^T(Bx^* + e) + \lambda\hat{z} = 0,$$

so that

$$B^TB(\hat{x} - x^*) - B^Te + \lambda\hat{z} = 0.$$

Consequently,

$$\begin{bmatrix} B_S^T \\ B_{S^c}^T \end{bmatrix}\begin{bmatrix} B_S & B_{S^c} \end{bmatrix}\begin{bmatrix} \hat{x}_S - x_S^* \\ 0 \end{bmatrix} - \begin{bmatrix} B_S^T \\ B_{S^c}^T \end{bmatrix} e + \lambda\begin{bmatrix} \hat{z}_S \\ \hat{z}_{S^c} \end{bmatrix} = 0.$$

For the first part of the theorem, it is sufficient to prove $\|\hat{z}_{S^c}\|_\infty < 1$.

We have from the top block that

$$B_S^TB_S(\hat{x}_S - x_S^*) - B_S^Te + \lambda\hat{z}_S = 0,$$

which indicates

$$\hat{x}_S - x_S^* = (B_S^TB_S)^{-1}(B_S^Te - \lambda\hat{z}_S). \tag{2.29}$$

On the other hand, we have from the bottom block that

$$B_{S^c}^TB_S(\hat{x}_S - x_S^*) - B_{S^c}^Te + \lambda\hat{z}_{S^c} = 0.$$

Substitute $\hat{x}_S - x_S^*$ to have

$$\hat{z}_{S^c} = B_{S^c}^TB_S(B_S^TB_S)^{-1}\hat{z}_S + \frac{1}{\lambda}B_{S^c}^T(I - B_S(B_S^TB_S)^{-1}B_S^T)e. \tag{2.30}$$

Note that each entry of $\frac{1}{\lambda}B_{S^c}^T(I - B_S(B_S^TB_S)^{-1}B_S^T)e$ has mean zero and variance at most $\frac{C\sigma^2}{\lambda^2}$, since $I - B_S(B_S^TB_S)^{-1}B_S^T$ is an orthogonal projection an thus has spectral norm equal to 1. Therefore, by a direct union bound we have

$$\mathbb{P}\left(\left\|\frac{1}{\lambda}B_{S^c}^T(I - B_S(B_S^TB_S)^{-1}B_S^T)e\right\|_\infty \ge t\right) \le (\Phi(P_{max}) - n_S)e^{-\frac{\lambda^2t^2}{2C\sigma^2}}, \tag{2.31}$$

since there are $\Phi(P_{max}) - n_S$ entries in $\frac{1}{\lambda} B_{S^c}^T (I - B_S (B_S^T B_S)^{-1} B_S^T) e$. Let $t = 1 - \frac{n_S^2 M_{S,S^c}}{K}$, and we have

$$\mathbb{P}\left(\left\| \frac{1}{\lambda} B_{S^c}^T (I - B_S (B_S^T B_S)^{-1} B_S^T) e \right\|_\infty \geq 1 - \frac{n_S^2 M_{S,S^c}}{K} \right) \leq (\Phi(P_{max}) - n_S) e^{-\frac{\lambda^2 (K - n_S^2 M_{S,S^c})^2}{2C\sigma^2 K^2}},$$

so that with probability at least $1 - (\Phi(P_{max}) - n_S) e^{-\frac{\lambda^2 (K - n_S^2 M_{S,S^c})^2}{2C\sigma^2 K^2}}$, we have

$$\begin{aligned} \|\hat{z}_{S^c}\|_\infty &\leq \left\| B_{S^c}^T B_S (B_S^T B_S)^{-1} \right\|_\infty + \left\| \frac{1}{\lambda} B_{S^c}^T (I - B_S (B_S^T B_S)^{-1} B_S^T) e \right\|_\infty \\ &< \frac{n_S^2 M_{S,S^c}}{K} + 1 - \frac{n_S^2 M_{S,S^c}}{K} \\ &= 1. \end{aligned}$$

To prove the second part of the theorem, we first note that by Lemma 2, each entry of $(B_S^T B_S)^{-1} B_S^T e$ has mean zero and variance at most $\frac{C\sigma^2}{K^2}$. Therefore, by a direct union bound we have

$$\mathbb{P}\Big(\left\| (B_S^T B_S)^{-1} B_S^T e \right\|_\infty > t \Big) \leq n_S e^{-\frac{K^2 t^2}{2C\sigma^2}}. \tag{2.32}$$

Let

$$t = \sqrt{\frac{\lambda^2 (K - n_S^2 M_{S,S^c})^2}{K^4} + \frac{2C\sigma^2 (\log n_S - \log(\Phi(P_{max}) - n_S))}{K^2}},$$

then with probability at least $1 - (\Phi(P_{max}) - n_S) e^{-\frac{\lambda^2 (K - n_S^2 M_{S,S^c})^2}{2C\sigma^2 K^2}}$, we have

$$\begin{aligned} &\left\| \hat{x} - x^* \right\|_\infty = \left\| \hat{x}_S - x_S^* \right\|_\infty \\ &\leq \left\| (B_S^T B_S)^{-1} B_S^T e \right\|_\infty + \lambda \left\| (B_S^T B_S)^{-1} \right\|_\infty \\ &\leq \sqrt{\frac{\lambda^2 (K - n_S^2 M_{S,S^c})^2}{K^4} + \frac{2C\sigma^2 (\log n_S - \log(\Phi(P_{max}) - n_S))}{K^2}} + \lambda \left\| (B_S^T B_S)^{-1} \right\|_\infty. \end{aligned}$$

□

2.6 Conclusion

We have proposed a novel TF analysis algorithm, RDS, which incorporates the RPT and l^1 penalized linear regression, to analyze complicated time series with non-sinusoidal oscillatory patterns. Numerical experiments demonstrate its usefulness in the extraction of the fundamental IF of a non-stationary signal. It alleviates some limitations of the traditional cepstrum-based de-shape algorithm, and it is supported by the provided robustness analysis of RPT to different perturbations. Specifically, the l^1 approach helps stabilize the impact of inevitable noise; the robustness of the RPT to the spectral envelop fluctuation helps reduce the inevitable low quefrency artifact issue when we apply the STCT; the fact that the PT preserves the oscillatory component energy helps resolve the "weak fundamental component" issue. In addition to these benefits, the computational complexity of this algorithm is reasonably fast, and can be easily scaled to long time series.

We have a comment here regarding directly applying the PT to the high frequency time series, particularly the biomedical signals. In general, any oscillatory component in a biomedical signal does not oscillate with a fixed period. Instead, its period changes from time to time. Since the PT is a global method, directly applying the PT to extract periods from such time series might not be suitable. Note that this does not contradict the provided robustness property of RPT against jitter shown in Theorem 2. This is because the time-varying period cannot be well approximated by the jitter effect.

It is natural to ask if we can generalize the PT to short periods, and come out with the idea of "short-time PT"; that is, we run the PT over a short period around the time we want to study how fast it oscillates, and stitch all PT together and generate a two-dimensional matrix that we can call the *time-period representation*. See Figure 2.11 for a preliminary result of this idea when we apply it to the ta-mECG $\mathbf{f}$ shown in Figure 2.1, where $\mathbf{f}(i) = f(i\Delta_t)$, f is the ta-mECG, $\Delta_t = 1/250$ second, and $i = 1, \ldots, N$. Numerically, for the i-th sampling time, $[\mathbf{f}(i-500)\ \mathbf{f}(i-499)\ \mathbf{f}(i-500)\ldots\mathbf{f}(i)\ldots\mathbf{f}(i+499)\ \mathbf{f}(i+500)]$; that is, the window is chosen to be of 4 seconds long. Then, based on the knowledge of the maternal IHR, we choose $P_{max} = 200$, which is associated with $250/200 = 1.25$Hz.

After tuning parameters (although not optimized via a grid search), the final "time-period representation" results with different periodicity penalization functions are shown in Figure 2.11. It is clear that we can see some useful information, both for the maternal and fetal IHR, but the quality is clearly less ideal compared with the proposed RDS. We mention that we can choose other window lengths, like 10 seconds long, but the results are worse and we do not show them. Even worse, note that the period change might happen suddenly in few cycles; for example, when a subject has an arrhythmia attack. The short-time PT idea will be further impacted. A potential solution is applying a change point detection algorithm to segment the signal into pieces, and then apply the PT. We do not claim that the short-time PT does not work, since we have not extensively explore this possibility. This is the direction we would explore in our future work.

Another comment following the about discussion about the short-time PT, the RDS solution we propose can be viewed as a solution sitting between PT and short-time PT in the following sense. We first delegate the time-varying oscillatory periods information to the TF domain, where the oscillation is related to the spectrum of the non-sinusoidal oscillation, and this oscillation in the TF domain is more regular and can be well modeled by the jitter effect. Then, we can benefit from this nice periodicity property in the TF domain and apply the PT to extract the fundamental IF, and hence the instantaneous period.

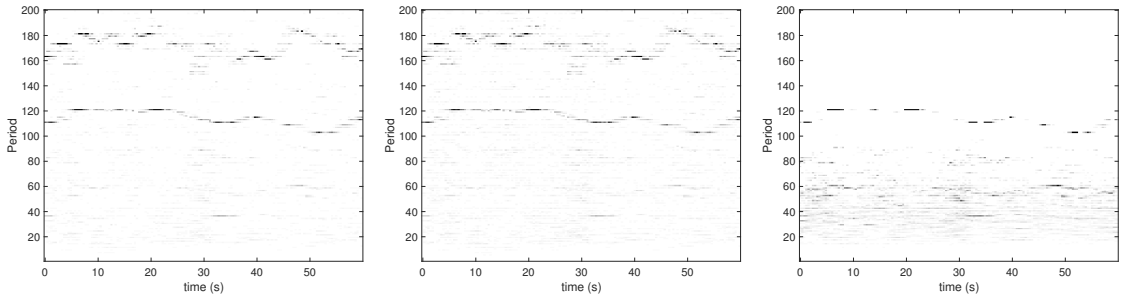

Figure 2.11: Left: $\zeta(p) = 1$ with $\lambda = 500$. Middle: $\zeta(p) = p$ with $\lambda = 200$. Right: $\zeta(p) = p^2$ with $\lambda = 10$.

There are several future directions we will explore. From the theoretical perspective, we need to establish the statistical property of the RPT, and hence the RDS, so that we can carry out statistical inference. To the best of our knowledge, there is limited work in this direction, even for the basic PT. Note that the statistical property of de-shape algorithm is also missing. Although we do not discuss extensively in the main article, we shall indicate the boundary problem, which is universal to all kernel-based algorithms. Around the boundary, the STFT would get distorted, and hence the RDS. How to handle this boundary effect is important and will be studied in the future work, particularly for the real-time implementation of the RDS. Although our theoretical results and preliminary numerical results support that the RDS resolves several limitations of the traditional de-shape approach, it is not clear how useful it is to real data. We will explore its performance in the real database and clinical problems in future work.

Chapter 3

Rotations in the time-frequency plane

In the preceding chapter, we introduced techniques that make it possible to determine more accurately the $\varphi'(t)$ for signals of the form $f(t) = \sum_{l=1}^{L} A_l(t)s_l(\varphi_l(t))$, where each s_l is 1-periodic. The key was to exploit periodicity features in the TF-plane, at fixed time, to determine the fundamental frequency of each component. In this chapter, we will also encounter the different harmonic components in the TF-plane of $s_l(\varphi_l(t))$, but in a different form.

The time-frequency algorithms introduced and applied in this chapter address the problem of the "thickened" representation in the TF-plane of chirping components when on uses the SST or ConceFT.

In this chapter we use a slightly different definition of the STFT. It will be convenient to omit the factor 2π in the complex exponential in the STFT. We define two types of Gaussian windows centered at (t, ξ) in the time-frequency plane, differing only in their phase:

$$g_{t,\xi}(x) = \pi^{-\frac{1}{4}} e^{-\frac{1}{2}(x-t)^2 + i\xi(x-t)}, \text{ (standard coherent states)},$$

and

$$\tilde{g}_{t,\xi}(x) = \pi^{-\frac{1}{4}} e^{-\frac{1}{2}(x-t)^2 + i\xi x - \frac{i}{2}t\xi}, \text{ (cononical coherent states)}.$$

We define the modified short-time Fourier transform (STFT) of a function $f \in L^2(\mathbb{R})$ with a window function $g(x) = \pi^{-\frac{1}{4}} e^{-\frac{1}{2}x^2}$ as

$$V_f^{(g)}(t, \xi) = \langle f, g_{t,\xi} \rangle = \pi^{-\frac{1}{4}} \int f(x) e^{-\frac{1}{2}(x-t)^2 + i\xi(x-t)} \, \mathrm{d}x.$$

Thus the reassignment rule in the SST becomes

$$\omega_f^{(g)}(t, \xi) = \Re \frac{\partial_t V_f^{(g)}(t, \xi)}{i V_f^{(g)}(t, \xi)},$$

where $\Re$ indicates the real part of a complex number.

3.1 Motivation: Problems when chirping

We showed earlier that the SST gives good results for functions of the form $f(t) = A(t)\cos(2\pi\varphi(t))$ when $\left|A'(t)\right|$ and $\left|\varphi''(t)\right|$ are small compared with $\left|\varphi'(t)\right|$. Some signals of interest have a "chirping" behavior, i.e. $\varphi'(t)$ increases (or decreases) monotonically on some time interval, during which $\left|\varphi''(t)\right|$ is not negligibly small. In this case, the signal no longer satisfies the conditions under which it was proved that the SST recovers $\varphi'(t)$ accurately. In practice, this leads to a "thickening" of the IF curve in the SST and the ConceFT, that was already mentioned in the Introduction (see Figure 1.6). In the next section we will investigate this in more detail, and propose tools that will help to construct a remedy.

3.2 Mathematical background

Let us first introduce some operators to build our analysis and algorithmic tools that will be useful. We denote the rotation of a point (t, ξ) by an angle θ with respect to the origin in the TF plane by

$$R_\theta(t, \xi) = (t \cos\theta - \xi \sin\theta, t \sin\theta + \xi \cos\theta).$$

By the resolution of the indentity, for any $f \in L^2(\mathbb{R})$, we have in L^2 sense

$$f = \frac{1}{2\pi} \iint \langle f, \tilde{g}_{t,\xi} \rangle \tilde{g}_{t,\xi}(x) \, \mathrm{d}t \, \mathrm{d}\xi. \tag{3.1}$$

We then define rotations of the TF representation of f by an angle θ in terms of the origin as

$$U_\theta f(x) = \frac{1}{2\pi} \iint \langle f, \tilde{g}_{t,\xi} \rangle \tilde{g}_{R_\theta(t,\xi)}(x) \, \mathrm{d}t \, \mathrm{d}\xi.$$

We also define the operation of translating the TF content of f by (t, ξ) as

$$(w(t, \xi)f)(x) = e^{-\frac{it\xi}{2}} e^{i\xi x} f(x - t),$$

so $\tilde{g}_{t,\xi} = w(t, \xi)g$. Then we have

Proposition 5. $w(t, \xi)w(t', \xi') = e^{\frac{i}{2}(t'\xi - t\xi')} w(t + t', \xi + \xi')$.

Proof.

$$\begin{aligned}
[w(t, \xi)w(t', \xi')f](x) &= [w(t', \xi')f](x - t) e^{i\xi x} e^{-\frac{i}{2}t\xi} \\
&= f(x - (t + t')) e^{i\xi'(x-t)} e^{-\frac{i}{2}t'\xi'} e^{i\xi x} e^{-\frac{i}{2}t\xi} \\
&= f(x - (t + t')) e^{i(\xi+\xi')x} e^{-\frac{i}{2}(t+t')(\xi+\xi')} e^{\frac{i}{2}(t'\xi - t\xi')} \\
&= e^{\frac{i}{2}(t'\xi - t\xi')} [w(t + t', \xi + \xi')f](x).
\end{aligned}$$

□

The following identity will be used extensively:

$$\langle \tilde{g}_{t,\xi}, \tilde{g}_{t',\xi'} \rangle = \pi^{-\frac{1}{2}} \int e^{-\frac{1}{2}(x-t)^2 - \frac{1}{2}(x-t')^2 + i(\xi - \xi')x - \frac{i}{2}t\xi + \frac{i}{2}t'\xi'} \, \mathrm{d}x$$

$$= \pi^{-\frac{1}{2}} \int e^{-(x-\frac{t+t'}{2})^2 - \frac{1}{4}(t-t')^2 + i(\xi-\xi')(x-\frac{t+t'}{2}) + i\frac{(\xi-\xi')(t+t')}{2} - \frac{it\xi}{2} + \frac{it'\xi'}{2}} \, \mathrm{d}x$$
$$= e^{-\frac{(t-t')^2}{4} - \frac{(\xi-\xi')^2}{4} + \frac{i(t'\xi - t\xi')}{2}}. \qquad (*)$$

Proposition 6. $U_\theta \tilde{g}_{t,\xi}(x) = \tilde{g}_{R_\theta(t,\xi)}(x)$.

Proof. First, by (*), we have

$$\begin{aligned}
&\langle \tilde{g}_{t,\xi}, \tilde{g}_{R_\alpha(t',\xi')} \rangle \\
&= \exp(-\frac{(t - (t'\cos\alpha - \xi'\sin\alpha))^2}{4} - \frac{(\xi - (t'\sin\alpha + \xi'\cos\alpha))^2}{4} \\
&\qquad + \frac{i(\xi(t'\cos\alpha - \xi'\sin\alpha) - t(t'\sin\alpha + \xi'\cos\alpha))}{2}) \\
&= \exp[-\frac{1}{4}t^2 - \frac{1}{4}(t'\cos\alpha - \xi'\sin\alpha)^2 + \frac{1}{2}(tt'\cos\alpha - t\xi'\sin\alpha) - \frac{1}{4}\xi^2 - \frac{1}{4}(t'\sin\alpha + \xi'\cos\alpha)^2 \\
&\qquad + \frac{1}{2}(t'\xi\sin\alpha + \xi\xi'\cos\alpha) + \frac{i}{2}(t'\xi\cos\alpha - \xi\xi'\sin\alpha - tt'\sin\alpha - t\xi'\cos\alpha)] \\
&= \exp[-\frac{1}{4}(t^2 + t'^2 + \xi^2 + \xi'^2) + \frac{1}{2}tt'e^{-i\alpha} + \frac{1}{2}\xi\xi'e^{-i\alpha} + \frac{i}{2}t'\xi e^{-i\alpha} - \frac{i}{2}t\xi'e^{-i\alpha}] \\
&= \exp[-\frac{1}{4}(t^2 + t'^2 + \xi^2 + \xi'^2) + \frac{1}{2}(\xi - it)(\xi' + it')e^{-i\alpha}].
\end{aligned}$$

Then it is easy to check that

$$\overline{\langle \tilde{g}_{t',\xi'}, \tilde{g}_{R_{-\alpha}(t,\xi)} \rangle} = \langle \tilde{g}_{t,\xi}, \tilde{g}_{R_\alpha(t',\xi')} \rangle,$$

and we have thus

$$\langle \tilde{g}_{R_{-\alpha}(t,\xi)}, \tilde{g}_{t',\xi'} \rangle = \overline{\langle \tilde{g}_{t',\xi'}, \tilde{g}_{R_{-\alpha}(t,\xi)} \rangle} = \langle \tilde{g}_{t,\xi}, \tilde{g}_{R_\alpha(t',\xi')} \rangle.$$

Consequently,

$$\begin{aligned}
\langle U_\theta \tilde{g}_{t,\xi}, \tilde{g}_{t',\xi'} \rangle &= \iint \langle \tilde{g}_{t,\xi}, \tilde{g}_{t'',\xi''} \rangle \langle \tilde{g}_{R_\theta(t'',\xi'')}, \tilde{g}_{t',\xi'} \rangle \frac{\mathrm{d}t'' \, \mathrm{d}\xi''}{2\pi} \\
&= \iint \langle \tilde{g}_{t,\xi}, \tilde{g}_{R_{-\theta}(t^*,\xi^*)} \rangle \langle \tilde{g}_{t^*,\xi^*}, \tilde{g}_{t',\xi'} \rangle \frac{\mathrm{d}t^* \, \mathrm{d}\xi^*}{2\pi} \\
&= \iint \langle \tilde{g}_{R_\theta(t,\xi)}, \tilde{g}_{t^*,\xi^*} \rangle \langle \tilde{g}_{t^*,\xi^*}, \tilde{g}_{t',\xi'} \rangle \frac{\mathrm{d}t^* \, \mathrm{d}\xi^*}{2\pi} \\
&= \langle \tilde{g}_{R_\theta(t,\xi)}, \tilde{g}_{t',\xi'} \rangle,
\end{aligned}$$

where the second equality follows from a change of variables: $(t^*, \xi^*) = R_\theta(t'', \xi'')$. Therefore, $U_\theta \tilde{g}_{t,\xi} = \tilde{g}_{R_\theta(t,\xi)}$. □

Proposition 7. *$U_\theta w(t,\xi) = w(R_\theta(t,\xi))U_\theta$.*

Proof.

$$\begin{aligned} U_\theta w(t,\xi)\tilde{g}_{t',\xi'} &= U_\theta w(t,\xi)w(t',\xi')\tilde{g} \\ &= e^{\frac{i}{2}(t'\xi - t\xi')} U_\theta w(t+t',\xi+\xi')\tilde{g} \\ &= e^{\frac{i}{2}(t'\xi - t\xi')} \tilde{g}_{R_\theta(t+t',\xi+\xi')} \\ &= e^{\frac{i}{2}[t,\xi]J[t',\xi']^\mathsf{T} - \frac{i}{2}[t,\xi]O_\theta^\mathsf{T} J O_\theta [t',\xi']^\mathsf{T}} w(R_\theta(t,\xi))U_\theta \tilde{g}_{t',\xi'} \\ &= w(R_\theta(t,\xi))U_\theta \tilde{g}_{t',\xi'}, \end{aligned}$$

where

$$J = \begin{bmatrix} 0 & -1 \\ 1 & 0 \end{bmatrix},$$

and

$$O_\theta = \begin{bmatrix} \cos\theta & -\sin\theta \\ \sin\theta & \cos\theta \end{bmatrix}.$$

□

Proposition 8. *U_θ is unitary.*

Proof. For any $h \in L^2$, we have

$$\begin{aligned} \langle U_\theta f, h\rangle &= \iint \langle f, \tilde{g}_{t,\xi}\rangle\langle \tilde{g}_{R_\theta(t,\xi)}, h\rangle \frac{\mathrm{d}t\,\mathrm{d}\xi}{2\pi} \\ &= \iint \langle f, \tilde{g}_{R_{-\theta}(t',\xi')}\rangle\langle \tilde{g}_{t',\xi'}, h\rangle \frac{\mathrm{d}t'\,\mathrm{d}\xi'}{2\pi} \\ &= \overline{\langle U_{-\theta}h, f\rangle} \\ &= \langle f, U_{-\theta}h\rangle. \end{aligned}$$

So $U_\theta^* = U_{-\theta}$. Moreover, we have

$$U_\alpha U_\beta \tilde{g}_{t,\xi} = U_\alpha \tilde{g}_{R_\beta(t,\xi)} = \tilde{g}_{R_\alpha R_\beta(t,\xi)} = U_{\alpha+\beta}\tilde{g}_{t,\xi},$$

so $U_\alpha U_\beta = U_{\alpha+\beta}$. Therefore, we have

$$U_\theta U_\theta^* = U_\theta U_{-\theta} = Id = U_{-\theta}U_\theta = U_\theta^* U_\theta.$$

□

The operators U_θ, $\theta \in [0, 2\pi]$ thus provide a natural unitary representation of the operation of rotating in the TF-plane the TF "content" of a function f. Some of their properties were studied in [13]. In particular, their eigenvectors are the Hermite functions: $U_\theta H_n = e^{in\theta} H_n$, where $H_n(x)$ is the n-th order Hermite function based on $g(x) = \pi^{-\frac{1}{4}} e^{-\frac{x^2}{2}}$, i.e. $H_n = N_n(x - \frac{\mathrm{d}}{\mathrm{d}x})^n g$, where N_n is a normalization factor.

Let us now investigate the phenomena of thickening in SST and splitting in ConceFT when chirping. To understand what happens with a simple chirp that we construct explicitly, let $G_\gamma(x) = \pi^{-\frac{1}{4}} \gamma^{-\frac{1}{4}} e^{-\frac{x^2}{2\gamma}}$; G_γ is normalized to have unit L^2 norm. To obtain a chirp, we can rotate G_γ by applying U_θ and take $\gamma \to \infty$. See Figure 3.1 for an example of the constructed signal when $\gamma = 100$ and $\theta = \frac{\pi}{3}$.

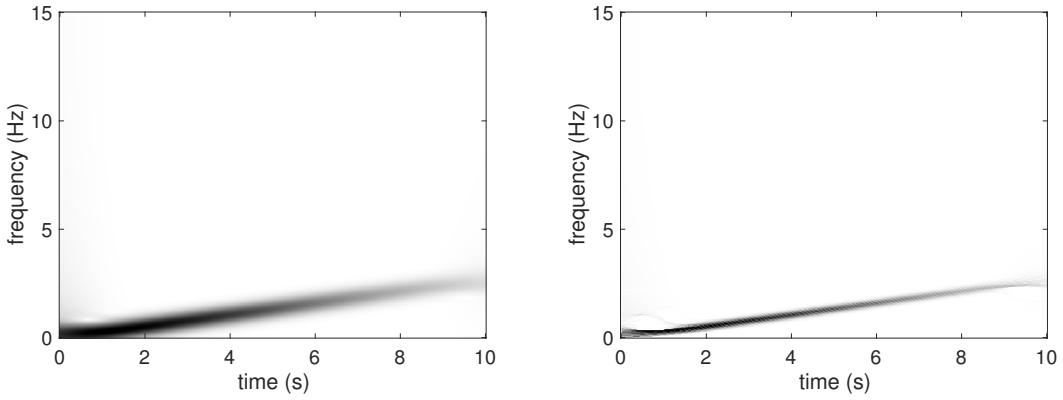

Figure 3.1: Left: the STFT of $U_{\frac{\pi}{3}} G_{100}$; right: the SST of $U_{\frac{\pi}{3}} G_{100}$. Here we use a Gaussian window.

Let us compute the SST of $U_\theta G_\gamma$. It will be useful to know that

$$\begin{aligned}
\langle G_\gamma, \tilde{g}_{t,\xi} \rangle &= \pi^{-\frac{1}{2}} \gamma^{-\frac{1}{4}} \int e^{-\frac{1}{2\gamma}x^2 - \frac{1}{2}(x-t)^2 - i\xi x + \frac{i}{2}t\xi} \, \mathrm{d}x \\
&= \pi^{-\frac{1}{2}} \gamma^{-\frac{1}{4}} \int e^{-\frac{\gamma+1}{2\gamma}(x - \frac{\gamma t}{\gamma+1})^2 - \frac{1}{2}t^2 + \frac{\gamma}{2(\gamma+1)}t^2 - i\xi(x - \frac{\gamma t}{\gamma+1}) - i\xi\frac{\gamma t}{\gamma+1} + \frac{i}{2}t\xi} \, \mathrm{d}x \\
&= 2^{\frac{1}{2}} \gamma^{\frac{1}{4}} (\gamma+1)^{-\frac{1}{2}} e^{-\frac{\gamma}{2(\gamma+1)}\xi^2 - \frac{1}{2(\gamma+1)}t^2 - \frac{i(\gamma-1)}{2(\gamma+1)}t\xi}.
\end{aligned}$$

It follows that

$$\begin{aligned}&\langle U_\theta G_\gamma, \tilde{g}_{t,\xi}\rangle = \langle G_\gamma, \tilde{g}_{R_{-\theta}(t,\xi)}\rangle \\ &= 2^{\frac{1}{2}}\gamma^{\frac{1}{4}}(\gamma+1)^{-\frac{1}{2}}e^{-\frac{\gamma}{2(\gamma+1)}(-t\sin\theta+\xi\cos\theta)^2-\frac{1}{2(\gamma+1)}(t\cos\theta+\xi\sin\theta)^2-\frac{i(\gamma-1)}{2(\gamma+1)}(t\cos\theta+\xi\sin\theta)(-t\sin\theta+\xi\cos\theta)}.\end{aligned}$$

To see where the linear chirp $\lim_{\gamma\to\infty} G_\gamma$ is concentrated in the TF-plane, we take the module of $\langle U_\theta G_\gamma, \tilde{g}_{t,\xi}\rangle$:

$$2^{-\frac{1}{2}}\gamma^{-\frac{1}{4}}(\gamma+1)^{\frac{1}{2}}\left|\langle U_\theta G_\gamma, \tilde{g}_{t,\xi}\rangle\right| = e^{-\frac{\gamma}{2(\gamma+1)}(-t\sin\theta+\xi\cos\theta)^2-\frac{1}{2(\gamma+1)}(t\cos\theta+\xi\sin\theta)^2},$$

and the right-hand side tends to $e^{-\frac{1}{2}(-t\sin\theta+\xi\cos\theta)^2}$. Note that $(-t\sin\theta+\xi\cos\theta)^2$ is the square of the distance from (t,ξ) to the line $L_\theta : \xi = t\tan\theta$ in TF-plane, thus the TF content of $\lim_{\gamma\to\infty} G_\gamma$ is indeed concentrated around the line L_θ. In addition, the phase of $\langle U_\theta G_\gamma, \tilde{g}_{t,\xi}\rangle$ is

$$\begin{aligned}\frac{\langle U_\theta G_\gamma, \tilde{g}_{t,\xi}\rangle}{\left|\langle U_\theta G_\gamma, \tilde{g}_{t,\xi}\rangle\right|} &= e^{-\frac{i(\gamma-1)}{2(\gamma+1)}(t\cos\theta+\xi\sin\theta)(-t\sin\theta+\xi\cos\theta)} \\ &= e^{-\frac{i(\gamma-1)}{2(\gamma+1)}(t\xi\cos 2\theta+\frac{\xi^2-t^2}{2}\sin 2\theta)}.\end{aligned}$$

Next we look at the SST of the constructed chirp. Note that

$$\begin{aligned}\langle U_\theta G_\gamma, g_{t,\xi}\rangle &= e^{\frac{i}{2}t\xi}\langle U_\theta G_\gamma, \tilde{g}_{t,\xi}\rangle \\ &= 2^{\frac{1}{2}}\gamma^{\frac{1}{4}}(\gamma+1)^{-\frac{1}{2}}e^{-\frac{\gamma}{2(\gamma+1)}(-t\sin\theta+\xi\cos\theta)^2-\frac{1}{2(\gamma+1)}(t\cos\theta+\xi\sin\theta)^2-\frac{i(\gamma-1)}{2(\gamma+1)}(t\xi\cos 2\theta+\frac{\xi^2-t^2}{2}\sin 2\theta)+\frac{i}{2}t\xi}.\end{aligned}$$

Hence

$$\begin{aligned}&-i\frac{\partial_t\langle U_\theta G_\gamma, g_{t,\xi}\rangle}{\langle U_\theta G_\gamma, g_{t,\xi}\rangle} \\ &= -i(-\frac{\gamma}{\alpha+1}(-t\sin\theta+\xi\cos\theta)(-\sin\theta)-\frac{1}{\gamma+1}(t\cos\theta+\xi\sin\theta)\cos\theta-\frac{i(\gamma-1)}{2(\gamma+1)}(\xi\cos 2\theta-t\sin 2\theta) \\ &\quad+\frac{i}{2}\xi)\end{aligned}$$

Taking the real part, we have

$$\begin{aligned}\omega^{(g)}_{U_\theta G_\gamma}(t,\xi) &= \Re(-i\frac{\partial_t\langle U_\theta G_\gamma, g_{t,\xi}\rangle}{\langle U_\theta G_\gamma, g_{t,\xi}\rangle}) \\ &= -\frac{(\gamma-1)}{2(\gamma+1)}(\xi\cos 2\theta-t\sin 2\theta)+\frac{1}{2}\xi\end{aligned}$$

$$= \frac{1}{2}\xi(1-\cos 2\theta) + \frac{1}{2}t\sin 2\theta + \frac{1}{\gamma+1}(\xi\cos 2\theta - t\sin 2\theta)$$
$$= \xi\sin^2\theta + t\sin\theta\cos\theta + \frac{1}{\gamma+1}(\xi\cos 2\theta - t\sin 2\theta).$$

We would like to get $\xi_1(t) = t\tan\theta$ for the vertical SST of the linear chirp, so the actual SST of the chirp can be rewritten as

$$\omega^{(g)}_{U_\theta G_\gamma}(t,\xi) = \xi\sin^2\theta + \xi_1(t)\cos^2\theta + \frac{1}{\gamma+1}(\xi\cos 2\theta - t\sin 2\theta),$$

which tends to $\xi\sin^2\theta + \xi_1(t)\cos^2\theta$ as $\gamma\to\infty$. In fact, $\xi\sin^2\theta + \xi_1(t)\cos^2\theta$ is the ξ-coordinate of the projection onto L_θ of the point (t,ξ), so the SST $\omega^{(g)}_{U_\theta G_\gamma}(t,\xi)$ is a weighted average of ξ and $\xi_1(t)$ that takes ξ into account more as θ differs more from 0; in the limit for large γ and for θ not too large, we have $\omega^{(g)}_{U_\theta G_\gamma}(t,\xi) \approx \xi_1(t) + \theta^2(\xi - \xi_1(t)) + O(\theta^4)$. The standard SST approach would thus, on chirps like these, produce a "thickened" line, as a result of this ξ-dependent shift in $\omega^{(g)}_{U_\theta G_\gamma}(t,\xi)$.

Because ConceFT is built on the SST, ConceFT transforms of chirps likewise show artifacts. In a ConceFT transform, an "average effect" is computed by many SSTs using different windows. Most of these windows will have several peaks in the frequency domain. For this reason, we also investigate what happens to SSTs for window functions h that have multiple peaks (e,g, higher order Hermite functions), For instance, let us consider the following window that we can easily make out of standard coherent states that imitates the Hermite function $xe^{-\frac{x^2}{2}}$ in that its Fourier transform has two peaks:

$$h_b(x) = \pi^{-\frac{1}{4}}(e^{-\frac{(x-b)^2}{2}} - e^{-\frac{(x+b)^2}{2}}).$$

We have $h_b = g_{b,0} - g_{-b,0}$, and can easily write down the inner product of $U_\theta G_\alpha$ with $h_{b;t,\xi}(x) := h_b(x-t)e^{i\xi(x-t)}$. Since $h_b(x-t)e^{i\xi(x-t)} = \pi^{-\frac{1}{4}}e^{i\xi(x-t)}(e^{-\frac{(x-b-t)^2}{2}} - e^{-\frac{(x+b-t)^2}{2}}) = e^{i\xi b}g_{t+b,\xi} - e^{-i\xi b}g_{t-b,\xi}$. It follows that

$$\langle U_\theta G_\alpha, h_{b;t,\xi}\rangle = e^{-i\xi b}\langle U_\theta G_\alpha, g_{t+b,\xi}\rangle - e^{i\xi b}\langle U_\theta G_\alpha, g_{t-b,\xi}\rangle.$$

Under the assumption that in the region where $\big|\langle U_\theta G_\alpha, g_{t+b,\xi}\rangle\big|$ is large, the value of $\big|\langle U_\theta G_\alpha, g_{t-b,\xi}\rangle\big|$ is very small (i.e. if b is not too small), we can use the approximation

$$\big|\langle U_\theta G_\alpha, h_{b;t,\xi}\rangle\big| = \max(\big|\langle U_\theta G_\alpha, g_{t+b,\xi}\rangle\big|, \big|\langle U_\theta G_\alpha, g_{t-b,\xi}\rangle\big|).$$

And we then get

$$\Re(-i\frac{\partial_t\langle U_\theta G_\alpha, h_{b;t,\xi}\rangle}{\langle U_\theta G_\alpha, h_{b;t,\xi}\rangle}) \approx \xi\sin^2\theta + \begin{cases}(t+b)\sin\theta\cos\theta, & \text{if } \left|\langle U_\theta G_\alpha, g_{t+b,\xi}\rangle\right| \text{ dominates,}\\ (t-b)\sin\theta\cos\theta, & \text{if } \left|\langle U_\theta G_\alpha, g_{t-b,\xi}\rangle\right| \text{ dominates.}\end{cases}$$

See Figure 3.2 for an example, where we use the window function $h_1(x) = \pi^{-\frac{1}{4}}(e^{-\frac{(x-1)^2}{2}} - e^{-\frac{(x+1)^2}{2}})$. We do observe the splitting, into two lines, one slightly above, the other slightly below the "thickened" line.

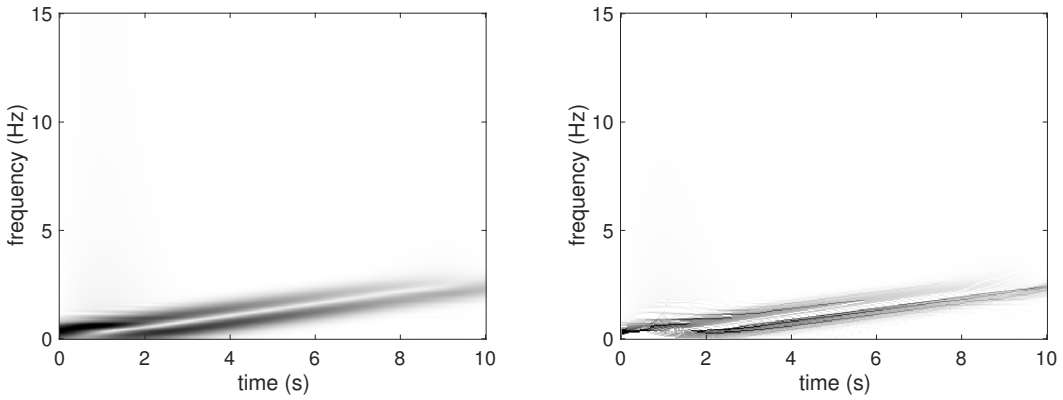

Figure 3.2: Left: the STFT of $U_{\frac{\pi}{3}}G_{100}$; right: the SST of $U_{\frac{\pi}{3}}G_{100}$, with window function: $h_1(x)$.

Remark 2. *The vertical distance between the two "split" lines is* $2b\sin\theta\cos\theta$. *The "thickening" we observed for the Gaussian window, measured vertically, was* $\omega^{(g)}_{U_\theta G_\alpha}(t,\xi) - \xi_1(t) = (\xi - \xi_1(t))\sin^2\theta$, *where we consider only* ξ *close to* $\xi_1(t)$ *since these are the only ones for which* $\left|\langle U_\theta G_\alpha, g_{t,\xi}\rangle\right|$ *is non-negligible. To compare the two effects, we can consider that* $\xi - \xi_1(t)$ *of the same size as* b *in the* $h_{b;t,\xi}$. *Therefore, the splitting is linear in* $\sin\theta$, *whereas the thickening we see in the SST is proportional to* $\sin^2\theta$, *and thus less pronounced.*

3.3 Theoretical results

Based on the analysis above, we want to correct the SST of a signal where the IF changes rapidly. More precisely, we shall do this by rotating the TF content of a signal where the derivative of the IF is large. As a result the "thickening" and "splitting" would be alleviated as the "slope" of the IF becomes small. Because the behavior of the IF of a component of f need not be the same for all time, we want to carry out this operation locally in time. In addition, f may have several components (in different frequency ranges) with different chirping behavior in the same time interval, which means we should also isolate in frequency the portion of f that we wish to rotate. For this purpose, we will utilize the localization operator P_R in TF-plane introduced in [13], which will permits to localize on a TF disk around (t, ξ). We shall also consider localization on ellipses centered at (t, ξ) for greater flexibility and extra properties that will turn out to be essential.

Let us briefly review this operator first. Given a point (t, ξ) in TF-plane, we can always localize and move the TF content of a signal f near (t, ξ) as follows. Define $\tilde{H}_{n;,t,\xi}(x) := w(t, \xi)H_n(x)$. One can use the $\tilde{H}_n$ to easily define localization operators,

Definition 12 ([13]). *The TF localization operator $\mathbf{P}_R$ on the disk S_R centered at origin of radius R is defined as*

$$\mathbf{P}_R f = \frac{1}{2\pi} \iint\limits_{t^2+\xi^2 \leq R^2} \langle f, \tilde{g}_{t,\xi} \rangle \tilde{g}_{t,\xi} \, \mathrm{d}t \, \mathrm{d}\xi.$$

Note that this is consistent with the notion that the rank-one projection operator $\langle \cdot, \tilde{g}_{t,\xi} \rangle \tilde{g}_{t,\xi}$ captures the TF-content of a signal near TF-point (t, ξ); from (3.1) we obtain that the $\mathbf{P}_R$ tends strongly to Id when $R \to \infty$. From section 4 of [13], we know that each $\mathbf{P}_R$ commutes with the rotation operator U_θ, which has the H_n as eigenvectors: $U_\theta H_n = e^{in\theta} H_n$. It follows that H_n are also the eigenvectors for $\mathbf{P}_R$:

$$\mathbf{P}_R = \sum_{n=0}^{\infty} \lambda_n(R) \langle \cdot, H_n \rangle H_n,$$

where

$$\lambda_n(R) = \frac{1}{2\pi} \iint\limits_{t^2+\xi^2 \leq R^2} \left| \langle H_n, \tilde{g}_{t,\xi} \rangle \right|^2 \mathrm{d}t \, \mathrm{d}\xi$$

$$= \frac{1}{n!}\int_0^{R^2/2} t^n e^{-t}\,\mathrm{d}t.$$

The behavior of $\lambda_n(R)$ as a funtion of n and R can also be found in section 2.8 of [14]. The following lemma gives an upper bound on the decay of the magnitude of the TF content outside of the disk:

Lemma 3 (in section 3 of [13]). *Suppose $f \in L^2(\mathbb{R})$, for any $\epsilon \in (0,1)$, we have*

$$\left|\langle \mathbf{P}_R f, g_{t,\xi}\rangle\right| \le \epsilon^{-\frac{1}{2}}\|f\|_2 \exp[-\frac{1-\epsilon}{4}\mathrm{dist}((t,\xi), S_R)^2].$$

Replacing S_R by its complement S_R^c in the proof of the above lemma, we have an error bound of the STFT of the localized signal compared with that of the original signal.

Corollary 2. $\left|\langle \mathbf{P}_R f, g_{t,\xi}\rangle - \langle f, g_{t,\xi}\rangle\right| \le \epsilon^{-\frac{1}{2}}\|f\|_2 \exp[-\frac{1-\epsilon}{4}\mathrm{dist}((t,\xi), S_R^c)^2]$.

If we would like to localize on a disk around (t,ξ) instead of around the origin, then we would use

$$\mathbf{P}_{R;t,\xi} := w(t,\xi)\mathbf{P}_R w(t,\xi)^* = \sum_n \lambda_n(R)\langle \cdot, \tilde{H}_{n;t,\xi}\rangle \tilde{H}_{n;t,\xi}.$$

Rotating the content of this disk in TF plane by angle $-\theta$ would then be easy as well; the composite operator would be

$$L_{R;\theta,t,\xi} f := w(t,\xi)U_{-\theta}\mathbf{P}_R w(t,\xi)^* f = \sum_n e^{-in\theta}\lambda_n(R)\langle f, \tilde{H}_{n;t,\xi}\rangle \tilde{H}_{n;t,\xi}.$$

This expansion of the operator is useful to compute the transform numerically. We want to rotate on the TF content of a signal, i.e. we hope the center of the disk to be on the IF of a signal. However, this is not possible because of the "thickening" when the IF changes rapidly. To avoid determining the center of the disk before applying the transform, we propose a way to "rotate along the whole frequency range". One can generalize all the above to build the localization operators (see section 5 of [13]) that single out ellipses rather than disks.

The extra freedom of choosing how excentric this ellipse can be will turn out to be important in what follows. First we introduce the dilation operator B_α for $\alpha > 0$,

$$(B_\alpha f)(x) = \sqrt{\alpha} f(\alpha x).$$

We also define

$$g_{t,\xi}^{(\alpha)}(x) = e^{i\xi(x-t)}(B_\alpha g)(x-t),$$

and

$$\tilde{g}_{t,\xi}^{(\alpha)}(x) = w(t,\xi)B_\alpha g.$$

Then we can define

Definition 13 ([13]). *The TF localization operator $\mathbf{P}_R^\alpha$ on the ellipse*

$$S_{\alpha,R} = \left\{(t,\xi) \in \mathbb{R}^2 : \alpha^2 t^2 + \alpha^{-2}\xi^2 \le R^2\right\}$$

is defined as

$$\mathbf{P}_R^\alpha f = \frac{1}{2\pi} \iint\limits_{(t,\xi)\in S_{\alpha,R}} \langle f, \tilde{g}_{t,\xi}^{(\alpha)}\rangle \tilde{g}_{t,\xi}^{(\alpha)}\, \mathrm{d}t\, \mathrm{d}\xi.$$

It is shown in [13] that $B_\alpha^{-1}\mathbf{P}_R^\alpha B_\alpha = \mathbf{P}_R$, hence the eigenvalues of $\mathbf{P}_R^\alpha$ are the same as those of $\mathbf{P}_R$, and the eigenfunctions of $\mathbf{P}_R^\alpha$ are dilated Hermite functions,

$$H_n^{(\alpha)}(x) := (B_\alpha H_n)(x) = \sqrt{\alpha} H_n(\alpha x).$$

Moreover, parallel to (*), we have

$$\langle \tilde{g}_{t,\xi}^{(\alpha)}, \tilde{g}_{t',\xi'}^{(\alpha)}\rangle = e^{-\frac{\alpha^2(t-t')^2}{4} - \frac{(\xi-\xi')^2}{4\alpha^2} + \frac{i(t'\xi - t\xi')}{2}}.$$

As a result, we have a lemma for $\mathbf{P}_R^\alpha$, whose proof is similar to that of Lemma 3:

Lemma 4. *Suppose $f \in L^2(\mathbb{R})$, for any $\epsilon \in (0,1)$, we have*

$$\left|\langle \mathbf{P}_R^\alpha f, \tilde{g}_{t,\xi}^{(\alpha)}\rangle\right| \le \epsilon^{-\frac{1}{2}} \|f\|_2 \exp[-\frac{1-\epsilon}{4} \inf_{(t',\xi')\in S_{\alpha,R}} (\frac{(\xi-\xi')^2}{\alpha^2} + \alpha^2(t-t')^2)];$$

as well as its corollary

Corollary 3. *Suppose $f \in L^2(\mathbb{R})$, for any $\epsilon \in (0,1)$, we have*

$$\left|\langle \mathbf{P}_R^\alpha f, \tilde{g}_{t,\xi}^{(\alpha)}\rangle - \langle f, \tilde{g}_{t,\xi}^{(\alpha)}\rangle\right| \le \epsilon^{-\frac{1}{2}} \|f\|_2 \exp[-\frac{1-\epsilon}{4} \inf_{(t',\xi')\in S_{\alpha,R}^c} (\frac{(\xi-\xi')^2}{\alpha^2} + \alpha^2(t-t')^2)].$$

We also define

$$\tilde{H}^{(\alpha)}_{n;t,\xi}(x) := w(t,\xi)H^{(\alpha)}_n(x).$$

as well as the rotation operator that works with $\tilde{g}^{(\alpha)}_{t,\xi}(x)$,

$$U^\alpha_\theta = B_\alpha U_\theta B^{-1}_\alpha,$$

and

$$R^\alpha_\theta(t,\xi) = (t\cos\theta - \frac{\xi}{\alpha^2}\sin\theta, \alpha^2 t\sin\theta + \xi\cos\theta).$$

It is straightforward to see that

$$U^\alpha_\theta H^{(\alpha)}_n = B_\alpha U_\theta B^{-1}_\alpha B_\alpha H_n = B_\alpha(e^{in\theta}H_n) = e^{in\theta}H^{(\alpha)}_n.$$

Therefore, if we would like to localize on an ellipse of dilation factor α around (t,ξ) instead of around the origin, then we would use

$$\mathbf{P}^\alpha_{R;t,\xi} := w(t,\xi)\mathbf{P}^\alpha_R w(t,\xi)^* = \sum_n \lambda_n(R)\langle\cdot, \tilde{H}^{(\alpha)}_{n;t,\xi}\rangle\tilde{H}^{(\alpha)}_{n;t,\xi}.$$

Rotating the content of this ellipse in TF plane by angle $-\theta$ (with respect to the elliptic coordinates) gives rise to the composite operator

$$L^\alpha_{R;\theta,t,\xi}f := w(t,\xi)U^\alpha_{-\theta}\mathbf{P}^\alpha_R w(t,\xi)^* f = \sum_n e^{-in\theta}\lambda_n(R)\langle f, \tilde{H}^{(\alpha)}_{n;t,\xi}\rangle\tilde{H}^{(\alpha)}_{n;t,\xi}.$$

We have several results about the dilated rotation operators U^α_θ

Proposition 9. $U^\alpha_\theta\tilde{g}^{(\alpha)}_{t,\xi}(x) = \tilde{g}^{(\alpha)}_{R^\alpha_\theta(t,\xi)}(x)$.

Proof.

$$\begin{aligned}
U^\alpha_\theta\tilde{g}^{(\alpha)}_{t,\xi}(x) &= B_\alpha U_\theta B^{-1}_\alpha(\pi^{-\frac{1}{4}}\sqrt{\alpha}e^{-\frac{\alpha^2(x-t)^2}{2}+i\xi x-\frac{i}{2}t\xi}) \\
&= B_\alpha U_\theta(\pi^{-\frac{1}{4}}e^{-\frac{\alpha^2(\frac{x}{\alpha}-t)^2}{2}+i\frac{\xi}{\alpha}x-\frac{i}{2}t\xi}) \\
&= B_\alpha U_\theta\tilde{g}_{\alpha t,\frac{\xi}{\alpha}} \\
&= B_\alpha\tilde{g}_{R_\theta(\alpha t,\frac{\xi}{\alpha})} \\
&= B_\alpha(\pi^{-\frac{1}{4}}e^{-\frac{(x-\alpha t\cos\theta+\frac{\xi}{\alpha}\sin\theta)^2}{2}+i(\alpha t\sin\theta+\frac{\xi}{\alpha}\cos\theta)x-\frac{i}{2}(\alpha t\cos\theta-\frac{\xi}{\alpha}\sin\theta)(\alpha t\sin\theta+\frac{\xi}{\alpha}\cos\theta)})
\end{aligned}$$

$$= \pi^{-\frac{1}{4}}\sqrt{\alpha}e^{-\frac{\alpha^2(x-t\cos\theta+\frac{\xi}{\alpha^2}\sin\theta)^2}{2}+i(\alpha^2 t\sin\theta+\xi\cos\theta)x-\frac{i}{2}(t\cos\theta-\frac{\xi}{\alpha^2}\sin\theta)(\alpha^2 t\sin\theta+\xi\cos\theta)}$$

$$= \tilde{g}^{(\alpha)}_{R^\alpha_\theta(t,\xi)}.$$

□

Proposition 10. $U^\alpha_\theta w(t,\xi) = w(R^\alpha_\theta(t,\xi))U^\alpha_\theta$.

Proof.

$$U^\alpha_\theta w(t,\xi)\tilde{g}^{(\alpha)}_{t',\xi'}$$
$$= e^{\frac{i}{2}(t'\xi-t\xi')}U^\alpha_\theta w(t+t',\xi+\xi')B_\alpha g$$
$$= e^{\frac{i}{2}(t'\xi-t\xi')}U^\alpha_\theta \tilde{g}^{(\alpha)}_{t+t',\xi+\xi'}$$
$$= e^{\frac{i}{2}(t'\xi-t\xi')}\tilde{g}^{(\alpha)}_{R^\alpha_\theta(t+t',\xi+\xi')}$$
$$= e^{\frac{i}{2}(t'\xi-t\xi')}w(R^\alpha_\theta(t+t',\xi+\xi'))B_\alpha g$$
$$= e^{\frac{i}{2}(t'\xi-t\xi')}e^{-\frac{i}{2}((t'\cos\theta-\frac{\xi'}{\alpha^2}\sin\theta)(\alpha^2 t\sin\theta+\xi\cos\theta)-(t\cos\theta-\frac{\xi}{\alpha^2}\sin\theta)(\alpha^2 t'\sin\theta+\xi'\cos\theta))}w(R^\alpha_\theta(t,\xi))w(R^\alpha_\theta(t',\xi'))B_\alpha g$$
$$= w(R^\alpha_\theta(t,\xi))w(R^\alpha_\theta(t',\xi'))B_\alpha g$$
$$= w(R^\alpha_\theta(t,\xi))U^\alpha_\theta \tilde{g}^{(\alpha)}_{t',\xi'}$$

□

Proposition 11. *U^α_θ is unitary.*

Proof. Note that $\langle B_\alpha f, g\rangle = \langle f, B_{\frac{1}{\alpha}}g\rangle$, so $B^*_\alpha = B_{\frac{1}{\alpha}} = B^{-1}_\alpha$. Then we have

$$U^\alpha_\theta U^{\alpha *}_\theta = B_\alpha U_\theta B^{-1}_\alpha B_\alpha U_{-\theta}B^{-1}_\alpha = Id = U^{\alpha *}_\theta U^\alpha_\theta$$

□

Lemma 5.

$$\langle U^\alpha_\theta G_\gamma, \tilde{g}^{(\alpha)}_{t,\xi}\rangle = \gamma^{\frac{1}{4}}\sqrt{\frac{2}{1+\alpha^2\gamma}}e^{-\frac{\gamma(\xi\cos\theta-\alpha^2 t\sin\theta)^2}{2(1+\alpha^2\gamma)}-\frac{\alpha^2(\frac{\xi}{\alpha^2}\sin\theta+t\cos\theta)^2}{2(1+\alpha^2\gamma)}-\frac{i(\alpha^2\gamma-1)}{2(1+\alpha^2\gamma)}(\xi\cos\theta-\alpha^2 t\sin\theta)(\frac{\xi}{\alpha^2}\sin\theta+t\cos\theta)}$$

Proof. Let us first compute

$$\langle G_\gamma, \tilde{g}^{(\alpha)}_{t,\xi}\rangle = \pi^{-\frac{1}{2}}\gamma^{-\frac{1}{4}}\int e^{-\frac{x^2}{2\gamma}-\frac{\alpha^2(x-t)^2}{2}-i\xi x+\frac{i}{2}t\xi}\,\mathrm{d}x$$

$$= \pi^{-\frac{1}{2}}\gamma^{-\frac{1}{4}} \int e^{-\frac{1+\alpha^2\gamma}{2\gamma}(x-\frac{\gamma\alpha^2 t}{1+\alpha^2\gamma})^2 - i\xi(x-\frac{\gamma\alpha^2 t}{1+\alpha^2\gamma}) - \frac{\alpha^2 t^2}{2} + \frac{\gamma\alpha^4 t^2}{2(1+\alpha^2\gamma)} - i\xi\frac{\gamma\alpha^2 t}{1+\alpha^2\gamma} + \frac{i}{2}t\xi}\,\mathrm{d}x$$

$$= \gamma^{-\frac{1}{4}}\Big(\frac{2\gamma}{1+\alpha^2\gamma}\Big)^{\frac{1}{2}} e^{-\frac{\gamma\xi^2}{2(1+\alpha^2\gamma)} - \frac{\alpha^2 t^2}{2} + \frac{\gamma\alpha^4 t^2}{2(1+\alpha^2\gamma)} - i\xi\frac{\gamma\alpha^2 t}{1+\alpha^2\gamma} + \frac{i}{2}t\xi}$$

$$= \gamma^{\frac{1}{4}}\Big(\frac{2}{1+\alpha^2\gamma}\Big)^{\frac{1}{2}} e^{-\frac{\gamma\xi^2}{2(1+\alpha^2\gamma)} - \frac{\alpha^2 t^2}{2(1+\alpha^2\gamma)} - \frac{i(\alpha^2\gamma-1)}{2(1+\alpha^2\gamma)}t\xi}.$$

Then

$$\begin{aligned}
\langle U_\theta^\alpha G_\gamma, \tilde{g}_{t,\xi}^{(\alpha)}\rangle &= \langle G_\gamma, U_{-\theta}^\alpha \tilde{g}_{t,\xi}^{(\alpha)}\rangle \\
&= \langle G_\gamma, \tilde{g}^{(\alpha)}_{R_{-\theta}^\alpha(t,\xi)}\rangle \\
&= \gamma^{\frac{1}{4}}\sqrt{\frac{2}{1+\alpha^2\gamma}}\, e^{-\frac{\gamma(\xi\cos\theta-\alpha^2 t\sin\theta)^2}{2(1+\alpha^2\gamma)} - \frac{\alpha^2(\frac{\xi}{\alpha^2}\sin\theta+t\cos\theta)^2}{2(1+\alpha^2\gamma)} - \frac{i(\alpha^2\gamma-1)}{2(1+\alpha^2\gamma)}(\xi\cos\theta-\alpha^2 t\sin\theta)(\frac{\xi}{\alpha^2}\sin\theta+t\cos\theta)}.
\end{aligned}$$

□

Taking $\gamma\to\infty$, we have

$$\lim_{\gamma\to\infty}\gamma^{-\frac{1}{4}}\sqrt{\frac{1+\alpha^2\gamma}{2}}\langle U_\theta^\alpha G_\gamma, \tilde{g}_{t,\xi}^{(\alpha)}\rangle = e^{-\frac{(\xi\cos\theta-\alpha^2 t\sin\theta)^2}{2\alpha^2} - \frac{i}{2}(t\xi\cos 2\theta + \frac{\sin 2\theta}{2}(\frac{\xi^2}{\alpha^2}-\alpha^2 t^2))},$$

so the TF content of $\lim_{\gamma\to\infty}\gamma^{-\frac{1}{4}}\sqrt{\frac{1+\alpha^2\gamma}{2}}U_\theta^\alpha G_\gamma$ is concentrated at the line

$$L_\theta^\alpha : \xi\cos\theta - \alpha^2 t\sin\theta = 0,$$

whose slope is $\alpha^2\tan\theta$. That is, $U_\theta^\alpha G_\gamma$ constructs a linear chirp (in distribution sense) which passes through the origin and the IF of which has slope $\alpha^2\tan\theta$.

We saw earlier that, when γ is large $U_{\theta_0}^\alpha G_\gamma$ is a "narrow" chirp centered around $(0,0)$ in the TF-plane, with slope $\alpha^2\tan\theta_0$. To move its center to $(t_0, \alpha^2 t_0\tan\theta_0)$, we apply the appropriate w-operation:

$$f_{t_0,\theta_0,\alpha,\gamma} := w(t_0, \alpha^2 t_0\tan\theta_0)U_{\theta_0}^\alpha G_\gamma. \tag{3.2}$$

We now use these "skewed" rotation operators U_θ^α as follows to define

$$T_{\alpha,t_0,\theta}f(x) = \int w(t_0,\xi)U_{-\theta}^\alpha w(t_0,\xi)^* f(x)\,\mathrm{d}\xi. \tag{3.3}$$

We construct the $U_{-\theta}^\alpha$ as rotations in the TF-plane after a dilation that, in some sense, readjusts units in time and frequency in a consistent way. Sandwiching these $U_{-\theta}^\alpha$ between

$w(t_0,\xi)$ and $w(t_0,\xi)^*$ turns this in a rotation around (t_0,ξ). In practice, we want to perform our TF-rotation on a signal component for which we do not know a priori where it is located in frequency. By integrating over ξ in (3.3) we build an operator that will have the effect of rotating the TF content of our chirping component, wherever it is located frequency-wise. The following proposition details the effect of $T_{\alpha,t_0,\theta}$ on a chirp.

Proposition 12. *Suppose f is a linear chirp defined by (3.2), and let*

$$C_1(\alpha,\theta_0,\theta)=\frac{(\cos\theta_0-\cos(\theta_0-\theta))^2}{2\alpha^2}+\frac{i}{2}(\frac{\sin\theta}{\alpha^2}+\frac{\sin 2\theta_0}{2\alpha^2}-\frac{\sin(2\theta_0-\theta)}{\alpha^2}+\frac{\sin(2\theta_0-2\theta)}{2\alpha^2}),$$

$$\begin{aligned}C_2(\alpha,\theta_0,\theta)=&\frac{2\alpha^2\sin(\theta_0-\theta)}{\cos\theta_0-\cos(\theta_0-\theta)}(\frac{\sin\theta}{\alpha^2}+\frac{\sin 2\theta_0}{2\alpha^2}-\frac{\sin(2\theta_0-\theta)}{\alpha^2}+\frac{\sin(2\theta_0-2\theta)}{2\alpha^2})\\&+\cos(2\theta_0-\theta)-1-\cos(2\theta_0-2\theta)+\cos\theta,\end{aligned}$$

and

$$\begin{aligned}C_3(\alpha,\theta_0,\theta)=&\frac{2\cos(\theta_0-\theta)}{\cos\theta_0-\cos(\theta_0-\theta)}(\frac{\sin\theta}{\alpha^2}+\frac{\sin 2\theta_0}{2\alpha^2}-\frac{\sin(2\theta_0-\theta)}{\alpha^2}+\frac{\sin(2\theta_0-2\theta)}{2\alpha^2})\\&-\frac{\sin(2\theta_0-\theta)}{\alpha^2}+\frac{\sin(2\theta_0-2\theta)}{\alpha^2}+\frac{\sin\theta}{\alpha^2},\end{aligned}$$

then

$$\lim_{\gamma\to\infty}\gamma^{-\frac{1}{4}}\sqrt{\frac{1+\alpha^2\gamma}{2}}\langle T_{\alpha,t_0,\theta}f,\tilde{g}^{(\alpha)}_{t',\xi'}\rangle=\sqrt{\frac{\pi}{C_1(\alpha,\theta_0,\theta)}}e^{-\frac{[C_2(\alpha,\theta_0,\theta)(t'-t_0)-C_3(\alpha,\theta_0,\theta)(\xi'-\alpha^2t_0\tan\theta_0)]^2}{16C_1(\alpha,\theta_0,\theta)}}\cdot C_4(\alpha,\theta_0,\theta),$$

where

$$\begin{aligned}C_4(\alpha,\theta_0,\theta)=&\,e^{-\frac{i}{2}[\alpha^2t_0(t_0-t')\tan\theta_0\cos\theta-\alpha^2t_0^2\tan\theta_0+\xi't_0+\xi't_0\tan\theta_0\sin\theta]}\\&\cdot e^{-\frac{i}{2}[\frac{1}{2}\alpha^2t_0^2\tan^2\theta_0\sin 2\theta_0-\xi't_0\tan\theta_0\sin(2\theta_0-\theta)-\alpha^2t_0\tan\theta_0(t'-t_0)\cos(2\theta_0-\theta)+\frac{\sin(2\theta_0-2\theta)}{2\alpha^2}\xi'^2]}\\&\cdot e^{-\frac{i}{2}[\xi'(t'-t_0)\cos(2\theta_0-2\theta)-\frac{\alpha^2\sin(2\theta_0-2\theta)}{2}(t'-t_0)^2]}\\&\cdot e^{-\frac{i}{2}(\frac{\sin\theta}{\alpha^2}+\frac{\sin 2\theta_0}{2\alpha^2}-\frac{\sin(2\theta_0-\theta)}{\alpha^2}+\frac{\sin(2\theta_0-2\theta)}{2\alpha^2})(\frac{\xi'\cos(\theta_0-\theta)-\alpha^2t_0\sin\theta_0-(t'-t_0)\alpha^2\sin(\theta_0-\theta)}{\cos\theta_0-\cos(\theta_0-\theta)})^2}\\&\cdot e^{\frac{i}{2}[(-t_0\sin 2\theta_0\tan\theta_0+\frac{\xi'\sin(2\theta_0-\theta)}{\alpha^2}+t_0\tan\theta_0\sin(2\theta_0-\theta)+(t'-t_0)\cos(2\theta_0-\theta)-\frac{\xi'\sin(2\theta_0-2\theta)}{\alpha^2})\frac{\xi'\cos(\theta_0-\theta)-\alpha^2t_0\sin\theta_0-(t'-t_0)\alpha^2\sin(\theta_0-\theta}{\cos\theta_0-\cos(\theta_0-\theta)}}\\&\cdot e^{\frac{i}{2}[(-(t'-t_0)\cos(2\theta_0-2\theta)+t_0-t_0\cos\theta-t_0\tan\theta_0\sin\theta+t'\cos\theta-t'-\frac{\xi'\sin\theta}{\alpha^2})\frac{\xi'\cos(\theta_0-\theta)-\alpha^2t_0\sin\theta_0-(t'-t_0)\alpha^2\sin(\theta_0-\theta)}{\cos\theta_0-\cos(\theta_0-\theta)}]},\end{aligned}$$

and $\sqrt{\frac{\pi}{C_1(\alpha,\theta_0,\theta)}}$ is defined as the branch in the first or fourth quadrant in the complex plane.

Proof. Let $C(\gamma,\alpha)=\gamma^{-\frac{1}{4}}\sqrt{\frac{1+\alpha^2\gamma}{2}}$, then

$$\lim_{\gamma\to\infty} C(\gamma,\alpha)\langle w(t_0,\xi)U^\alpha_{-\theta}w(t_0,\xi)^* f,\tilde{g}^{(\alpha)}_{t',\xi'}\rangle$$

$$= \lim_{\gamma\to\infty} C(\gamma,\alpha)\langle w(t_0,\xi)U^\alpha_{-\theta}w(t_0,\xi)^* w(t_0,\alpha^2 t_0\tan\theta_0)U^\alpha_{\theta_0}G_\gamma,\tilde{g}^{(\alpha)}_{t',\xi'}\rangle$$

$$= \lim_{\gamma\to\infty} C(\gamma,\alpha)\langle U^\alpha_{-\theta}w(t_0,\xi)^* w(t_0,\alpha^2 t_0\tan\theta_0)U^\alpha_{\theta_0}G_\gamma, w(t_0,\xi)^*\tilde{g}^{(\alpha)}_{t',\xi'}\rangle$$

$$= e^{\frac{i}{2}(-t_0\xi+\alpha^2 t_0^2\tan\theta_0)}\lim_{\gamma\to\infty} C(\gamma,\alpha)\langle U^\alpha_{-\theta}w(0,\alpha^2 t_0\tan\theta_0-\xi)U^\alpha_{\theta_0}G_\gamma, w(t_0,\xi)^*\tilde{g}^{(\alpha)}_{t',\xi'}\rangle$$

$$= e^{\frac{i}{2}(-t_0\xi+\alpha^2 t_0^2\tan\theta_0)}\lim_{\gamma\to\infty} C(\gamma,\alpha)\langle w(R^\alpha_{-\theta}(0,\alpha^2 t_0\tan\theta_0-\xi))U^\alpha_{\theta_0-\theta}G_\gamma, w(t_0,\xi)^*\tilde{g}^{(\alpha)}_{t',\xi'}\rangle$$

$$= e^{\frac{i}{2}(-t_0\xi+\alpha^2 t_0^2\tan\theta_0)}\lim_{\gamma\to\infty} C(\gamma,\alpha)\langle U^\alpha_{\theta_0-\theta}G_\gamma, w(R^\alpha_{-\theta}(0,\alpha^2 t_0\tan\theta_0-\xi))^* w(t_0,\xi)^*\tilde{g}^{(\alpha)}_{t',\xi'}\rangle$$

$$= e^{\frac{i}{2}(-t_0\xi+\alpha^2 t_0^2\tan\theta_0)}e^{-\frac{i}{2}[(\alpha^2 t_0\tan\theta_0-\xi)t_0\cos\theta-(t_0\tan\theta_0-\frac{\xi}{\alpha^2})\xi\sin\theta]}$$

$$\cdot\lim_{\gamma\to\infty} C(\gamma,\alpha)\langle U^\alpha_{\theta_0-\theta}G_\gamma, w(-(t_0\tan\theta_0-\frac{\xi}{\alpha^2})\sin\theta-t_0,-(\alpha^2 t_0\tan\theta_0-\xi)\cos\theta-\xi)\tilde{g}^{(\alpha)}_{t',\xi'}\rangle$$

$$= e^{\frac{i}{2}(-t_0\xi+\alpha^2 t_0^2\tan\theta_0)}e^{-\frac{i}{2}[(\alpha^2 t_0\tan\theta_0-\xi)t_0\cos\theta-(t_0\tan\theta_0-\frac{\xi}{\alpha^2})\xi\sin\theta]}$$

$$\cdot e^{-\frac{i}{2}[(-(\alpha^2 t_0\tan\theta_0-\xi)\cos\theta-\xi)t'+((t_0\tan\theta_0-\frac{\xi}{\alpha^2})\sin\theta+t_0)\xi']}$$

$$\cdot\lim_{\gamma\to\infty} C(\gamma,\alpha)\langle U^\alpha_{\theta_0-\theta}G_\gamma,\tilde{g}^{(\alpha)}_{(\frac{\xi}{\alpha^2}-t_0\tan\theta_0)\sin\theta-t_0+t',(\xi-\alpha^2 t_0\tan\theta_0)\cos\theta-\xi+\xi'}\rangle$$

$$= e^{\frac{i}{2}(-t_0\xi+\alpha^2 t_0^2\tan\theta_0)}e^{-\frac{i}{2}[(\alpha^2 t_0\tan\theta_0-\xi)t_0\cos\theta-(t_0\tan\theta_0-\frac{\xi}{\alpha^2})\xi\sin\theta]}$$

$$\cdot e^{-\frac{i}{2}[(-(\alpha^2 t_0\tan\theta_0-\xi)\cos\theta-\xi)t'+((t_0\tan\theta_0-\frac{\xi}{\alpha^2})\sin\theta+t_0)\xi']}$$

$$\cdot e^{-\frac{[((\xi-\alpha^2 t_0\tan\theta_0)\cos\theta-\xi+\xi')\cos(\theta_0-\theta)-\alpha^2((\frac{\xi}{\alpha^2}-t_0\tan\theta_0)\sin\theta-t_0+t')\sin(\theta_0-\theta)]^2}{2\alpha^2}}$$

$$\cdot e^{-\frac{i}{2}((\frac{\xi}{\alpha^2}-t_0\tan\theta_0)\sin\theta-t_0+t')((\xi-\alpha^2 t_0\tan\theta_0)\cos\theta-\xi+\xi')\cos 2(\theta_0-\theta)}$$

$$\cdot e^{-\frac{i}{2}\frac{\sin 2(\theta_0-\theta)}{2}(\frac{((\xi-\alpha^2 t_0\tan\theta_0)\cos\theta-\xi+\xi')^2}{\alpha^2}-\alpha^2((\frac{\xi}{\alpha^2}-t_0\tan\theta_0)\sin\theta-t_0+t')^2)}$$

$$= e^{-\frac{(\cos\theta_0-\cos(\theta_0-\theta))^2}{2\alpha^2}[\xi+\frac{\xi'\cos(\theta_0-\theta)-\alpha^2 t_0\sin\theta_0-(t'-t_0)\alpha^2\sin(\theta_0-\theta)}{\cos\theta_0-\cos(\theta_0-\theta)}]^2}$$

$$\cdot e^{-\frac{i}{2}[\frac{\sin\theta}{\alpha^2}\xi^2+(t_0-t_0\cos\theta-t_0\tan\theta_0\sin\theta+t'\cos\theta-t'-\frac{\xi'\sin\theta}{\alpha^2})\xi]}$$

$$\cdot e^{-\frac{i}{2}[\alpha^2 t_0(t_0-t')\tan\theta_0\cos\theta-\alpha^2 t_0^2\tan\theta_0+\xi' t_0+\xi' t_0\tan\theta_0\sin\theta]}$$

$$\cdot e^{-\frac{i}{2}[\frac{(\xi-\alpha^2 t_0\tan\theta_0)^2}{2\alpha^2}\sin 2\theta_0+\frac{(\xi-\alpha^2 t_0\tan\theta_0)(\xi'-\xi)}{\alpha^2}\sin(2\theta_0-\theta)+(\xi-\alpha^2 t_0\tan\theta_0)(t'-t_0)\cos(2\theta_0-\theta)]}$$

$$\cdot e^{-\frac{i}{2}[\frac{\sin(2\theta_0-2\theta)}{2\alpha^2}(\xi'-\xi)^2+(\xi'-\xi)(t'-t_0)\cos(2\theta_0-2\theta)-\frac{\alpha^2\sin(2\theta_0-2\theta)}{2}(t'-t_0)^2]}$$

$$= e^{-\frac{(\cos\theta_0-\cos(\theta_0-\theta))^2}{2\alpha^2}[\xi+\frac{\xi'\cos(\theta_0-\theta)-\alpha^2 t_0\sin\theta_0-(t'-t_0)\alpha^2\sin(\theta_0-\theta)}{\cos\theta_0-\cos(\theta_0-\theta)}]^2}$$

$$\cdot\, e^{-\frac{i}{2}[(\frac{\sin\theta}{\alpha^2}+\frac{\sin 2\theta_0}{2\alpha^2}-\frac{\sin(2\theta_0-\theta)}{\alpha^2}+\frac{\sin(2\theta_0-2\theta)}{2\alpha^2})\xi^2]}$$

$$\cdot\, e^{-\frac{i}{2}[(-t_0\sin 2\theta_0\tan\theta_0+\frac{\xi'\sin(2\theta_0-\theta)}{\alpha^2}+t_0\tan\theta_0\sin(2\theta_0-\theta)+(t'-t_0)\cos(2\theta_0-\theta)-\frac{\xi'\sin(2\theta_0-2\theta)}{\alpha^2})\xi]}$$

$$\cdot\, e^{-\frac{i}{2}[(-(t'-t_0)\cos(2\theta_0-2\theta)+t_0-t_0\cos\theta-t_0\tan\theta_0\sin\theta+t'\cos\theta-t'-\frac{\xi'\sin\theta}{\alpha^2})\xi]}$$

$$\cdot\, e^{-\frac{i}{2}[\alpha^2 t_0(t_0-t')\tan\theta_0\cos\theta-\alpha^2 t_0^2\tan\theta_0+\xi' t_0+\xi' t_0\tan\theta_0\sin\theta]}$$

$$\cdot\, e^{-\frac{i}{2}[\frac{1}{2}\alpha^2 t_0^2\tan^2\theta_0\sin 2\theta_0-\xi' t_0\tan\theta_0\sin(2\theta_0-\theta)-\alpha^2 t_0\tan\theta_0(t'-t_0)\cos(2\theta_0-\theta)+\frac{\sin(2\theta_0-2\theta)}{2\alpha^2}\xi'^2]}$$

$$\cdot\, e^{-\frac{i}{2}[\xi'(t'-t_0)\cos(2\theta_0-2\theta)-\frac{\alpha^2\sin(2\theta_0-2\theta)}{2}(t'-t_0)^2]}.$$

Moreover, we have

$$\begin{aligned}
&\left|\langle w(t_0,\xi)U^\alpha_{-\theta}w(t_0,\xi)^* f,\tilde{g}^{(\alpha)}_{t',\xi'}\rangle\right| \\
&=\left|\langle w(t_0,\xi)U^\alpha_{-\theta}w(t_0,\xi)^* w(t_0,\alpha^2 t_0\tan\theta_0)U^\alpha_{\theta_0}G_\gamma,\tilde{g}^{(\alpha)}_{t',\xi'}\rangle\right| \\
&=\left|\langle U^\alpha_{-\theta}w(0,\alpha^2 t_0\tan\theta_0-\xi)U^\alpha_{\theta_0}G_\gamma, w(t_0,\xi)^*\tilde{g}^{(\alpha)}_{t',\xi'}\rangle\right| \\
&=\left|\langle w(R^\alpha_{-\theta}(0,\alpha^2 t_0\tan\theta_0-\xi))U^\alpha_{\theta_0-\theta}G_\gamma,\tilde{g}^{(\alpha)}_{t'-t_0,\xi'-\xi}\rangle\right| \\
&=\left|\langle w(\frac{\sin\theta(\alpha^2 t_0\tan\theta_0-\xi)}{\alpha^2},(\alpha^2 t_0\tan\theta_0-\xi)\cos\theta)U^\alpha_{\theta_0-\theta}G_\gamma,\tilde{g}^{(\alpha)}_{t'-t_0,\xi'-\xi}\rangle\right| \\
&=\left|\langle U^\alpha_{\theta_0-\theta}G_\gamma,\tilde{g}^{(\alpha)}_{t'-t_0-\frac{\sin\theta(\alpha^2 t_0\tan\theta_0-\xi)}{\alpha^2},\xi'-\xi-(\alpha^2 t_0\tan\theta_0-\xi)\cos\theta}\rangle\right| \\
&\le C(\gamma,\alpha)^{-1}e^{-\frac{\gamma}{2(1+\alpha^2\gamma)}[(\xi'-\xi-(\alpha^2 t_0\tan\theta_0-\xi)\cos\theta)\cos(\theta_0-\theta)-\alpha^2(t'-t_0-\frac{\sin\theta(\alpha^2 t_0\tan\theta_0-\xi)}{\alpha^2})\sin(\theta_0-\theta)]^2}.
\end{aligned}$$

Since the derivative of $\frac{\gamma}{1+\alpha^2\gamma}$ is $\frac{1}{(1+\alpha^2\gamma)^2}$, which is strictly positive, we have $\frac{\gamma}{1+\alpha^2\gamma}\ge\frac{1}{1+\alpha^2}$ for all $\gamma\ge 1$. So

$$\begin{aligned}
&e^{-\frac{\gamma}{2(1+\alpha^2\gamma)}[(\xi'-\xi-(\alpha^2 t_0\tan\theta_0-\xi)\cos\theta)\cos(\theta_0-\theta)-\alpha^2(t'-t_0-\frac{\sin\theta(\alpha^2 t_0\tan\theta_0-\xi)}{\alpha^2})\sin(\theta_0-\theta)]^2} \\
&\le e^{-\frac{1}{2(1+\alpha^2)}[(\xi'-\xi-(\alpha^2 t_0\tan\theta_0-\xi)\cos\theta)\cos(\theta_0-\theta)-\alpha^2(t'-t_0-\frac{\sin\theta(\alpha^2 t_0\tan\theta_0-\xi)}{\alpha^2})\sin(\theta_0-\theta)]^2}
\end{aligned}$$

uniformly in γ. And the right hand side is clearly integrable with respect to ξ. Therefore, by the dominated convergence theorem, we can interchange the limit with the integral sign; that is,

$$\lim_{\gamma\to\infty}C(\gamma,\alpha)\langle T_{\alpha,t_0,\theta}f,\tilde{g}^{(\alpha)}_{t',\xi'}\rangle$$

$$
\begin{aligned}
&= \int \lim_{\gamma\to\infty} C(\gamma,\alpha)\langle w(t_0,\xi)U_{-\theta}^{\alpha} w(t_0,\xi)^* f, \tilde{g}^{(\alpha)}_{t',\xi'}\rangle \,\mathrm{d}\xi \\
&= \int e^{-\frac{(\cos\theta_0-\cos(\theta_0-\theta))^2}{2\alpha^2}[\xi+\frac{\xi'\cos(\theta_0-\theta)-\alpha^2 t_0\sin\theta_0-(t'-t_0)\alpha^2\sin(\theta_0-\theta)}{\cos\theta_0-\cos(\theta_0-\theta)}]^2} \\
&\quad \cdot e^{-\frac{i}{2}[(\frac{\sin\theta}{\alpha^2}+\frac{\sin 2\theta_0}{2\alpha^2}-\frac{\sin(2\theta_0-\theta)}{\alpha^2}+\frac{\sin(2\theta_0-2\theta)}{2\alpha^2})\xi^2]} \\
&\quad \cdot e^{-\frac{i}{2}[(-t_0\sin 2\theta_0\tan\theta_0+\frac{\xi'\sin(2\theta_0-\theta)}{\alpha^2}+t_0\tan\theta_0\sin(2\theta_0-\theta)+(t'-t_0)\cos(2\theta_0-\theta)-\frac{\xi'\sin(2\theta_0-2\theta)}{\alpha^2})\xi]} \\
&\quad \cdot e^{-\frac{i}{2}[(-(t'-t_0)\cos(2\theta_0-2\theta)+t_0-t_0\cos\theta-t_0\tan\theta_0\sin\theta+t'\cos\theta-t'-\frac{\xi'\sin\theta}{\alpha^2})\xi]}\,\mathrm{d}\xi \\
&\quad \cdot e^{-\frac{i}{2}[\alpha^2 t_0(t_0-t')\tan\theta_0\cos\theta-\alpha^2 t_0^2\tan\theta_0+\xi' t_0+\xi' t_0\tan\theta_0\sin\theta]} \\
&\quad \cdot e^{-\frac{i}{2}[\frac{1}{2}\alpha^2 t_0^2\tan^2\theta_0\sin 2\theta_0-\xi' t_0\tan\theta_0\sin(2\theta_0-\theta)-\alpha^2 t_0\tan\theta_0(t'-t_0)\cos(2\theta_0-\theta)+\frac{\sin(2\theta_0-2\theta)}{2\alpha^2}\xi'^2]} \\
&\quad \cdot e^{-\frac{i}{2}[\xi'(t'-t_0)\cos(2\theta_0-2\theta)-\frac{\alpha^2\sin(2\theta_0-2\theta)}{2}(t'-t_0)^2]}.
\end{aligned}
$$

The integral above can be computed by a change of variable

$$
\xi \to \xi - \frac{\xi'\cos(\theta_0-\theta)-\alpha^2 t_0\sin\theta_0-(t'-t_0)\alpha^2\sin(\theta_0-\theta)}{\cos\theta_0-\cos(\theta_0-\theta)},
$$

$$
\begin{aligned}
&\int e^{-\frac{(\cos\theta_0-\cos(\theta_0-\theta))^2}{2\alpha^2}[\xi+\frac{\xi'\cos(\theta_0-\theta)-\alpha^2 t_0\sin\theta_0-(t'-t_0)\alpha^2\sin(\theta_0-\theta)}{\cos\theta_0-\cos(\theta_0-\theta)}]^2} \\
&\quad \cdot e^{-\frac{i}{2}[(\frac{\sin\theta}{\alpha^2}+\frac{\sin 2\theta_0}{2\alpha^2}-\frac{\sin(2\theta_0-\theta)}{\alpha^2}+\frac{\sin(2\theta_0-2\theta)}{2\alpha^2})\xi^2]} \\
&\quad \cdot e^{-\frac{i}{2}[(-t_0\sin 2\theta_0\tan\theta_0+\frac{\xi'\sin(2\theta_0-\theta)}{\alpha^2}+t_0\tan\theta_0\sin(2\theta_0-\theta)+(t'-t_0)\cos(2\theta_0-\theta)-\frac{\xi'\sin(2\theta_0-2\theta)}{\alpha^2})\xi]} \\
&\quad \cdot e^{-\frac{i}{2}[(-(t'-t_0)\cos(2\theta_0-2\theta)+t_0-t_0\cos\theta-t_0\tan\theta_0\sin\theta+t'\cos\theta-t'-\frac{\xi'\sin\theta}{\alpha^2})\xi]}\,\mathrm{d}\xi \\
&= \int e^{-C_1(\alpha,\theta_0,\theta)\xi^2} \\
&\quad \cdot e^{-\frac{i}{2}[-2(\frac{\sin\theta}{\alpha^2}+\frac{\sin 2\theta_0}{2\alpha^2}-\frac{\sin(2\theta_0-\theta)}{\alpha^2}+\frac{\sin(2\theta_0-2\theta)}{2\alpha^2})\frac{\xi'\cos(\theta_0-\theta)-\alpha^2 t_0\sin\theta_0-(t'-t_0)\alpha^2\sin(\theta_0-\theta)}{\cos\theta_0-\cos(\theta_0-\theta)}\xi]} \\
&\quad \cdot e^{-\frac{i}{2}[(-t_0\sin 2\theta_0\tan\theta_0+\frac{\xi'\sin(2\theta_0-\theta)}{\alpha^2}+t_0\tan\theta_0\sin(2\theta_0-\theta)+(t'-t_0)\cos(2\theta_0-\theta)-\frac{\xi'\sin(2\theta_0-2\theta)}{\alpha^2})\xi]} \\
&\quad \cdot e^{-\frac{i}{2}[(-(t'-t_0)\cos(2\theta_0-2\theta)+t_0-t_0\cos\theta-t_0\tan\theta_0\sin\theta+t'\cos\theta-t'-\frac{\xi'\sin\theta}{\alpha^2})\xi]}\,\mathrm{d}\xi \\
&\quad \cdot e^{-\frac{i}{2}(\frac{\sin\theta}{\alpha^2}+\frac{\sin 2\theta_0}{2\alpha^2}-\frac{\sin(2\theta_0-\theta)}{\alpha^2}+\frac{\sin(2\theta_0-2\theta)}{2\alpha^2})(\frac{\xi'\cos(\theta_0-\theta)-\alpha^2 t_0\sin\theta_0-(t'-t_0)\alpha^2\sin(\theta_0-\theta)}{\cos\theta_0-\cos(\theta_0-\theta)})^2} \\
&\cdot e^{\frac{i}{2}[(-t_0\sin 2\theta_0\tan\theta_0+\frac{\xi'\sin(2\theta_0-\theta)}{\alpha^2}+t_0\tan\theta_0\sin(2\theta_0-\theta)+(t'-t_0)\cos(2\theta_0-\theta)-\frac{\xi'\sin(2\theta_0-2\theta)}{\alpha^2})\frac{\xi'\cos(\theta_0-\theta)-\alpha^2 t_0\sin\theta_0-(t'-t_0)\alpha^2\sin(\theta_0-\theta}{\cos\theta_0-\cos(\theta_0-\theta)}} \\
&\cdot e^{\frac{i}{2}[(-(t'-t_0)\cos(2\theta_0-2\theta)+t_0-t_0\cos\theta-t_0\tan\theta_0\sin\theta+t'\cos\theta-t'-\frac{\xi'\sin\theta}{\alpha^2})\frac{\xi'\cos(\theta_0-\theta)-\alpha^2 t_0\sin\theta_0-(t'-t_0)\alpha^2\sin(\theta_0-\theta)}{\cos\theta_0-\cos(\theta_0-\theta)}]},
\end{aligned}
$$

The second to the fourth term inside the integral can be written as

$$
e^{-\frac{i}{2}[-2(\frac{\sin\theta}{\alpha^2}+\frac{\sin 2\theta_0}{2\alpha^2}-\frac{\sin(2\theta_0-\theta)}{\alpha^2}+\frac{\sin(2\theta_0-2\theta)}{2\alpha^2})(\frac{(\xi'-\alpha^2 t_0\tan\theta_0)\cos(\theta_0-\theta)-(t'-t_0)\alpha^2\sin(\theta_0-\theta)}{\cos\theta_0-\cos(\theta_0-\theta)}-\alpha^2 t_0\tan\theta_0)]\xi}
$$

$$\cdot\, e^{-\frac{i}{2}[(-t_0\sin 2\theta_0\tan\theta_0+\frac{\xi'\sin(2\theta_0-\theta)}{\alpha^2}+t_0\tan\theta_0\sin(2\theta_0-\theta)+(t'-t_0)\cos(2\theta_0-\theta)-\frac{\xi'\sin(2\theta_0-2\theta)}{\alpha^2})]\xi}$$

$$\cdot\, e^{-\frac{i}{2}[(-(t'-t_0)\cos(2\theta_0-2\theta)+t_0-t_0\cos\theta-t_0\tan\theta_0\sin\theta+t'\cos\theta-t'-\frac{\xi'\sin\theta}{\alpha^2})]\xi}$$

$$= e^{-\frac{i}{2}[(-\frac{2\cos(\theta_0-\theta)}{\cos\theta_0-\cos(\theta_0-\theta)}(\frac{\sin\theta}{\alpha^2}+\frac{\sin 2\theta_0}{2\alpha^2}-\frac{\sin(2\theta_0-\theta)}{\alpha^2}+\frac{\sin(2\theta_0-2\theta)}{2\alpha^2})+\frac{\sin(2\theta_0-\theta)}{\alpha^2}-\frac{\sin(2\theta_0-2\theta)}{\alpha^2}-\frac{\sin\theta}{\alpha^2})(\xi'-\alpha^2t_0\tan\theta_0)]\xi}$$

$$\cdot\, e^{-\frac{i}{2}[(\frac{2\alpha^2\sin(\theta_0-\theta)}{\cos\theta_0-\cos(\theta_0-\theta)}(\frac{\sin\theta}{\alpha^2}+\frac{\sin 2\theta_0}{2\alpha^2}-\frac{\sin(2\theta_0-\theta)}{\alpha^2}+\frac{\sin(2\theta_0-2\theta)}{2\alpha^2})+\cos(2\theta_0-\theta)-1-\cos(2\theta_0-2\theta)+\cos\theta)(t'-t_0)]\xi}$$

$$= e^{-\frac{i}{2}[C_2(\alpha,\theta_0,\theta)(t'-t_0)-C_3(\alpha,\theta_0,\theta)(\xi'-\alpha^2t_0\tan\theta_0)]\xi}.$$

Hence the above integral would be

$$\int e^{-C_1(\alpha,\theta_0,\theta)\xi^2}e^{-\frac{i}{2}[-2(\frac{\sin\theta}{\alpha^2}+\frac{\sin 2\theta_0}{2\alpha^2}-\frac{\sin(2\theta_0-\theta)}{\alpha^2}+\frac{\sin(2\theta_0-2\theta)}{2\alpha^2})\frac{\xi'\cos(\theta_0-\theta)-\alpha^2t_0\sin\theta_0-(t'-t_0)\alpha^2\sin(\theta_0-\theta)}{\cos\theta_0-\cos(\theta_0-\theta)}\xi]}$$

$$\cdot\, e^{-\frac{i}{2}[(-t_0\sin 2\theta_0\tan\theta_0+\frac{\xi'\sin(2\theta_0-\theta)}{\alpha^2}+t_0\tan\theta_0\sin(2\theta_0-\theta)+(t'-t_0)\cos(2\theta_0-\theta)-\frac{\xi'\sin(2\theta_0-2\theta)}{\alpha^2})\xi]}$$

$$\cdot\, e^{-\frac{i}{2}[(-(t'-t_0)\cos(2\theta_0-2\theta)+t_0-t_0\cos\theta-t_0\tan\theta_0\sin\theta+t'\cos\theta-t'-\frac{\xi'\sin\theta}{\alpha^2})\xi]}\,\mathrm{d}\xi$$

$$= \sqrt{\frac{\pi}{C_1(\alpha,\theta_0,\theta)}}e^{-\frac{[C_2(\alpha,\theta_0,\theta)(t'-t_0)-C_3(\alpha,\theta_0,\theta)(\xi'-\alpha^2t_0\tan\theta_0)]^2}{16C_1(\alpha,\theta_0,\theta)}}.$$

Combining the computations above, we thus get

$$\lim_{\gamma\to\infty}C(\gamma,\alpha)\langle T_{\alpha,t_0,\theta}f,\tilde{g}^{(\alpha)}_{t',\xi'}\rangle$$

$$= \sqrt{\frac{\pi}{C_1(\alpha,\theta_0,\theta)}}e^{-\frac{[C_2(\alpha,\theta_0,\theta)(t'-t_0)-C_3(\alpha,\theta_0,\theta)(\xi'-\alpha^2t_0\tan\theta_0)]^2}{16C_1(\alpha,\theta_0,\theta)}}$$

$$\cdot\, e^{-\frac{i}{2}[\alpha^2t_0(t_0-t')\tan\theta_0\cos\theta-\alpha^2t_0^2\tan\theta_0+\xi't_0+\xi't_0\tan\theta_0\sin\theta]}$$

$$\cdot\, e^{-\frac{i}{2}[\frac{1}{2}\alpha^2t_0^2\tan^2\theta_0\sin 2\theta_0-\xi't_0\tan\theta_0\sin(2\theta_0-\theta)-\alpha^2t_0\tan\theta_0(t'-t_0)\cos(2\theta_0-\theta)+\frac{\sin(2\theta_0-2\theta)}{2\alpha^2}\xi'^2]}$$

$$\cdot\, e^{-\frac{i}{2}[\xi'(t'-t_0)\cos(2\theta_0-2\theta)-\frac{\alpha^2\sin(2\theta_0-2\theta)}{2}(t'-t_0)^2]}$$

$$\cdot\, e^{-\frac{i}{2}(\frac{\sin\theta}{\alpha^2}+\frac{\sin 2\theta_0}{2\alpha^2}-\frac{\sin(2\theta_0-\theta)}{\alpha^2}+\frac{\sin(2\theta_0-2\theta)}{2\alpha^2})(\frac{\xi'\cos(\theta_0-\theta)-\alpha^2t_0\sin\theta_0-(t'-t_0)\alpha^2\sin(\theta_0-\theta)}{\cos\theta_0-\cos(\theta_0-\theta)})^2}$$

$$\cdot\, e^{\frac{i}{2}[(-t_0\sin 2\theta_0\tan\theta_0+\frac{\xi'\sin(2\theta_0-\theta)}{\alpha^2}+t_0\tan\theta_0\sin(2\theta_0-\theta)+(t'-t_0)\cos(2\theta_0-\theta)-\frac{\xi'\sin(2\theta_0-2\theta)}{\alpha^2})\frac{\xi'\cos(\theta_0-\theta)-\alpha^2t_0\sin\theta_0-(t'-t_0)\alpha^2\sin(\theta_0-\theta}{\cos\theta_0-\cos(\theta_0-\theta)}}$$

$$\cdot\, e^{\frac{i}{2}[(-(t'-t_0)\cos(2\theta_0-2\theta)+t_0-t_0\cos\theta-t_0\tan\theta_0\sin\theta+t'\cos\theta-t'-\frac{\xi'\sin\theta}{\alpha^2})\frac{\xi'\cos(\theta_0-\theta)-\alpha^2t_0\sin\theta_0-(t'-t_0)\alpha^2\sin(\theta_0-\theta)}{\cos\theta_0-\cos(\theta_0-\theta)}]}.$$

□

These expressions are quite complicated. Let us see what they represent. Suppose $k_0 = \alpha^2\tan\theta_0$ and $k = \alpha^2\tan\theta$ are fixed, i.e. θ_0 and θ would change as α varies. To see where $T_{\alpha,t_0,\theta}f$ is concentrated in TF plane, we have the following lemma

Lemma 6.

$$\lim_{\alpha\to\infty}\frac{C_2(\alpha,\theta_0,\theta)}{C_3(\alpha,\theta_0,\theta)}=k_0-k.$$

Proof. For $\theta_0=\arctan(\frac{k_0}{\alpha^2})$, we have

$$\sin\theta_0=\frac{k_0}{\alpha^2\sqrt{1+\frac{k_0^2}{\alpha^4}}},\cos\theta_0=\frac{1}{\sqrt{1+\frac{k_0^2}{\alpha^4}}},$$

so

$$\sin 2\theta_0=\frac{2k_0}{\alpha^2(1+\frac{k_0^2}{\alpha^4})},\cos 2\theta_0=\frac{1}{1+\frac{k_0^2}{\alpha^4}}-\frac{k_0^2}{\alpha^4(1+\frac{k_0^2}{\alpha^4})}.$$

Similar relations also hold for θ and k. We first look at

$$C_2(\alpha,\theta_0,\theta)=\frac{2\alpha^2\sin(\theta_0-\theta)}{\cos\theta_0-\cos(\theta_0-\theta)}(\frac{\sin\theta}{\alpha^2}+\frac{\sin 2\theta_0}{2\alpha^2}-\frac{\sin(2\theta_0-\theta)}{\alpha^2}+\frac{\sin(2\theta_0-2\theta)}{2\alpha^2})$$
$$+\cos(2\theta_0-\theta)-1-\cos(2\theta_0-2\theta)+\cos\theta.$$

$$\begin{aligned}\frac{2\alpha^2\sin(\theta_0-\theta)}{\cos\theta_0-\cos(\theta_0-\theta)}&=\frac{2\alpha^2(\frac{k_0}{\alpha^2\sqrt{1+\frac{k_0^2}{\alpha^4}}}\frac{1}{\sqrt{1+\frac{k^2}{\alpha^4}}}-\frac{1}{\sqrt{1+\frac{k_0^2}{\alpha^4}}}\frac{k}{\alpha^2\sqrt{1+\frac{k^2}{\alpha^4}}})}{\frac{1}{\sqrt{1+\frac{k_0^2}{\alpha^4}}}-\frac{1}{\sqrt{1+\frac{k_0^2}{\alpha^4}}\sqrt{1+\frac{k^2}{\alpha^4}}}-\frac{k_0k}{\alpha^4\sqrt{1+\frac{k_0^2}{\alpha^4}}\sqrt{1+\frac{k^2}{\alpha^4}}}}\\&=\frac{2(k_0-k)}{\sqrt{1+\frac{k^2}{\alpha^4}}-1-\frac{k_0k}{\alpha^4}}\\&=\frac{2(k_0-k)(\sqrt{1+\frac{k^2}{\alpha^4}}+1+\frac{k_0k}{\alpha^4})}{1+\frac{k^2}{\alpha^4}-(1+\frac{k_0k}{\alpha^4})^2}\\&=\frac{2(k_0-k)(\sqrt{1+\frac{k^2}{\alpha^4}}+1+\frac{k_0k}{\alpha^4})}{\frac{k^2}{\alpha^4}-\frac{2k_0k}{\alpha^4}-\frac{k_0^2k^2}{\alpha^8}}\\&=\frac{2\alpha^4(k_0-k)(\sqrt{1+\frac{k^2}{\alpha^4}}+1+\frac{k_0k}{\alpha^4})}{k^2-2k_0k-\frac{k_0^2k^2}{\alpha^4}},\end{aligned}$$

and

$$\begin{aligned}&\frac{\sin\theta}{\alpha^2}+\frac{\sin 2\theta_0}{2\alpha^2}-\frac{\sin(2\theta_0-\theta)}{\alpha^2}+\frac{\sin(2\theta_0-2\theta)}{2\alpha^2}\\&=\frac{k}{\alpha^4\sqrt{1+\frac{k^2}{\alpha^4}}}+\frac{k_0}{\alpha^4(1+\frac{k_0^2}{\alpha^4})}-\frac{2k_0}{\alpha^4(1+\frac{k_0^2}{\alpha^4})\sqrt{1+\frac{k^2}{\alpha^4}}}+\frac{k}{\alpha^4\sqrt{1+\frac{k^2}{\alpha^4}}}(\frac{1}{1+\frac{k_0^2}{\alpha^4}}-\frac{k_0^2}{\alpha^4(1+\frac{k_0^2}{\alpha^4})})\end{aligned}$$

$$+\frac{1}{2\alpha^2}[\frac{2k_0}{\alpha^2(1+\frac{k_0^2}{\alpha^4})}(\frac{1}{1+\frac{k^2}{\alpha^4}}-\frac{k^2}{\alpha^4(1+\frac{k^2}{\alpha^4})})-\frac{2k}{\alpha^2(1+\frac{k^2}{\alpha^4})}(\frac{1}{1+\frac{k_0^2}{\alpha^4}}-\frac{k_0^2}{\alpha^4(1+\frac{k_0^2}{\alpha^4})})]$$
$$=\frac{1}{\alpha^4}[\frac{k}{\sqrt{1+\frac{k^2}{\alpha^4}}}+\frac{k_0}{1+\frac{k_0^2}{\alpha^4}}-\frac{2k_0}{(1+\frac{k_0^2}{\alpha^4})\sqrt{1+\frac{k^2}{\alpha^4}}}+\frac{k}{(1+\frac{k_0^2}{\alpha^4})\sqrt{1+\frac{k^2}{\alpha^4}}}+\frac{k_0}{(1+\frac{k_0^2}{\alpha^4})(1+\frac{k^2}{\alpha^4})}$$
$$-\frac{k}{(1+\frac{k_0^2}{\alpha^4})(1+\frac{k^2}{\alpha^4})}]-\frac{1}{\alpha^8}[\frac{kk_0^2}{(1+\frac{k_0^2}{\alpha^4})\sqrt{1+\frac{k^2}{\alpha^4}}}+\frac{k^2k_0}{(1+\frac{k_0^2}{\alpha^4})(1+\frac{k_0^2}{\alpha^4})}-\frac{kk_0^2}{(1+\frac{k_0^2}{\alpha^4})(1+\frac{k_0^2}{\alpha^4})}].$$

Therefore, as $\alpha\to\infty$

$$\lim_{\alpha\to\infty}\frac{2\alpha^2\sin(\theta_0-\theta)}{\cos\theta_0-\cos(\theta_0-\theta)}(\frac{\sin\theta}{\alpha^2}+\frac{\sin 2\theta_0}{2\alpha^2}-\frac{\sin(2\theta_0-\theta)}{\alpha^2}+\frac{\sin(2\theta_0-2\theta)}{2\alpha^2})=\frac{4(k_0-k)k}{k^2-2k_0k}$$
$$=\frac{4(k_0-k)}{k-2k_0}.$$

On the other hand, as $\alpha\to\infty$, θ_0 and θ both tend to 0, so

$$\lim_{\alpha\to\infty}\cos(2\theta_0-\theta)-1-\cos(2\theta_0-2\theta)+\cos\theta=0.$$

Therefore,

$$\lim_{\alpha\to\infty}C_2(\alpha,\theta_0,\theta)=\frac{4(k_0-k)}{k-2k_0}.$$

Next we investigate

$$C_3(\alpha,\theta_0,\theta)=\frac{2\cos(\theta_0-\theta)}{\cos\theta_0-\cos(\theta_0-\theta)}(\frac{\sin\theta}{\alpha^2}+\frac{\sin 2\theta_0}{2\alpha^2}-\frac{\sin(2\theta_0-\theta)}{\alpha^2}+\frac{\sin(2\theta_0-2\theta)}{2\alpha^2})$$
$$-\frac{\sin(2\theta_0-\theta)}{\alpha^2}+\frac{\sin(2\theta_0-2\theta)}{\alpha^2}+\frac{\sin\theta}{\alpha^2}.$$

Note that

$$\frac{2\cos(\theta_0-\theta)}{\cos\theta_0-\cos(\theta_0-\theta)}=\frac{2(\frac{1}{\sqrt{1+\frac{k_0^2}{\alpha^4}}\sqrt{1+\frac{k^2}{\alpha^4}}}+\frac{kk_0}{\alpha^4\sqrt{1+\frac{k_0^2}{\alpha^4}}\sqrt{1+\frac{k^2}{\alpha^4}}})}{\frac{1}{\sqrt{1+\frac{k_0^2}{\alpha^4}}}-\frac{1}{\sqrt{1+\frac{k_0^2}{\alpha^4}}\sqrt{1+\frac{k^2}{\alpha^4}}}-\frac{k_0k}{\alpha^4\sqrt{1+\frac{k_0^2}{\alpha^4}}\sqrt{1+\frac{k^2}{\alpha^4}}}}$$
$$=\frac{2(1+\frac{k_0k}{\alpha^4})}{\sqrt{1+\frac{k^2}{\alpha^4}}-1-\frac{k_0k}{\alpha^4}}$$
$$=\frac{2(1+\frac{k_0k}{\alpha^4})(\sqrt{1+\frac{k^2}{\alpha^4}}+1+\frac{k_0k}{\alpha^4})}{1+\frac{k^2}{\alpha^4}-(1+\frac{k_0k}{\alpha^4})^2}$$
$$=\frac{2(1+\frac{k_0k}{\alpha^4})(\sqrt{1+\frac{k^2}{\alpha^4}}+1+\frac{k_0k}{\alpha^4})}{\frac{k^2}{\alpha^4}-\frac{2k_0k}{\alpha^4}-\frac{k_0^2k^2}{\alpha^8}}$$

$$= \frac{2\alpha^4(1+\frac{k_0 k}{\alpha^4})(\sqrt{1+\frac{k^2}{\alpha^4}}+1+\frac{k_0 k}{\alpha^4})}{k^2-2k_0 k-\frac{k_0^2 k^2}{\alpha^4}}.$$

Therefore, as $\alpha \to \infty$

$$\lim_{\alpha\to\infty} \frac{2\cos(\theta_0-\theta)}{\cos\theta_0-\cos(\theta_0-\theta)}\left(\frac{\sin\theta}{\alpha^2}+\frac{\sin 2\theta_0}{2\alpha^2}-\frac{\sin(2\theta_0-\theta)}{\alpha^2}+\frac{\sin(2\theta_0-2\theta)}{2\alpha^2}\right) = \frac{4k}{k^2-2k_0 k}$$
$$= \frac{4}{k-2k_0}.$$

As a result,

$$\lim_{\alpha\to\infty} \frac{C_2(\alpha,\theta_0,\theta)}{C_3(\alpha,\theta_0,\theta)} = \frac{4(k_0-k)}{k-2k_0}\frac{k-2k_0}{4} = k_0-k.$$

□

Lemma 6 tells us that as α gets larger, the TF content of $T_{\alpha,t_0,\theta}f$ would be closer to the line

$$\xi = (k_0-k)t,$$

hence the operator indeed rotates the TF content of f asymptotically, in the regime where α is large.

In practice, we usually want to rotate a portion of the TF content of a signal of interest, we thus define the localized rotations:

$$\tilde{T}_{\alpha,R,t_0,\theta}f(x) := \int L^{\alpha}_{R;\theta,t,\xi} f \,\mathrm{d}\xi = \int w(t_0,\xi)U^{\alpha}_{-\theta}P^{\alpha}_{R}w(t_0,\xi)^* f(x)\,\mathrm{d}\xi. \tag{3.4}$$

We mention that to bound the difference $\left|\langle T_{\alpha,t_0,\theta}f, \tilde{g}^{(\alpha)}_{t',\xi'}\rangle - \langle \tilde{T}_{\alpha,R,t_0,\theta}f, \tilde{g}^{(\alpha)}_{t',\xi'}\rangle\right|$ for f defined as in (3.2) and for (t',ξ') close to $(t_0, \alpha^2 t_0\tan\theta_0)$, one simply note that for ξ close to $\alpha^2 t_0\tan\theta_0$, the integrand is bounded by applying Corollary 3, and both quantities $\left|\langle w(t_0,\xi)U^{\alpha}_{-\theta}P^{\alpha}_{R}w(t_0,\xi)^* f, \tilde{g}^{(\alpha)}_{t',\xi'}\rangle\right|$ and $\left|\langle w(t_0,\xi)U^{\alpha}_{-\theta}w(t_0,\xi)^* f, \tilde{g}^{(\alpha)}_{t',\xi'}\rangle\right|$ have exponential decay in ξ when ξ is far from $\alpha^2 t_0\tan\theta_0$ as seen in the proof in Proposition 12.

Figure 3.3 shows an example of the localized rotation of the signal $f(t) = \cos[2\pi(3(t-\frac{5}{2})^2+25t)]$, where we choose $\alpha = 12$, $R = 4\pi$, $t_0 = 2.5$s, and $\theta = \arctan(\frac{12\pi}{\alpha^2})$. The discretization of the integral is $\Delta\xi = 0.1$ Hz. In all cases, the inset window graphs the vertical section of the gray-scale figure at $t_0 = 2.5$s.

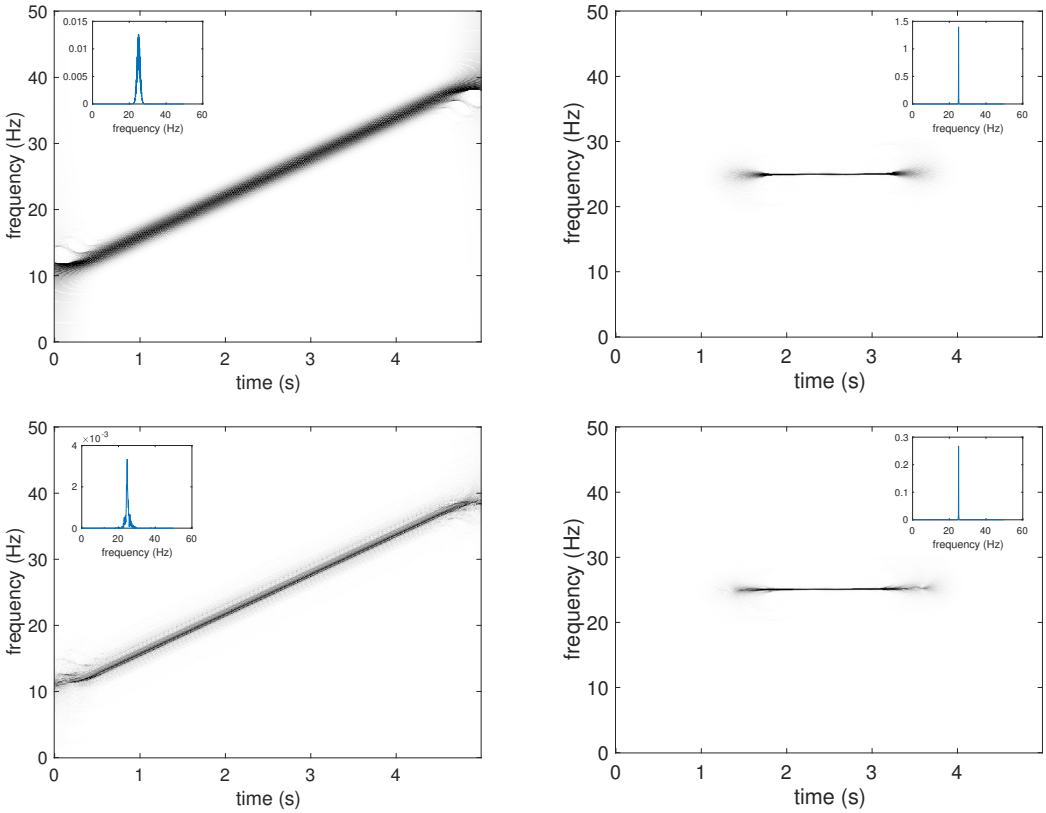

Figure 3.3: Top left: SST of f; top right: SST of $\tilde{T}_{12,4\pi,\frac{5}{2},\arctan(\frac{12\pi}{64})}f$; bottom left: ConceFT of f; bottom right: ConceFT of $\tilde{T}_{12,4\pi,\frac{5}{2},\arctan(\frac{12\pi}{64})}f$.

We show another example of a simulated signal f that consists of two oscillatory components in Figure 3.4. One of the components starts at 0 second and ends at 10-th second; the other one starts at 5-th second and ends at 16-th second. We show its SST and ConceFT results, where we use the Gaussian and the first order Hermite function in the ConceFT. We see that there is thickening phenomenon of the IF curve of the component with higher frequency in the SST at around 8.5s and 12.5s, and "splitting" in its ConceFT around these times. The two red vertical lines in its ConceFT indicate that we will perform the localized rotations at 8.5s and 12.5s respectively.

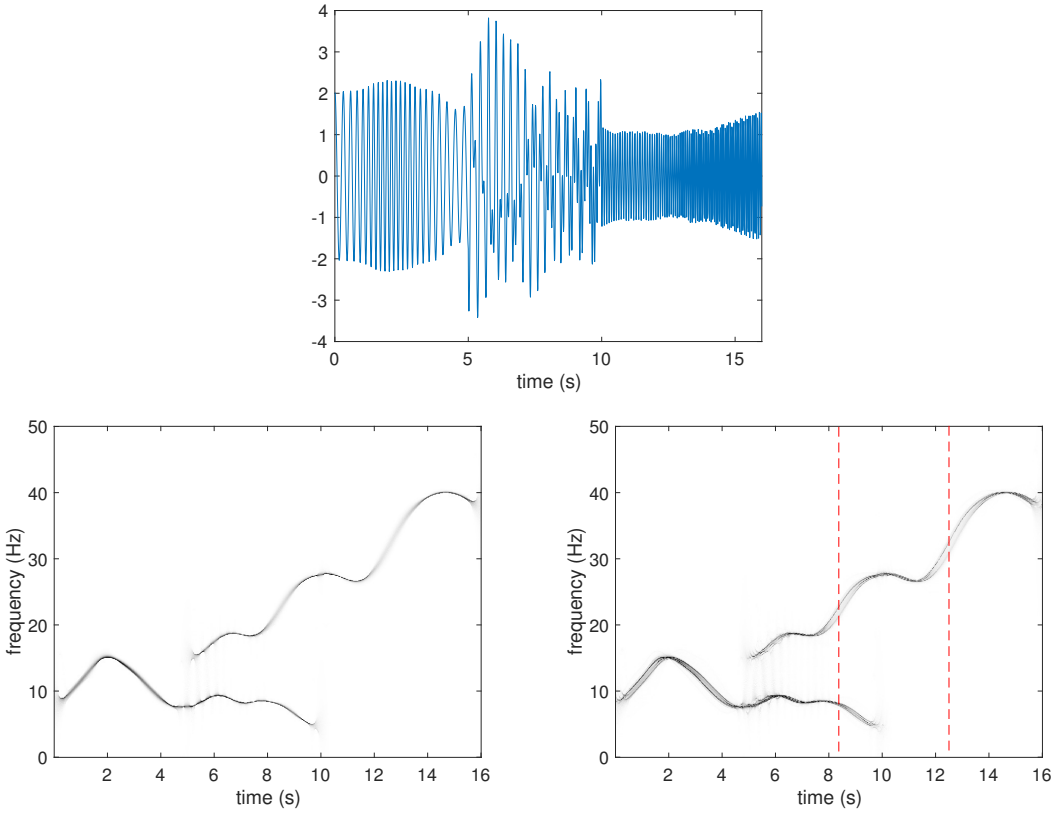

Figure 3.4: Top: plot of the signal f; Bottom left: SST of f; Bottom right: ConceFT of f.

Figure 3.5 gives the SST of the signal before and after rotations, i.e. the SST of f and $\tilde{T}_{5,10,8.5,\arctan(\frac{3}{100})}f$. In the bottom row of the figure, we show the vertical section of them

at 8.5s respectively. We see that the thickened TFR of the high-frequency component is made more concentrated after rotations.

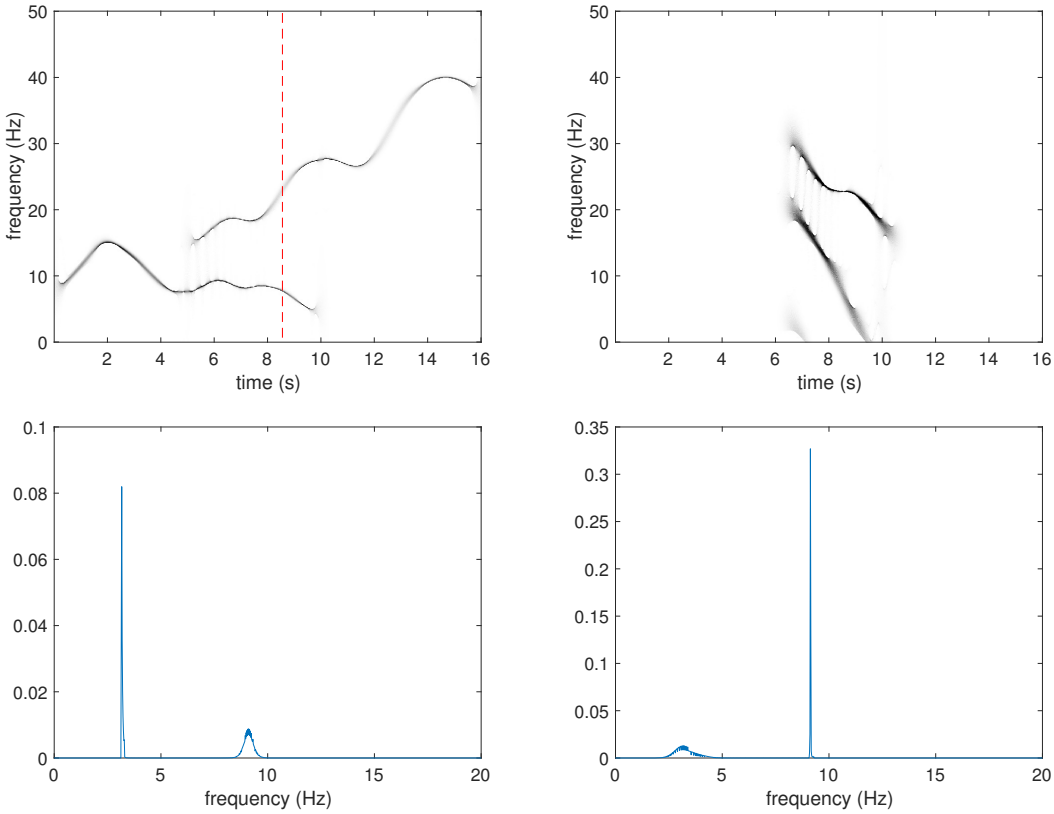

Figure 3.5: Top left: SST of f; Top right: SST of $\tilde{T}_{5,10,8.5,\arctan(\frac{3}{100})}f$. Bottom: vertical sections at 8.5s.

Figure 3.6 shows the ConceFT of f and $\tilde{T}_{5,10,8.5,\arctan(\frac{3}{100})}f$. In the bottom row of the figure, we show the vertical section of them at 8.5s respectively. We see that the splitting of the IF portion of the high-frequency component is reduced after rotations.

Figure 3.7 gives the SST of f and $\tilde{T}_{5,10,12.5,\arctan(\frac{3.2}{100})}f$. In the bottom row of the figure, we show the vertical section of them at 12.5s respectively. We observe that the thickened IF portion of the high-frequency component is made more concentrated after rotations.

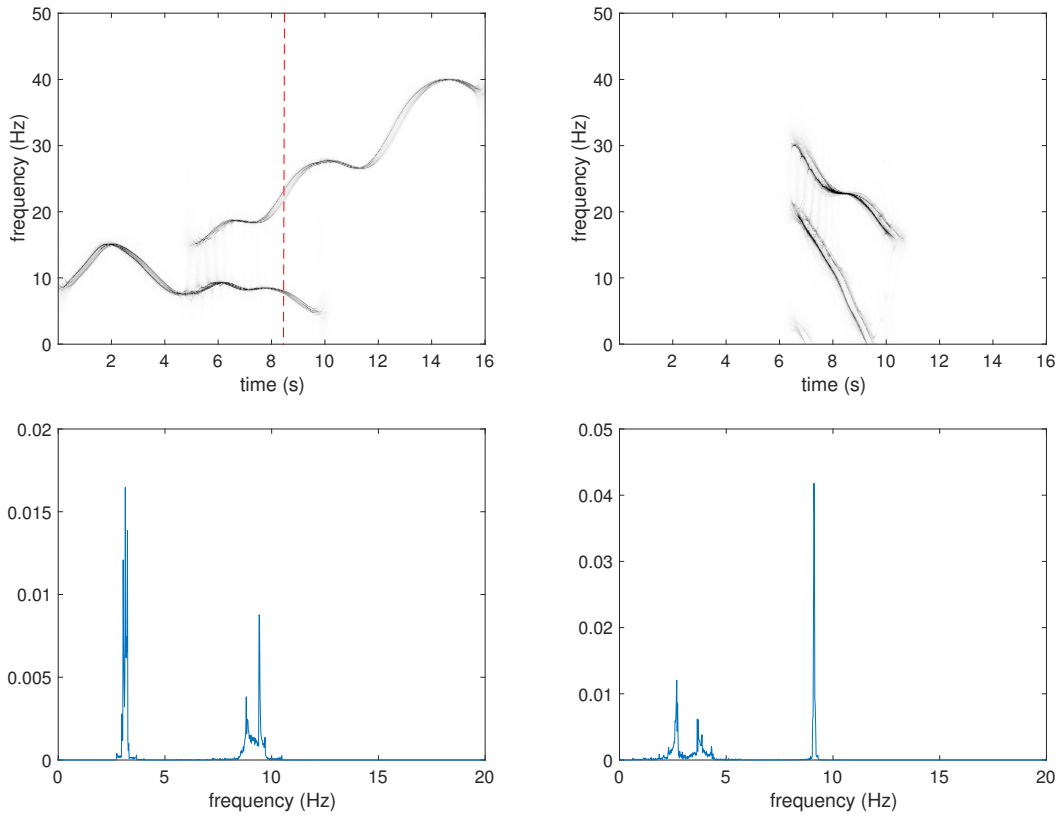

Figure 3.6: Top left: ConceFT of f; Top right: ConceFT of $\tilde{T}_{5,10,8.5,\arctan(\frac{3}{100})}f$. Bottom: vertical sections at 8.5s.

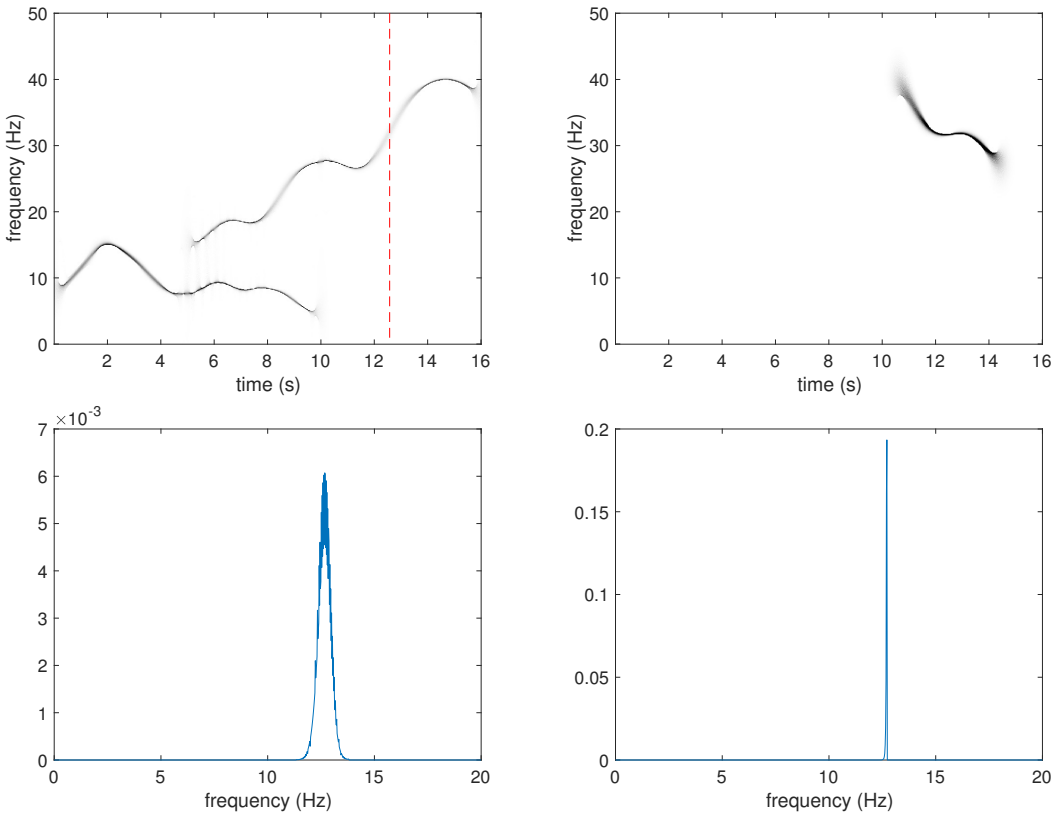

Figure 3.7: Top left: SST of f; Top right: SST of $\tilde{T}_{5,10,12.5,\arctan(\frac{3.2}{100})}f$. Bottom: vertical sections at 12.5s.

Figure 3.8 shows the ConceFT of f and $\tilde{T}_{5,10,12.5,\arctan(\frac{3.2}{100})}f$. In the bottom row of the figure, we show the vertical section of them at 12.5s respectively. We see that the splitting phenomenon is alleviated after rotations.

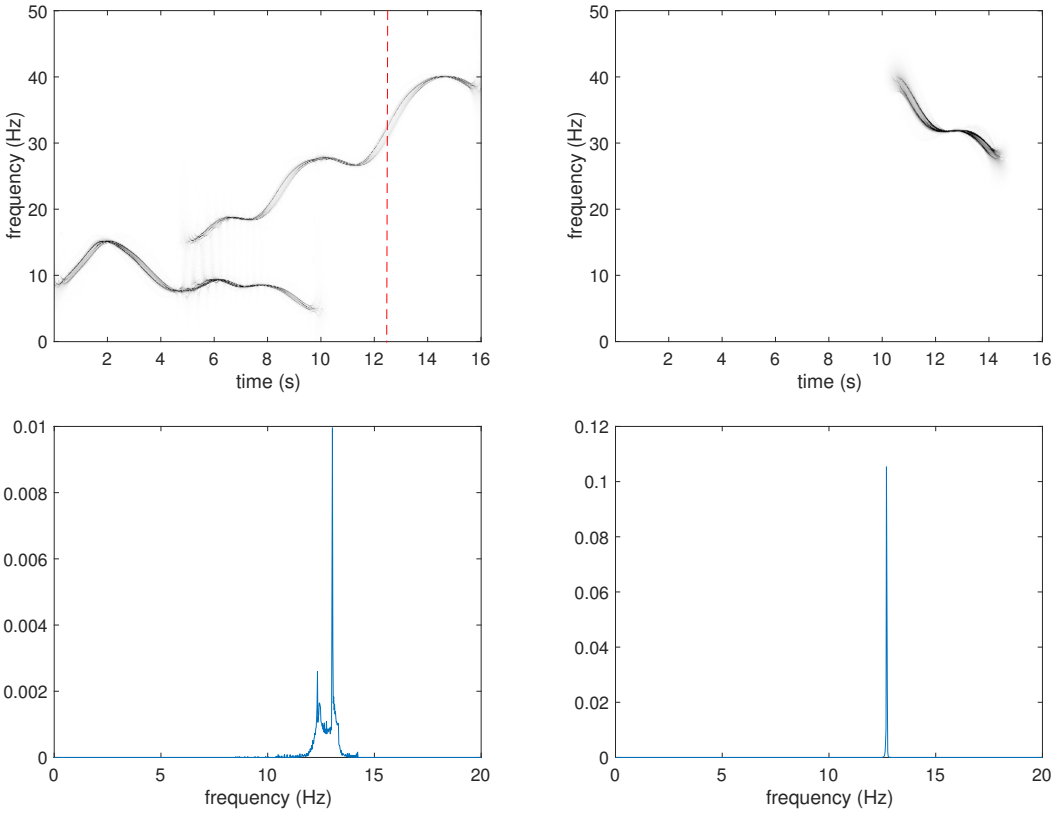

Figure 3.8: Top left: ConceFT of f; Top right: ConceFT of $\tilde{T}_{5,10,12.5,\arctan(\frac{3.2}{100})}f$. Bottom: vertical sections at 12.5s.

Chapter 4

Conclusion

We provide two new methods, the RDS and rotations in TF-plane, to address the shortcomings of the De-shape algorithm and SST (and ConceFT) respectively. We give theoretical guarantees for these new methods. In addition, numerical results are shown to demonstrate their effectiveness.

Bibliography

[1] M. Baumert, A. Porta, M. A. Vos, M. Malik, J.-P. Couderc, P. Laguna, G. Piccirillo, G. L. Smith, L. G. Tereshchenko, and P. G. Volders, *Qt interval variability in body surface ecg: measurement, physiological basis, and clinical value: position statement and consensus guidance endorsed by the european heart rhythm association jointly with the esc working group on cardiac cellular electrophysiology*, Europace, 18 (2016), pp. 925–944.

[2] B. P. Bogert, *The quefrency alanysis of time series for echoes; cepstrum, pseudo-autocovariance, cross-cepstrum and saphe cracking*, Time series analysis, (1963), pp. 209–243.

[3] S. Boyd, N. Parikh, E. Chu, B. Peleato, J. Eckstein, et al., *Distributed optimization and statistical learning via the alternating direction method of multipliers*, Foundations and Trends in Machine learning, 3 (2011), pp. 1–122.

[4] A. K. Brodzik, *Quaternionic periodicity transform: an algebraic solution to the tandem repeat detection problem*, Bioinformatics, 23 (2007), pp. 694–700.

[5] M. Buchner and S. Janjarasjitt, *Detection and visualization of tandem repeats in DNA sequences*, IEEE Transactions on Signal Processing, 51 (2003), pp. 2280–2287.

[6] S. Chen and D. Donoho, *Basis pursuit*, in Proceedings of 1994 28th Asilomar Conference on Signals, Systems and Computers, vol. 1, IEEE, 1994, pp. 41–44.

[7] S. S. Chen, D. L. Donoho, and M. A. Saunders, *Atomic decomposition by basis pursuit*, SIAM review, 43 (2001), pp. 129–159.

[8] Y.-C. Chen, M.-Y. Cheng, and H.-T. Wu, *Non-parametric and adaptive modelling of dynamic periodicity and trend with heteroscedastic and dependent errors*, J. R. Stat. Soc. Ser. B. Stat. Methodol., 76 (2014), pp. 651–682.

[9] Z. Chen and H.-T. Wu, *When ramanujan meets time-frequency analysis in complicated time series analysis*, arXiv preprint arXiv:2004.00076, (2020).

[10] H. Cheng, B. Tang, J. Du, and X. Chen, *Single channel pulse train radar signal separation using algebraic method*, in 2009 IET International Radar Conference, IET, 2009, pp. 1–4.

[11] A. Cicone and H.-T. Wu, *How nonlinear-type time-frequency analysis can help in sensing instantaneous heart rate and instantaneous respiratory rate from photoplethysmography in a reliable way*, Frontiers in physiology, 8 (2017), p. 701.

[12] G. D. Clifford, F. Azuaje, P. McSharry, et al., *Advanced methods and tools for ECG data analysis*, Artech house Boston, 2006.

[13] I. Daubechies, *Time-frequency localization operators: a geometric phase space approach*, IEEE Transactions on Information Theory, 34 (1988), pp. 605–612.

[14] ——, *Ten lectures on wavelets*, SIAM, 1992.

[15] I. Daubechies, J. Lu, and H.-T. Wu, *Synchrosqueezed wavelet transforms: An empirical mode decomposition-like tool*, Applied and Computational Harmonic Analysis, 30 (2011), pp. 243–261.

[16] I. Daubechies, Y. Wang, and H.-t. Wu, *ConceFT: Concentration of frequency and time via a multitapered synchrosqueezed transform*, Philosophical Transactions of the Royal Society A: Mathematical, Physical and Engineering Sciences, 374 (2016), p. 20150193.

[17] Z. Feng, X. Chen, and M. Liang, *Iterative generalized synchrosqueezing transform for fault diagnosis of wind turbine planetary gearbox under nonstationary conditions*, Mechanical Systems and Signal Processing, 52 (2015), pp. 360–375.

[18] A. L. Goldberger, L. A. Amaral, L. Glass, J. M. Hausdorff, P. C. Ivanov, R. G. Mark, J. E. Mietus, G. B. Moody, C.-K. Peng, and H. E. Stanley, *Physiobank, physiotoolkit, and physionet: components of a new research resource for complex physiologic signals*, circulation, 101 (2000), pp. e215–e220.

[19] R. H. Herrera, J. Han, and M. van der Baan, *Applications of the synchrosqueezing transform in seismic time-frequency analysis*, Geophysics, 79 (2014), pp. V55–V64.

[20] M. Hong and Z.-Q. Luo, *On the linear convergence of the alternating direction method of multipliers*, Mathematical Programming, 162 (2017), pp. 165–199.

[21] T. Y. Hou and Z. Shi, *Extracting a shape function for a signal with intra-wave frequency modulation*, Philosophical Transactions of the Royal Society A: Mathematical, Physical and Engineering Sciences, 374 (2016), p. 20150194.

[22] T. Kobayashi and S. Imai, *Spectral analysis using generalised cepstrum*, IEEE Transactions on Acoustics, Speech, and Signal Processing, 32 (1984), pp. 1235–1238.

[23] T. Kovács, *A novel optimization based method for separation of periodic signals*, Digital Signal Processing, 22 (2012), pp. 463–470.

[24] C. Li and M. Liang, *Time-frequency signal analysis for gearbox fault diagnosis using a generalized synchrosqueezing transform*, Mechanical Systems and Signal Processing, 26 (2012), pp. 205–217.

[25] F. Li, W. Song, C. Li, and A. Yang, *Non-harmonic analysis based instantaneous heart rate estimation from photoplethysmography*, in ICASSP 2019-2019 IEEE International Conference on Acoustics, Speech and Signal Processing (ICASSP), IEEE, 2019, pp. 1279–1283.

[26] H.-W. Liao and L. Su, *Monaural source separation using ramanujan subspace dictionaries*, IEEE Signal Processing Letters, 25 (2018), pp. 1156–1160.

[27] C.-Y. Lin, L. Su, and H.-T. Wu, *Wave-shape function analysis–when cepstrum meets time-frequency analysis*, Journal of Fourier Analysis and Applications, 24 (2018), pp. 451–505.

[28] Y.-T. Lin, Y.-L. Lo, C.-Y. Lin, M. G. Frasch, and H.-T. Wu, *Unexpected sawtooth artifact in beat-to-beat pulse transit time measured from patient monitor data*, PloS one, 14 (2019).

[29] Y.-T. Lin, J. Malik, and H.-T. Wu, *Wave-shape oscillatory model for biomedical time series with applications*, arXiv preprint arXiv:1907.00502, (2019).

[30] Y.-T. LIN, H.-T. WU, J. Tsao, H.-W. YIEN, and S.-S. HSEU, *Time-varying spectral analysis revealing differential effects of sevoflurane anaesthesia: non-rhythmic-to-rhythmic ratio*, Acta Anaesthesiologica Scandinavica, 58 (2014), pp. 157–167.

[31] Y.-T. Lin, H.-W. Yien, S.-S. Hseu, and J. Tsao, *Analyzing autonomic activity in electrocardiography about general anesthesia by spectrogram with multitaper time-frequency reassignment*, in 2011 4th International Conference on Biomedical Engineering and Informatics (BMEI), vol. 2, IEEE, 2011, pp. 630–634.

[32] S. M. Lobmaier, A. Müller, C. Zelgert, C. Shen, P. Su, G. Schmidt, B. Haller, G. Berg, B. Fabre, J. Weyrich, et al., *Fetal heart rate variability responsiveness to maternal stress, non-invasively detected from maternal transabdominal ecg*, Archives of gynecology and obstetrics, (2019), pp. 1–10.

[33] Y. Lu, H.-t. Wu, and J. Malik, *Recycling cardiogenic artifacts in impedance pneumography*, Biomedical Signal Processing and Control, 51 (2019), pp. 162–170.

[34] L. Mainardi, M. Bertinelli, and R. Sassi, *Analysis of t-wave alternans using the ramanujan transform*, in 2008 Computers in Cardiology, IEEE, 2008, pp. 605–608.

[35] L. Mainardi, L. Pattini, and S. Cerutti, *Application of the ramanujan fourier transform for the analysis of secondary structure content in amino acid sequences*, Methods of information in medicine, 46 (2007), pp. 126–129.

[36] M. Malik, P. Färbom, V. Batchvarov, K. Hnatkova, and A. Camm, *Relation between qt and rr intervals is highly individual among healthy subjects: implications for heart rate correction of the qt interval*, Heart, 87 (2002), pp. 220–228.

[37] Z. Mouyan, C. Zhenming, and R. Unbehauen, *Separation of periodic signals by using an algebraic method*, in 1991., IEEE International Sympoisum on Circuits and Systems, IEEE, 1991, pp. 2427–2430.

[38] D. D. Muresan and T. W. Parks, *Orthogonal, exactly periodic subspace decomposition*, IEEE Transactions on Signal Processing, 51 (2003), pp. 2270–2279.

[39] M. Nakashizuka, *A sparse decomposition for periodic signal mixtures*, in 2007 15th International Conference on Digital Signal Processing, IEEE, 2007, pp. 627–630.

[40] A. V. Oppenheim and R. W. Schafer, *From frequency to quefrency: A history of the cepstrum*, IEEE signal processing Magazine, 21 (2004), pp. 95–106.

[41] M. Planat, *Ramanujan sums for signal processing of low frequency noise*, in IEEE International frequency control symposium and PDA exhibition, 2002, pp. 5–10.

[42] M. Planat, M. Minarovjech, and M. Saniga, *Ramanujan sums analysis of long-period sequences and 1/f noise*, Epl, 85 (2009).

[43] S. Ramanujan, *On certain trigonometrical sums and their applications in the theory of numbers*, Trans. Cambridge Philos. Soc, 22 (1918), pp. 259–276.

[44] N. Rea, G. Lacey, R. Dahyotit, and R. Dahyot, *Multimodal periodicity analysis for illicit content detection in videos*, in The 3rd European Conference on Visual Media Production (CVMP 2006)-Part of the 2nd Multimedia Conference 2006, IET, 2006, pp. 106–114.

[45] B. Santhanam and P. Maragos, *Demodulation of discrete multicomponent am-fm signals using periodic algebraic separation and energy demodulation*, in 1997 IEEE International Conference on Acoustics, Speech, and Signal Processing, vol. 3, IEEE, 1997, pp. 2409–2412.

[46] ——, *Harmonic analysis and restoration of separation methods for periodic signal mixtures: Algebraic separation versus comb filtering*, Signal Processing, 69 (1998), pp. 81–91.

[47] M. Schmidt, A. Schumann, J. Müller, K.-J. Bär, and G. Rose, *Ecg derived respiration: comparison of time-domain approaches and application to altered breathing patterns of patients with schizophrenia*, Physiological measurement, 38 (2017), p. 601.

[48] W. A. Sethares and T. W. Staley, *Periodicity Transforms*, IEEE Transactions on Signal Processing, 47 (1999), pp. 2953–2964.

[49] ——, *Meter and periodicity in musical performance*, Journal of New Music Research, 30 (2001), pp. 149–158.

[50] L. Su and H.-T. Wu, *Extract fetal ECG from single-lead abdominal ECG by de-shape short time Fourier transform and nonlocal median*, Frontiers in Applied Mathematics and Statistics, 3 (2017), p. 2.

[51] P.-C. Su, S. Miller, S. Idriss, P. Barker, and H.-T. Wu, *Recovery of the fetal electrocardiogram for morphological analysis from two trans-abdominal channels via optimal shrinkage*, Physiological measurement, 40 (2019), p. 115005.

[52] L. Sugavaneswaran, S. Xie, K. Umapathy, and S. Krishnan, *Time-frequency analysis via ramanujan sums*, IEEE Signal Processing Letters, 19 (2012), pp. 352–355.

[53] Task Force of the European Society of Cardiology and the North American Society of Pacing and Electrophysiology, *Heart rate variability: standards of measurement, physiological interpretation and clinical use. task force of the european society of cardiology and the north american society of pacing and electrophysiology*, Circulation, 93 (1996), pp. 1043–1065.

[54] T. Taxt, *Comparison of cepstrum-based methods for radial blind deconvolution of ultrasound images*, IEEE transactions on ultrasonics, ferroelectrics, and frequency control, 44 (1997), pp. 666–674.

[55] S. Tenneti and P. Vaidyanathan, *Dictionary approaches for identifying periodicities in data*, in 2014 48th Asilomar Conference on Signals, Systems and Computers, IEEE, 2014, pp. 1967–1971.

[56] S. V. Tenneti and P. Vaidyanathan, *Nested periodic matrices and dictionaries: New signal representations for period estimation*, IEEE Transactions on Signal Processing, 63 (2015), pp. 3736–3750.

[57] ——, *Ramanujan filter banks for estimation and tracking of periodicities*, in 2015 IEEE International Conference on Acoustics, Speech and Signal Processing (ICASSP), IEEE, 2015, pp. 3851–3855.

[58] ——, *Detecting tandem repeats in DNA using Ramanujan filter bank*, in 2016 IEEE International Symposium on Circuits and Systems (ISCAS), IEEE, 2016, pp. 21–24.

[59] ——, *A unified theory of union of subspaces representations for period estimation*, IEEE Transactions on Signal Processing, 64 (2016), pp. 5217–5231.

[60] ——, *MUSIC and Ramanujan: MUSIC-like algorithms for integer periods using nested-periodic-subspaces*, in 2017 51st Asilomar Conference on Signals, Systems, and Computers, IEEE, 2017, pp. 1997–2001.

[61] S. V. Tenneti and P. P. Vaidyanathan, *imusic: A family of music-like algorithms for integer period estimation*, IEEE Transactions on Signal Processing, 67 (2018), pp. 367–382.

[62] G. Thakur and H.-T. Wu, *Synchrosqueezing-based recovery of instantaneous frequency from nonuniform samples*, SIAM Journal on Mathematical Analysis, 43 (2011), pp. 2078–2095.

[63] R. Tibshirani, *Regression shrinkage and selection via the lasso*, Journal of the Royal Statistical Society: Series B (Methodological), 58 (1996), pp. 267–288.

[64] R. J. Tibshirani et al., *The lasso problem and uniqueness*, Electronic Journal of statistics, 7 (2013), pp. 1456–1490.

[65] K. Tokuda, T. Kobayashi, T. Masuko, and S. Imai, *Mel-generalized cepstral analysis-a unified approach to speech spectral estimation*, in Third International Conference on Spoken Language Processing, 1994.

[66] J. A. Tropp, *Just relax: Convex programming methods for identifying sparse signals in noise*, IEEE Transactions on Information Theory, 52 (2006), pp. 1030–1051.

[67] P. Vaidyanathan, *Ramanujan sums in the context of signal processing–Part I: Fundamentals*, IEEE Transactions on Signal Processing, 62 (2014), pp. 4145–4157.

[68] ——, *Ramanujan sums in the context of signal processing–Part II: FIR representations and applications*, IEEE Transactions on Signal Processing, 62 (2014), pp. 4158–4172.

[69] P. Vaidyanathan and P. Pal, *The Farey-dictionary for sparse representation of periodic signals*, in 2014 IEEE International Conference on Acoustics, Speech and Signal Processing (ICASSP), IEEE, 2014, pp. 360–364.

[70] M. J. Wainwright, *Sharp thresholds for High-Dimensional and noisy sparsity recovery using l_1-Constrained Quadratic Programming (Lasso)*, IEEE transactions on Information Theory, 55 (2009), pp. 2183–2202.

[71] P. Wang, J. Gao, and Z. Wang, *Time-frequency analysis of seismic data using synchrosqueezing transform*, IEEE Geoscience and Remote Sensing Letters, 11 (2014), pp. 2042–2044.

[72] S.-C. Wang, H.-T. Wu, P.-H. Huang, C.-H. Chang, C.-K. Ting, and Y.-T. Lin, *Novel imaging revealing inner dynamics for cardiovascular waveform analysis via unsupervised manifold learning*, Anesthesia & Analgesia (in press), (2020).

[73] H.-T. Wu, *Instantaneous frequency and wave shape functions (I)*, Applied and Computational Harmonic Analysis, 35 (2013), pp. 181–199.

[74] J. Xu, H. Yang, and I. Daubechies, *Recursive diffeomorphism-based regression for shape functions*, SIAM Journal on Mathematical Analysis, 50 (2018), pp. 5–32.

[75] H. Yang, *Synchrosqueezed wave packet transforms and diffeomorphism based spectral analysis for 1d general mode decompositions*, Applied and Computational Harmonic Analysis, 39 (2015), pp. 33–66.

[76] P. Zhao and B. Yu, *On model selection consistency of Lasso*, Journal of Machine Learning Research, 7 (2006), pp. 2541–2563.

[77] Z. Zhou, *Heteroscedasticity and autocorrelation robust structural change detection*, J AM STAT ASSOC, 108 (2013), pp. 726–740.

[78] M.-y. Zou and R. UNBERHAUEN, *An algebraic theory for separation of periodic signals*, AEU. Archiv für Elektronik und Übertragungstechnik, 45 (1991), pp. 351–358.

Biography

Ziyu Chen received a B.S. in mathematics from Zhejiang University in 2016. In 2016, he arrived at Duke University and became a graduate student in the Department of Mathematics working in the direction of adaptive time-frequency analysis, under the supervision of Professor Ingrid Daubechies and Professor Hau-Tieng Wu. He will become a Visiting Assistant Professor at Duke University for the Academic Year 2021-2022.